UNIVERSITÀ
DEGLI STUDI
DI PADOVA

Sede Amministrativa: Università degli Studi di Padova

Dipartimento di Salute della Donna e del Bambino

Corso di Dottorato di Ricerca in medicina dello sviluppo e scienze della programmazione sanitaria

Curriculum: Emato-oncologia, genetica, malattie rare e medicina predittiva

32° Ciclo

“Alveolar Rhabdomyosarcoma 3D model development to mimic physiological cell-ECM interactions with focus on integrins.”

Tesi redatta con il contributo finanziario della
Fondazione Istituto di Ricerca Pediatrica Città della Speranza

Coordinatore: Prof. Carlo Giaquinto

Supervisore: Prof. Maurizio Muraca

Co-Supervisore: Dott.ssa Michela Pozzobon

Dottorando: Mattia Saggioro

…“*It seems to me that the observations associated with black body radiation, fluorescence, the production of cathode rays by ultraviolet light, and other related phenomena connected with the emission or transformation of light are more readily understood if one assumes that the energy of light is discontinuously distributed in space*.”

These simple and clear lines are the real birth certificate of quantum theory.

Note the wonderful initial “It seems to me…”, which recalls the “I think…” with which Darwin introduces in his notebooks the great idea of that species evolve, or the “hesitation” spoken of by Faraday when introducing to the first time the revolutionary idea of magnetic fields.

Genius hesitates.

- Seven brief histories of physics -

Prof. Carlo Rovelli

Summary

Riassunto

Introduzione:

Rabdomiosarcoma (RMS) è il sarcoma dei tessuti molli più frequente in età pediatrica, le due sottoclassi principali sono quella embrionale (ERMS), associata ad una prognosi favorevole, e quella alveolare (ARMS) altamente metastatica e con prognosi sfavorevole. Se da un lato la conoscenza del profilo genetico di RMS è ben approfondita, l'aspetto della caratterizzazione del suo microambiente è ancor'oggi poco definita. Finora, le interazioni tra cellule tumorali e stromali sono state indagate con modelli *in vitro* 2D. Tuttavia, questi modelli non sono rappresentativi dei complessi processi biologici che avvengono *in vivo*, tra i quali la migrazione cellulare. Questa dipende dalle interazioni 3D tra cellule e la matrice extracellulare (ECM) attraverso molecole di adesione come le integrine. Difatti, le interazioni cellula-cellula e cellula-ECM sono ben rappresentate in modelli 3D, che mimano meglio la condizione fisiologica.

Scopo:

Lo scopo di questo lavoro è lo sviluppo di un modello 3D di RMS, in grado di ricreare le interazioni cellula-matrice, con particolare attenzione sulle integrine, e di rappresentare i processi di migrazione cellulare che avvengono in condizioni fisiologiche.

Materiali e Metodi:

Sono state eseguite analisi bioinformatiche sull'espressione di geni della ECM di pazienti affetti da ARMS e da ERMS. Per il primo modello 3D, le masse di ARMS sono state decellularizzate mediante trattamento detergente-enzimatico. Tre differenti strategie di ricellularizzazione sono state testate: semina superficiale, microiniezione e bioreattore a perfusione. L'analisi proteomica del tessuto di ARMS è stata eseguita per determinare la composizione proteica della ECM. Sono stati sviluppati due ulteriori modelli 3D basati su: Ultrafoam e hydrogels di acido ialuronico/PEG (HA/PEG). Il ruolo di ITGA5 nella motilità cellulare è stato investigato *in vitro* a seguito di trasfezione con siRNA. La crescita tumorale e la migrazione metastatica sono stati testati *in vivo*.

Risultati:

15 geni correlati alla ECM risultano differenzialmente espressi tra pazienti affetti di ARMS ed ERMS. Per il primo modello 3D, le masse di ARMS sono state decellularizzate ma le tecniche di ricellularizzazione non hanno garantito un buon risultato in termini di distribuzione e vitalità cellulare. La composizione della matrice riporta collageni (tipo I e III), fibrillina, fibronectina e periostina. Tra i due ulteriori modelli 3D, Ultrafoam fornisce una struttura simile al tessuto con: superiore proliferazione (41% contro 24%), secrezione di MMP-2 e sovra espressione dei geni ITGA5 e CXCR4 rispetto ai controlli 2D. Gli hydrogels di HA/PEG formano un supporto 3D dove gli sferoidi non dimostrano invasività. L'inibizione *in vitro* di ITGA5 risulta in una ridotta abilità migratoria (24.3% contro 43.9% nel controllo). Nel test di invasività entrambe le cellule risultano incapaci di invadere il Matrigel, tuttavia è stata osservata una differente organizzazione cellulare tra cellule di controllo e

silenziare. La crescita tumorale in vivo non mostra associazione con la presenza di ITGA5; tuttavia, la frequenza di extravasazione risulta maggiore in presenza di ITGA5 (30.6% contro 8.5%).

Discussione:

Tra i modelli 3D testati, l'utilizzo diretto della matrice decellularizzata ha evidenziato una ridotta porosità del supporto, risultando in una distribuzione di cellule superficiale e la prevalenza di interazioni cellula-cellula piuttosto che cellula-ECM. Il supporto di Ultrafoam ha prodotto i migliori risultati in termini di interazioni cellula-microambiente; tuttavia, il bioreattore è inaccessibile per la visualizzazione al microscopio. D'altra parte, l'hydrogel è otticamente trasparente e più direttamente funzionalizzabile con altre proteine di matrice specifiche di ARMS. Negli hydrogels di HA/PEG, la concentrazione di fibronectina verrà ottimizzata assieme all'aggiunta di altre proteine di matrice. I risultati *in vitro* evidenziano che altre proteine cooperano nella migrazione cellulare nelle cellule di ARMS. La differente organizzazione in Matrigel suggerisce un cross-talk tra ITGA5 e proteine di adesione cellula-cellula. I risultati *in vivo* indicano che ITGA5 non è necessaria per la crescita tumorale, tuttavia sembra avere un ruolo funzionale nel processo di extravasazione.

Conclusioni:

Questo lavoro ha sviluppato tre differenti modelli 3D per lo studio di ARMS, ciascuno con vantaggi e svantaggi che devono essere considerati a seconda del processo biologico da investigare. In futuro prevediamo che un'analisi più dettagliata del microambiente di ARMS potrà portare alla luce di nuovi marcatori prognostici e terapeutici per migliorare la sopravvivenza dei giovani pazienti.

Abstract

Introduction:

Rhabdomyosarcoma (RMS) is the most common Soft Tissue Sarcoma in childhood, the two main subtypes are embryonal RMS (ERMS), associated with a better prognosis, and alveolar RMS (ARMS), more aggressive and highly metastatic. If the knowledge of RMS genomic alterations is well established, its microenvironmental characterization is still poorly defined. So far, *in vitro* 2D models are used to recapitulate the interactions between cancer cells and stromal cells. However, these models are not representative of the complex biological processes that happen *in vivo*, such as cell migration. This, in particular, depends on 3D interactions between cells and ECM via adhesion molecules, i.e. integrins. In this context, the cell-ECM and cell-cell interactions are better studied with 3D models that offer a platform where culture conditions approximate better the physiological conditions.

Aim:

This work aims at the development of a 3D model able to recreate the 3D complex cells-ECM interactions, with particular attention on integrins, and to represent the cell migration process taking place in physiological conditions.

Material and Methods:

Bioinformatic analysis was used to determine differential expression of ECM genes in ARMS end ERMS patients. Decellularization of ARMS xenogenic tumor masses employed cycles of detergents and enzymatic treatments (DET). Three different recellularization strategies were adopted: superficial seeding, microinjection and a perfusion bioreactor. Mass spectrometry (MS) analysis of ARMS tissue was performed to determine ECM protein composition. Two 3D models: 1- Ultrafoam collagen I sponge, 2- hyaluronic acid/PEG hydrogel (HA/PEG) were developed. ITGA5 role in cell motility was investigated *in vitro* upon siRNA transfection evaluating. Tumor growth and metastatic migration was tested *in vivo*.

Results:

15 ECM genes were shown to be differentially expressed between ARMS from ERMS patients. Xenogenic ARMS were successfully decellularized but the three recellularization techniques tested were not optimal in terms of viability and cell distribution. MS revealed major presence of collagens (type I and type III), fibrillin, fibronectin and periostin in ARMS ECM building. With Ultrafoam collagen I sponge we obtained a tissue-like structure in 7 days of culture, higher proliferation rates (41% vs 24%), enhanced secretion of MMP-2 and overexpression of ITGA5 and CXCR4 mRNAs compared to 2D controls. HA/PEG hydrogel formed a 3D support where cultured spheroids showed no invasion. *In vitro* migration assay showed reduction of migrating cells upon ITGA5 siRNA silencing (24.3% vs 43.9% in the control). In the invasion assay, cells were unable to invade the Matrigel, however we reported differential cell clustering with larger multicellular strands in control cells and smaller spherical

aggregates in ITGA5 silenced cells. *In vivo* tumor growth showed no dependence on ITGA5; conversely, extravasation rate was higher in presence of ITGA5 (30.6% vs 8.5%) in the zebrafish model.

Discussion:

This study highlighted the first preliminary results on ARMS cell-ECM interaction. Among the tested 3Dmodels, the direct use of the ARMS ECM evidenced reduced porosity, impacting on superficial cell seeding and prevalence of cell-cell interactions rather than cell-ECM adhesions. The use of commercially available scaffold composed of Collagen I (Ultrafoam) gave the best results in terms of interaction with the microenvironment; however, the bioreactor is inaccessible for fluorescence live imaging. In contrast, hydrogels are optically transparent and easier to enrich with other ARMS ECM specific proteins. In HA/PEG hydrogel, concentration of fibronectin has to be optimized together with the addition of other ECM proteins. *In vitro* results on ITGA5 expression by RH30 cells suggest that other fibronectin-binding integrins can cooperate for cell migration. Differences in cell clustering suggested an interplay between ITGA5 and cell-cell adhesion proteins. *In vivo* experiments imply that ITGA5 is not required for tumor growth and appeared to be functionally relevant for the extravasation process.

Conclusions:

This work developed three different 3D models of ARMS, each one with specific advantages and disadvantages that have to be considered depending on the investigated biological process. In the future, we foresee that deeper investigation on ARMS microenvironment could develop new prognostic or therapeutic markers to ameliorate the overall survival of the young patients.

Introduction

Sarcomas are a large and heterogeneous group of malignancies arising from mesenchymal tissues as bone, cartilage, muscle, fat and peripheral nerves (Figure 1.1). In general, sarcomas are reported as rare tumors, representing less than 10% of all cancer affecting around 200.000 patients each year, with a higher morbidity and mortality in children and young adults[1]. From a genetic point of view, sarcomas can be divided in two main categories: the “near-diploid karyotypes”, with simple genetic alterations or chromosomic translocations; and “complex karyotypes”, with chromosome instability, multiple genomic alterations and unbalanced karyotypes. The genomic profile characterization of sarcomas subtypes is shading light on the molecular mechanisms involved in the pathology, identification of fusion oncogenes, their transcriptional targets and pathways deregulation. This will possibly help to stratify patients into more accurate classes of risk and provide subtype-specific targets for molecular therapy improving outcome of patients [1,2]. The current classification of “Tumors of Soft Tissue and Bone”, published by the World Health Organization (WHO) in 2013, divides soft tissue and bone sarcomas in 12 groups: 1) adipocytic tumors; 2) fibroblastic/myofibroblastic tumors; 3) fibrohistocytic tumors; 4) smooth muscle tumors; 5) pericytic tumors; 6) skeletal muscle tumors; 7) vascular tumors; 8) gastrointestinal stromal tumors; 9) nerve sheath tumors; 10) chondroosseous tumors; 11) tumors of uncertain differentiation and 12) undifferentiated and unclassified sarcomas. This new classification replaces the 2002 edition and includes new genetic and molecular characterization of soft tissue an bone sarcomas [3].

***Figure 1.1**: Classification of sarcomas subtypes based on 2002 WHO classification updated with genetic information (N.B. it is not the official 2013 classification). Length of the branches is representative of differences in prognosis, driver alterations and additional parameters [4].*

Among this large group of malignancies, this work will focus on a specific subtype of sarcoma: rhabdomyosarcoma (RMS) and in particular on the alveolar variant (ARMS). The following chapters will introduce rhabdomyosarcoma from a clinical and molecular perspective together with the description of some RMS models used to study the genetic background. Some of the most recent techniques for 3D *in vitro* culture will be presented and discussed introducing basic principles, advantages, limitations and few examples, considering RMS or sarcomas when possible. We will extend the description of ARMS from a wider prospective that considers the tumor microenvironment (TME) in its stromal cell population and extracellular matrix (ECM). Finally, we will examine the process of metastatic migration at tissue and cell level, the different strategies of cell motility and the role of cell-cell and cell-ECM adhesions in this biological process.

Rhabdomyosarcoma

Rhabdomyosarcoma (RMS) is the most common Soft Tissue Sarcoma (STS) in childhood with an incidence of 4.5 cases among 1’000’000 new-borns, accounting for about 40% of the total soft tissue sarcomas and 7% of all malignancies. Rhabdomyosarcoma typically arises in adolescence, with 50% of the cases reported in the first decade of life [5]. RMS is uncommon in adults, representing less than 1% of total malignancies and about 3% of all STS, but the overall outcome is significantly worst since, more often, adult patients presents at the diagnosis with poor prognosis factors (e.g. pleomorphic histology and unfavourable sites of onset) [6,7].

The World Health Organization classified 4 main RMS subtypes: alveolar RMS (ARMS); embryonal RMS (ERMS); pleomorphic RMS (PRMS) and spindle cell/sclerosing RMS (SRMS) [3].

The two main paediatric subtypes are the ERMS and ARMS, accounting for the 57% and the 23% of all diagnosed RMS respectively. ERMS has a higher incidence: 2,6 cases per million people per year, and an earlier age of onset, with a peak in the first 5 years of life. The primary sites are more frequently: genitourinary tract, parameningeal and orbits (78% of the cases). ERMS is typically associated with a better prognosis with higher relative 5-years survival rates (73,4%). ARMS has no preferential age of onset, the incidence is 1 case per million people per year and the most frequent primary sites are extremities, parameningeal and the head and neck area (67% of the cases). It is associated with poorer outcome and a lower 5-years survival rate (47,8%) due to the high aggressiveness and tendency to metastasize [5].

Histologically ERMS cells appears small, round to elongated shape with uniform chromatin and heterogeneous grade of differentiation; ARMS cells are small round cells, with hyperchromatic nuclei, growing in clusters dispersed in fibrosus septa composed mainly by collagen, resembling lung alveoli [8].

The genetic characterisation of ARMS highlights the chromosomic translocations t(2:13) and less frequently t(1:13) resulting in the expression of chimeric fusion proteins PAX3-FOXO1 and PAX7-FOXO1 respectively. These two fusion oncoproteins have important prognostic value and are specific of ARMS subtype [9]. From the molecular point of view these two fusion proteins contains the N-terminal region of PAX3 or PAX7, with conserved DNA-binding activity, and the potent transcription activating domain of FOXO1 at the C-terminal of the protein. The result is a functional oncogenic transcription factor that acts down-regulating genes involved in “muscle development” and “muscle contraction” – as ACTC, MYL1, MYOG, SNAI2, and TNNC2 – and up-regulating genes involved in “programmed cell death”, “apoptosis” and “cell proliferation” [10,11].

ERMS is characterized by multiple numerical chromosome alterations: more frequently gains of chromosomes 2, 7, 8, 12 and 13 and loss of chromosomes 9 and 10; loss of heterozygosis and loss of imprinting on chromosome 11. Genomic amplification is more frequent in ARMS than in ERMS and occurs in the chromosomal regions: 1p36, 2p24, 12q13-q14, 13q14, and 13q31. Mutations found in ERMS are more frequently in RAS family, FGFR4, PI3CA, CTNNB1, BRAF and PTPN11 genes [8,12,13]. A comprehensive genomic analysis of 147 RMS tumor samples revealed that FGFR4, RAS, NF1, PIK3CA genes, included in receptor tyrosine kinase/RAS/PIK3CA pathway, were the most frequently altered in fusion negative RMS (at least 45% of the cases). The receptor tyrosine kinase/RAS/PIK3CA axis is altered in both fusion-positive and fusion-negative RMS but with two different mechanisms: the first via deregulation of the genes (MYOD1, MET, CNR1, FGFR4, FGFR4, CCND2, and IGF2) downstream the transcription of the fusion oncoprotein and the second via accumulation of mutations in those genes [14].

The origin of ARMS cells is still debated; the potential candidates that have been proposed are dedifferentiating myoblast and uncommitted mesenchymal cells [15]. Keller and Capecchi developed conditional knock-in mice expressing Pax3:Foxo1 at different developmental stages and reported that, only in neonatal stage, expression of the fusion protein resulted in alveolar rhabdomyosarcoma onset. Pax3:Foxo1 induction in satellite cells did not result in tumor initiation, implying that ARMS cell of origin is more likely a differentiating mature cell rather than a myogenic precursor. Moreover, they demonstrate how expression of the fusion oncoprotein was necessary but not sufficient to induce ARMS formation at high frequency and only with additional knock-out of *Trp53* and *CDKN2A*, reported to be altered in ARMS human cases, they were able to induce ARMS tumors at high frequency [16].

On the other hand, inducing the expression of PAX3-FOXO1 and PAX7-FOXO1 in bone marrow derived mice mesenchymal stem cells (mMSC), Yue-Xin Ren and co-workers obtained cells expressing MyoD and myogenin, increased growth rate and reduced contact inhibition. However, they were not able to form tumors in mice, confirming what previously demonstrated by Keller, that the fusion oncoprotein was necessary but not sufficient to induce ARMS. Disruption of RB, p53 and Ras pathways led to significantly higher tumor formation, demonstrating that progenitor or ARMS can also be a mesenchymal stem cell [17].

Cre-Lox mouse models of ERMS were used by Rubin and colleagues to study the effect of Ptch1 heterozygous deletion and lineage specific p53 homozygous deletion in different stage of myogenesis. Myf6Cre-p53$^{-/-}$, representative of prenatal and postnatal maturing myoblasts, gave rise to eRMS in 100% of the cases and less frequently ERMS histology in MCre-p53$^{-/-}$ (31%), MCre-p53$^{-/-}$Ptch1$^{+/-}$ (42%), Pax7CreER-Ptch1$^{+/-}$p53$^{-/-}$ (13%) suggesting that ERMS can arise from cells in many stages of myogenic differentiation, but the degree of differentiation depends on the cell of origin. Gene expression profiles of 111 primary human fusion-negative RMS confirmed that the predominant mutation was p53 loss (in 59% of the cases). These results demonstrate that p53 mutation can give rise to ERMS if cell of origin is a Myf5-maturing myoblast, Ptch1 is considered as a modifier of ARMS that contribute to tumor initiation [18].

Several models have been used to exploit the genetic background of RMS (Figure 2.1). Besides mouse models, used for reverse genetics studies and tumor onset, *Drosophila* and *Zebrafish* models are getting attention thanks to their potential applications in forward genetics approaches, *in vivo* imaging and low demands in terms of cost and time. *Zebrafish* model, used for ERMS disease modelling, offers a system where myoblast fusion pathways are conserved with mammals [19]. Up to date no *Zebrafish* models of ARMS have been reported, but thanks to the advantages offered by this model and the similarity with mammals, a *Zebrafish* model of ARMS is highly desirable. On the other hand, *Drosophila* is used to study ARMS genetics thanks to the homology of human PAX3 and PAX7 with orthologues Gooseberry and Goosebery-neuro respectively. However, tumor formation is not achieved *in vivo* and PAX7-FOXO1 transformed cells could only be followed infiltrating adjacent tissues at single cells level [20].

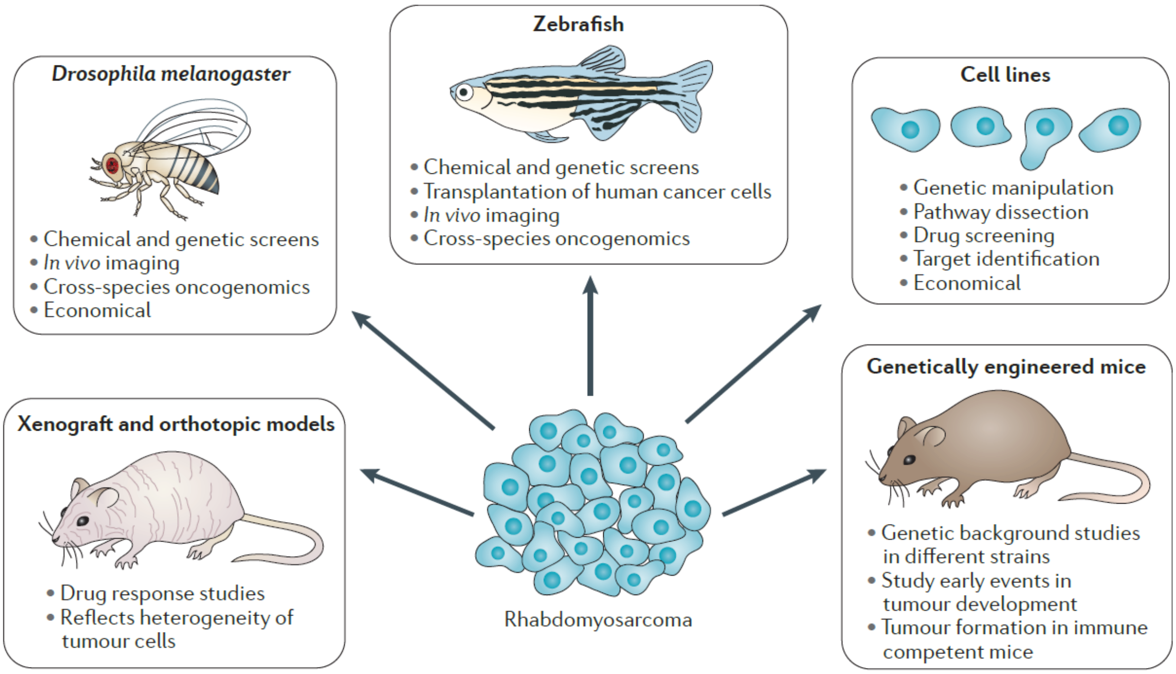

Figure 2.1: *Different model organisms used to study rhabdomyosarcoma with list of advantages offered by each model* [20].

If genetic modelling of RMS is well established and can be exploited in different model organisms, a model of the disease progression is still lacking. Most of the studies presented above are focused on the genetic background that lead to RMS onset, defining the involved genes and dysregulated pathways. In this view the different stages of the disease and microenvironmental are only partially considered. *In vitro* and *ex vivo* models can be employed to investigate, in a more controlled onset, given the higher intrinsic variability of *in vivo* models, the interactions between cancer cells and their microenvironment.

A good example that employs an extracellular matrix-based support for *ex vivo* 3D cell culture is given by Chen and colleagues. Briefly, healthy colon was decellularized to obtain an acellular scaffold for cell co-culture of myofibroblasts, endothelial cells and genetically modified epithelial cells, disrupting APC and overexpressing KRAS, to induce malignant phenotype. The three cell populations were seeded on the decellularized extracellular matrix (dECM) in a multistep process. The model recapitulates over-time the hallmarks of disease progression: distorted crypts, multicellular layers, increased proliferation and, upon TGF-β stimulation, large adenoma formation and submucosa invasion. This contrasted clearly the morphology obtained by recellularization of the same dECM with hTERT transformed healthy epithelial cells (representing the healthy colon epithelium) that showed single cell layer crypts, tightly attached to basal membrane and stromal ECM. This model identified 38 new genes that drive malignant submucosal invasion [21].

In vitro 3D culture

3D models are getting more and more attention from the scientific community since, with constant development of more advanced layouts, they promise to bridge the gap between *in vitro* classical models and *in vivo* systems. Classical *in vitro* systems are often oversimplified compared to the *in vivo* conditions in which cells are included. If for some cell type and some biological processes this simplification can be accepted – for example in the case of epithelial cells that possess an intrinsic apical-basal polarity – for other cell types like mesenchymal cells, that are embedded in 3D tissue, the 2D culture represent an unnatural condition that profoundly impacts on biological responses. The main differences between 2D surfaces and 3D systems affects especially cell adhesion, mechanotransduction and the emerging of gradients (Figure 3.1); these, in turn, have an impact on cell morphology, organization and migration but also differentiation and drug resistance [22].

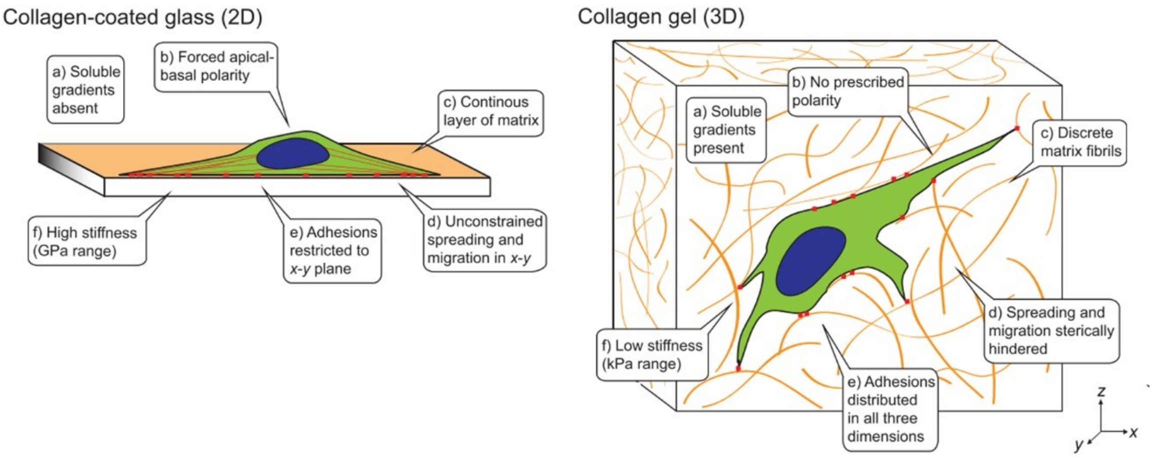

Figure 3.1: *Cues sensed by cells in 2D vs 3D in vitro culture conditions: gradients, polarity, continuity of matrix and adhesion substrates, stiffness* [22].

There are several systems to culture cells in 3D settings:

1. **Spheroids & organoids**: these models are maybe the simplest and the most widespread. They rely mainly on the self-assembly of cells when cultured in absence of adhesive substrates.
   Spheroids are commonly obtained from cell lines or homogeneous tumor tissues, whereas organoids refer usually to multicellular structures with heterogeneous cell populations and peculiar structure resembling the tissue of origin (e.g. intestinal organoids forms crypts with stem cells on the bottom). Thanks to gradients of nutrients and oxygen along the radius, aggregates larger than 500 μm display heterogeneous population with a necrotic core and high proliferating and invasive cell layer on the surface. Spheroids and organoids can be cultured with different techniques: hanging drop, liquid overlay, spinner or rotating flask, magnetic levitation and others [23]. In the case of sarcomas, tumor spheroids and patient derived tumor organoids are of particular interest since they could partially overcome the limitation of the restricted variety of cell lines available (especially for some of the sarcomas subtypes) and the paucity of patient-derived biological samples. The potential applications of these 3D models span from more reliable drug testing platforms for personalized medicine to study of vascularization or drug resistance on a model that mimics multicellular micro-metastases [24]. The effect of MEK/ERK pathway inhibition was studied on cancer stem cell population of ERMS

spheroids, displaying downregulation of stemness markers (CD133, CXCR4 and Nanog) together with delayed tumor development and reduced tumor growth *in vivo* [25]. In another study, ERMS cell line overexpressing Cav1 exhibits enhanced formation of lung metastases upon tail vein injection in immunodeficient mice. Cells isolated from metastases and grown as spheroids showed higher metastatic capability in migration assays and secretion of angiogenic factors [26]. Finally, Thuault and colleagues analysed the migration potential of ARMS and ERMS derived spheroids. Their results highlighted how the increased invasive potential of ARMS cells is regulated through downregulation of the Rho GTPase RhoE, a ROCK inhibitor, and upregulation of the GTPase activating protein (GAP) ARHGAP25that controls Rac activity downstream ROCK activation [27].

2. **Microfluidic devices:** microfluidic platforms integrate micro-engineered structures as channels, valves, pillars and pumps in micropatterned integrated devices (Figure 4.1). The most common material used for this applications is poly-dimetylsiloxane (PDMS) due to its optical transparency, that allows high quality and long-term imaging, and gas permeability to facilitate gas exchange between cells and the environment. In the microfluidic scale, fluids display laminar flow characteristic; this enable the generation of gradients of soluble factors and a precise spatial and temporal control of the stimulations. Scaling down the volumes of the cultures leads to reduction of costs, but also increases the concentration of paracrine factors secreted by cells. Reduction of both costs and size facilitates parallelization of the experiments in high-throughput platforms capable to reach statistical significance analysing single cell events. Given these great potentials, it’s not surprising that a variety of microfluidic devices have been developed for many applications: from cell adhesion and motility upon gradients stimulation to modelling of complex organ physiology implementing also mechanical stimulation [28–30].
3.

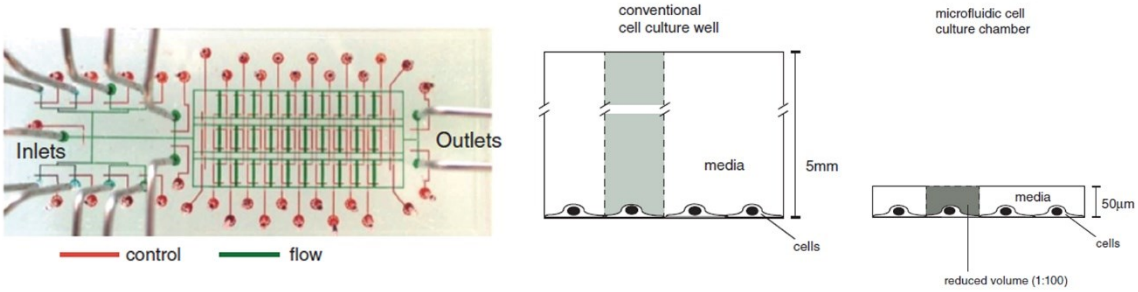

Figure 4.1: *An example of microfluidic chip; multiple culture chambers are controlled by complex layer of valves. Effects of the downscaling to microfluidic scale on culture volumes (adapted from [28]).*

Unfortunally, to our knowledge, no microfluidic devices have been developed for the study of RMS. An example of how this technology can model complex, multicellular environment and systemic biological effect is given by Bersini and colleagues. Briefly a tri-culture of osteo-differentiated bone marrow derived mesenchymal stem cell (hBM-MSC), endothelial cells and highly metastatic breast cancer cells is integrated into a microfluidic chip to recreate the bone marrow metastatic niche. Breast cancer cells, circulating in the microfluidic channel covered by a lined layer of endothelial cells, were shown to extravasate in response to CXCL5 (produced by hBM-MSC) recognition by the CXCR2 receptor (present on cancer cell surface), invade the collagen 1 hydrogel, containing the osteo-differentiated hBM-MSC, and form micrometastases [31].

4. **3D bio-printing:** it is important to distinguish between 3D printing and 3D bio-printing: the former refers to an additive manufactory process that can use materials as metals, ceramics and plastics, where the conditions for printing are too harsh for biological systems. These has to be included in the printed model later, in a two-step process. One application of 3D printing is the development, from CT scans images, of patient specific surgical guides or models of the surgical area to aid surgeons before or during the operation.
   On the other side 3D bio-printing combines biologically compatible polymers (natural as alginate, gelatine, collagen, hyaluronic acid or synthetic as polyethylene glycol or polycaprolactone) and bio-compatible printing condition that allow the inclusion of cells suspended in the bio-ink directly during printing. The most common techniques for bioprinting are: inkjet based, extrusion, laser-induced and laser-assisted. Briefly, inkjet based 3d printing requires a heater or piezoelectric device to generate droplets of the bio-ink, these is deposited on the substrate (Figure 5.1A); extrusion bioprinting uses pneumatic or mechanic actuators to push the bio-ink through a nozzle resulting in continuous deposition of the bio-ink (Figure 5.1B); in laser-assisted bioprinting a laser beam is directed to a photo-crosslinkable polymer, containing the cell suspension, curing the designed pattern directly in the solution (Figure 5.1C); finally, in laser-induced bioprinting, cells are included in a laser adsorbing hydrogel, a laser beam controlled by micro-mirrors induces a vapour bubble and transfers cells encapsulated in the hydrogel on the receiving substrate, similarly to the inkjet technique (Figure 5.1D).

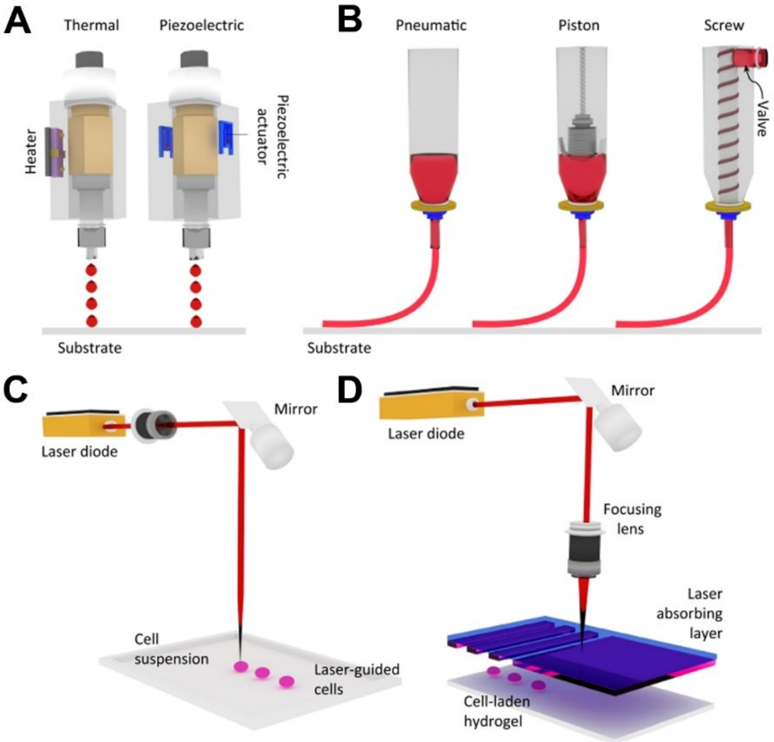

Figure 5.1: *3D bioprinting techniques: (A)Inkjet; (B) Extrusion; (C) Laser-assisted; (D) Laser-induced* [32].

Along the evolution of printing techniques, new bio-inks are being developed. Engineering, biomaterial science and biology work together to obtain new bio-inks. The main properties that a bio-ink has to have are: printability, biocompatibility, it has to be biodegradable with an appropriate kinetic and not generate toxic products, it has to provide mechanical and mechanical support to cells and finally it has to mimic the molecular properties of the *in vivo* tissues [32,33]. To our knowledge there are no example of 3D bio-printed models of RMS, however Fong and colleagues developed 3D printed model of Ewing sarcoma using polycaprolactone scaffold produced with electrospinning technique. Briefly, electrospinning technique is similar to extrusion 3D printing, where a high difference of electric potential is applied between the substrate and the nozzle. Ewing sarcoma cells cultured on this 3D printed support display grow kinetic and morphology similar to the human tumor and higher resistance to cytotoxic drugs. Authors identified enhanced and constitutive activation of IGF-1R compared to 2D cultures similarly to what reported in xenografts [34].

The potentials of 3D model for sarcoma research is still largely unexploited. However, 3D cultures seem to be a promising tool to overcome long-standing issues of sarcoma research as the paucity of available cell lines for most rare subtypes of sarcomas and the general low efficiency in obtaining primary cultures from patients in 2D systems. Patient derived 3D models would offer preclinical model with superior predictive value and a platform for a more reliable study of molecular pathway, tumor progression and drug screening, paving the way for approaches of personalized medicine [35].

Looking at the previous 3D culture models, a common aspect emerges: the importance to recreate a physiological environment that closely mimics the original tissue. Spheroids use the intrinsic ability of cells to self-aggregate and produce their own ECM; microfluidic uses complex geometries to recreate tissue micro-structures and implementing hydrogels or ECM-derived proteins (as collagen, laminin or fibronectin); 3D bioprinting employs natural polymers, synthetic polymers or ECM derived bio-inks printed to resemble tissue structure.

5. **Decellularization:** To retain the both protein composition and structural architecture of the ECM of a tissue, decellularization has been developed. In principle, during this process, cellular component within the tissue is depleted conserving the ECM proteins in their original spatial organization. Many protocols have been optimized for decellularization of specific tissues or whole organs, these protocols are often combinations of 3 general decellularization methods: physical, chemical and enzymatic (Figure 6.1). Briefly, physical methods involve freeze and thaw cycles, agitation or sonication; chemical methods include: alkaline and acidic solutions (that catalyse hydrolytic degradation of proteins), hypotonic and hypertonic solution (causing cell and organelles lysis by osmotic effect) and ionic or non-ionic detergents (that dissociate DNA from proteins, solubilize proteins and cell membranes); and finally enzymatic methods rely on proteolytic degradation of cell-ECM anchoring proteins, mild degradation of the ECM (e.g. treatment with collagenase) and degradation of nucleic acids with DNases and/or RNases. All these methods have their drawbacks, as an example: proteolytic treatment can degrade ECM proteins along with cell adhesion molecules, or alkaline and acidic solution can induce hydrolytic degradation of collagens together with cytosolic proteins.

   It is important to acknowledge that decellularization procedure has to balance between depletion of the cellular fraction and the maintenance of tissue composition, architecture and mechanical properties. Evaluation of decellularization efficiency mainly considers the following parameters: total DNA content of the dECM lower than 50 ng per mg of ECM dry weight, DNA fragment length lower than 200 pb and lack of DAPI in fluorescence or haematoxylin in H&E staining respectively [36–38].

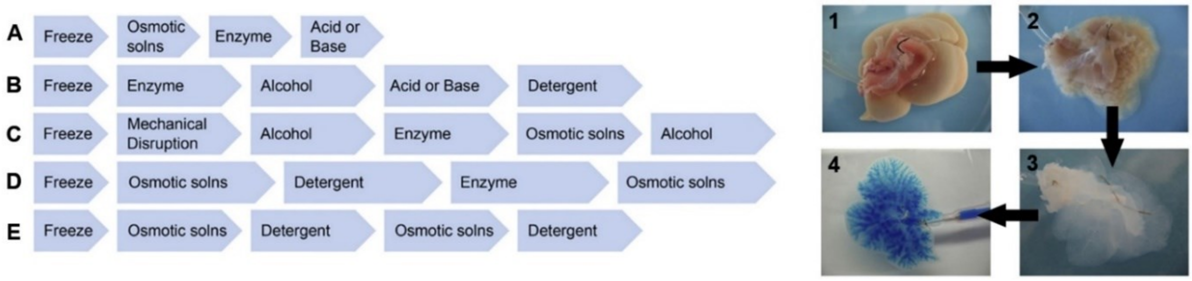

Figure 6.1: *on the left (A, B C, D, E) examples of decellularization protocols involving multistep decellularization methods; on the right: example of whole liver decellularization: (1) fresh tissue is perfused portal vein, (2) appearance of the tissue during decellularization and (3) at the end of the decellularization protocol; (4) blue dye shows the preservation of the vasculature after the process (adapted from [36]).*

Decellularized ECM are drawing attention especially for clinical application in regenerative medicine. Various dECM derived from porcine heart valves, porcine small intestinal submucosa and porcine bladder have been already approved by FDA for medical use [39]. They also represent the gold standard in terms of complexity and architecture of the scaffold. Together with decellularization of healthy tissues, decellularization of tumor tissues offers a platform more representative of the pathological microenvironment, enabling the study of cancer and stromal cells behaviour in a more physiological setting. In this view, tumor cells seeded on tumoral dECM would be suitable for modelling the tumor microenvironment of the disease [40]. The applications of decellularized matrix as scaffold for disease modelling has been anticipated in the previous paragraph with the discovery of new cancer-driving genes in colorectal cancer [21], however no attempt in the use of dECM as platform for 3D disease modelling in RMS has been made yet.

Our lab has good experience in decellularization techniques and in particular in decellularization of muscle tissues [41]. Decellularized ECM from mouse diaphragm was orthotopically transplanted in a mouse model of surgical diaphragmatic hernia, showing superior performance, compared to the standard of care Gore-Tex patch, in terms of regenerative potential, vascularization, re-innervation and functional recovery [42–44]. This experience was fundamental to develop part of this work, in particular addressing the issue of ARMS decellularization [45].

Interesting, future developments are emerging from the combination of 3D bioprinting and dECM derived hydrogels. As a matter of fact, natural and synthetic bioinks fail to represent the biological complexity of the *in vivo* tissue, since they often include only few structural proteins. On the other hand, dECM has proven to retain important cues for cells: enhancing homing, proliferation, differentiation and viability. The opportunity to 3D print in a desired size and shape tissues with the molecular complexity of the original tissue is intriguing both for applications in regenerative medicine and tissue engineering. An outstanding work from Pati and colleagues shows the development of 3 different bio-inks derived from adipose tissue, heart tissue and cartilage dECMs. The supports displayed increased differentiation and maturation of the respective stem cell populations [46].

3D bioprinting of dECM has still some issues to overcome: since dECM is from biological origin batch to batch variability could affect the quality of the final product; removal of DNA and decellularization residues has to be optimal not to induce cytotoxicity or immunogenic reaction and finally, by digestion of the dECM, spatial organization of the ECM proteins is lost, improvements in resolution of 3D printers may compensate this complication.

Tumor microenvironment

The tumor microenvironment (TME) emerges from the prospective that considers tumors not only as isolated, proliferating tumor cells but as complex and dynamic tissues, where several cell types and an unbalanced ECM contribute to tumor development, growth, immunological escape and metastatic migration (Figure 7.1). As a broad classification, TME can be divided in 2 main building blocks: the cellular and the acellular fraction. The former encompasses, besides tumor cells, a heterogeneous population of endothelial cells, immune cells, fibroblasts and other cells as myeloid derived suppressor cells (MDSCs) and adipocytes [47]. The latter can be further divided in "Core ECM proteins" and "ECM-associated proteins". "Core ECM proteins" are all the proteins, secreted in the extracellular space by cells, that assembles the scaffold that gives mechanical support and spatial organization to the surrounding cells; the 3 main classes of Core ECM proteins are: collagens, glycoproteins and proteoglycans. "ECM-associated proteins" are all the secreted proteins that interact with the ECM, but do not provide structural support, such as ECM-remodelling enzymes, growth factors and cytokines. [48,49].

In the next paragraphs we will discuss in detail the most relevant cellular and acellular components of the microenvironment. Unfortunally, specific data regarding RMS stromal cells or ECM are scarce or outdated. Hopefully, in the near future, the aforementioned advances in 3D tissue culture and disease modelling will open the way for new and powerful tools for the investigation of sarcomas TME.

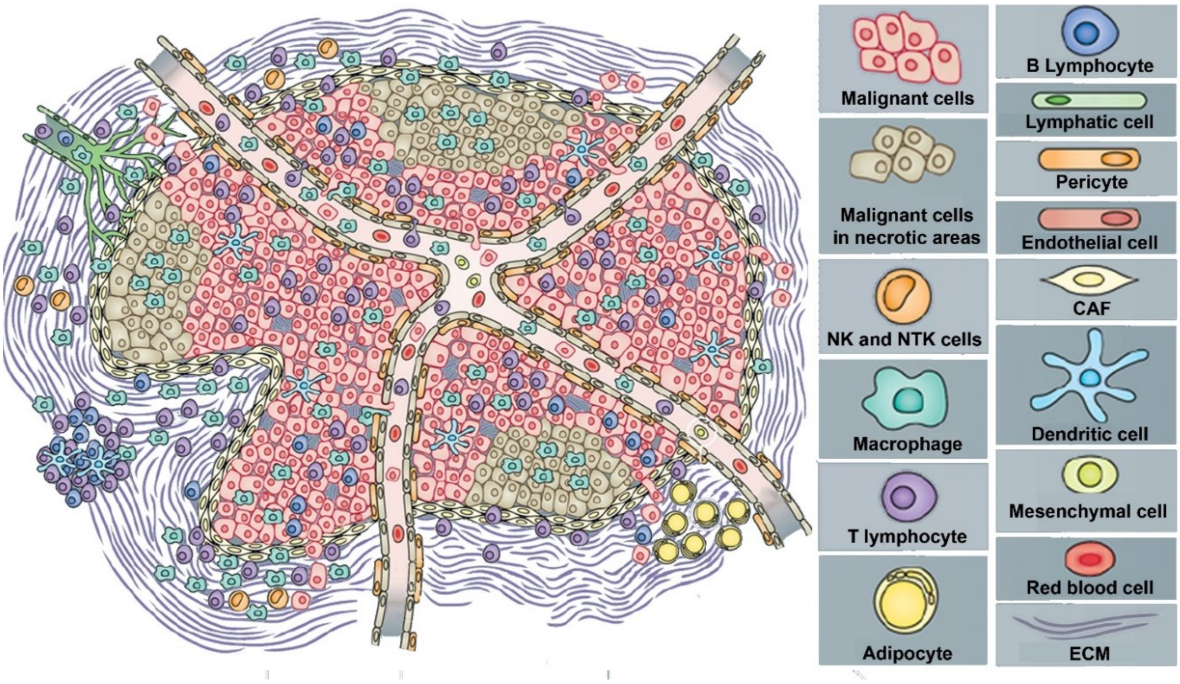

***Figure 7.1:** Schematic representation of TME complexity with different cell populations that can be found (adapted from [47])*

Cellular components of TME

Endothelial cells

Endothelial cell are the cells responsible for angiogenesis and therefore supplying nutrients, removing wastes and providing new routes for metastatic cell spreading. The most known signaling pathways activating angiogenesis are the hypoxia-inducible factor (HIF), induced by the hypoxic conditions in the TME, vascular endothelial growth factor (VEGF) and platelet-derived growth factor (PDGF) [50]. Together with endothelial cells, pericytes associates on the external surface of blood vessels and controlling endothelial cell signaling and capillary permeability. VEGF and hypoxia are potent activators of pericytes that, upon activation, dissociate from endothelial cells and promote their proliferation. Conversely, other factors – as sphingosine-1, Ang-1, PDGFB and metalloproteases – are shown to enhance pericytes recruitment on endothelial cell wall and vessel stabilization. However, the role of pericytes in this process is still poorly understood, with some signals promoting vessel stabilization or destabilization in a context and tissue dependent manner. In TME pericytes display dual role: in primary sites of colorectal carcinoma, pancreatic and prostate cancer, leaky vessels with reduced pericytes recruitment correlated with higher number of metastases; but, in liver metastases, higher presence of tumor circulating cells correlated with higher presence of stellate cells (hepatic pericytes) suggesting that these cells may support metastatic cell extravasation [51].

In a study from 1999 Tomlinson and colleagues compared angiogenesis pattern in 25 carcinoma and sarcoma tissue specimens. Carcinoma, displayed a homogeneous distribution of blood vessel, compared with sarcomas; together with this observation, authors reported a higher stromal cell infiltration in carcinoma TME. For this reason, sarcoma was defined as “One Compartment” tumor, where tumor mass is composed predominantly by mesenchymal malignant cells that secrete angiogenic soluble factors (VEGF, FGF, PD-ECGF and angiogenin). Carcinoma, on the other hand, was found with foci of fibroblast and myofibroblast infiltrations expressing the anti-angiogenic soluble factor TIMP-1 and was therefore defined as “Two Compartments” tumor. Authors concluded that angiogenesis resulted from a local equilibrium between pro-angiogenic and anti-angiogenic effects generating the discontinuous pattern of vessel distribution in carcinoma, whereas homogeneous vessel distribution in sarcoma was due to the absence of stromal anti-angiogenic interferences [52].

Among angiogenic factors in RMS, VEGF has proven to be one of the most important. In a xenogenic mouse model of RMS, derived from A653 human cell line, local and systemic injection of chimeric murine soluble VEGF receptor protein, able to neutralize both human and murine VEGF, showed complete suppression of tumor growth, drastic reduction of tumor vessels, and large necrotic areas together with upregulation of genes related to hypoxia in the tumorigenic tissue [53]. Autocrine signaling of VEGF has also been proved to sustain tumor growth of RMS cell lines *in vitro* and this could be inhibited treating cells with all-trans-retinoic acid [54]. Finally, in a cohort of 78 RMS patients, VEGF expression correlates with a poor prognosis and has been indicated as a potential prognostic factor and target for molecular therapy [55].

As mentioned previously, PDGF is another potent mediator of angiogenesis. In RMS the most overexpressed PDGF ligands are PDGF-CC and PDGF-DD and they are almost exclusively secreted by RMS cells. Among receptors, PDGFR-α (PDGF-CC receptor) is found expressed in both stromal and cancer cells, whereas PDGFR-β (PDGF-DD receptor) is mainly expressed in vascular stroma or rarely in ARMS tumor cells. PDGF inhibition proved to be effective in reducing cell proliferation, inducing apoptosis *in vitro* and *in vivo* and reducing tumor growth and stromal infiltration (macrophages, endothelial cells and fibroblasts) in a xenogenic mouse model [56]. This findings are in line with previous results obtained in mice, that showed how PDGFR-α is overexpressed in ARMS, since it is a transcriptional target of the fusion oncoprotein PAX3-FOXO1, and inhibition of PDGFR-α impaired tumor growth *in vitro* and *in vivo* [57]. Second phase clinical trials are considering Sorafenib, multi-kinase inhibitor targeting also VEGFR and PDGFR-β, has shown positive results in the treatment of soft tissue sarcoma, leiomyosarcoma, angiosarcoma and chondroma [58].

An interesting alternative, or complementary mechanism, for blood diffusion inside the tumor is vasculogenic mimicry (VM). Vasculogenic mimicry was described for the first time in aggressive melanoma by Maniottis and colleagues in 1999. Briefly, tissue sections showed interconnected loops of ECM and lined tumor cells with red blood cells contained in their cavities. These channels were negative for classical endothelial markers and positive for the PAS staining, therefore rich in polysaccharides and glycoproteins [59]. These functional tubular structures can provide nutrient supply and routes for metastatic cell migration as endothelial cells. VM have been reported in other tumors as breast, prostate, lung, rhabdomyosarcoma [60]. Two different cohorts of RMS patients showed the hallmarks of VM: the first reported between 13.6% and 27% of positive specimens for VM in patients with synovial sarcoma, mesothelial sarcomas or alveolar rhabdomyosarcoma, underlining also a correlation between VM and reduced survival in patients with mesothelial sarcomas and alveolar rhabdomyosarcoma [61]. The second study analysed a restricted cohort of 32 patients with RMS in the orbits. VM was identified in 11/32 patients with poorly differentiated histology and correlated with lower survival rates [62].

Immune cells

Both immune cells from innate and adaptive immunity can be found in the TME, exerting pro-tumorigenic or anti-tumorigenic functions in a time and context-dependent manner. Immune cells from the adaptive immunity that are more often reported in the TME are T-lymphocytes, B-lymphocytes, natural T killer cells (NTK) and dendritic cells; cells of the innate immunity are instead macrophages, polymorphonuclear leukocytes and natural killer (NK). The role of the immune system in TME is described by the three phases of the immunoediting model. An initial phase named “Elimination” describes a situation where innate and adaptive immune cells recognise malignant cells and promote their elimination, activating an inflammatory response. Eventually this situation reaches an “Equilibrium” phase where immune cells selected immune resistant tumor cells and the number of proliferating cancer cells is equal to the number of tumor cells killed by the immune response. Finally, resistant tumor cells overcome the immune control and elimination in the phase called “Escape” and in turn, tumor cells secrete soluble factors that modulate and polarize the immune compartment shifting them from an anti-tumorigenic to a tumor-sustaining phenotype [63]. The complete description of this intricate process would be too extensive for the purpose of this work. Additional information can be found in more specific reviews [64,65].

Macrophages are recruited in TME by a series of cytokines, chemokines and soluble factors derived from ECM degradation; among these signals CCL2, VEGF-A and endothelin are the most well-known. Tumor associated macrophages can derive form circulating monocytes, from differentiation of myeloid-derived suppressor cells (MDSCs) or directly from resident macrophages. Different states of macrophages activation have been reported but the main 2 subtypes are M1 and M2: the former has pro-inflammatory and anti-tumoral functions, is induced by IFN-γ and LPS, produces high levels of IL-

6, IL-12, IL-23 and TNF-α, and it also express higher levels of MHC class I and II required for antigen presentation. M2 macrophages exert anti-inflammatory, pro-tumorigenic and pro-angiogenic properties, express high levels of IL-10, mannose receptor, IL-1 receptor antagonist together with reduced antigen presenting ability. However, this classification is oversimplified and other classes of macrophages has been described [66,67]. Different population of tumor infiltrating lymphocytes (TILs) can infiltrate the TME: T_h1 produce IFN-γ, polarizing macrophages towards M1 phenotype, T_h2 produce IL-4 eliciting humoral response and activating T cytotoxic lymphocytes in combination with T_h1, however, they are also responsible in some contexts for M2 polarization of macrophages. Tregs exert pro-tumorigenic functions suppressing $CD8^+$ cytotoxic lymphocytes via secretion of IL-10 and TGF-β and Th17 derive from naïve CD4+ T cells and are reported to be pro-tumorigenic or anti-tumorigenic in a context dependent manner [68].

The role of the immune infiltrate in RMS is still largely unexplored. In a cohort of 50 soft tissue sarcoma patients, D'Angelo and colleagues verified the expression of the immune suppressing molecule programmed death-ligand (PD-L1). Lymphocytes and macrophages were found in 98 and 90% of the samples respectively. The most abundant infiltrating populations were the CD3+ (TILs), CD4+ (T-helper cells), CD8+ (cytotoxic T-cells) and FOXP3+ (T-reg). Low CD3+ and CD4+ infiltration appeared to correlate with better survival, in contrast with previous studies showing a positive correlation between CD3+ and CD4+ infiltrates and survival. Higher number of CD8+ cells was found in patients with larger tumors or metastatic disease. However, this study presents some critical limitations: the low number tumor specimens representing each histological subtype (20 different subtype represented by 1 or 2 specimen each) and samples representing the same malignancy but with different stages of the disease [69].

A recent work divided a cohort of 25 RMS (13 embryonal,11 alveolar and 1 sclerosing) in 4 categories based on the expression of PD-L1. Although RMS cells were negative for PD-L1 expression, immune infiltrating cells (CD3+ lymphocytes and CD68+ macrophages) and surrounding the tumor showed different pattern and grades of PD-L1 positivity. 'Immune-inflamed' RMS (4/25 of the specimens), displayed expression of PD-L1 in immune cells surrounding and within the tumor burden, 'immune-excluded' RMS (5/25) with PD-L1 staining present in immune cells retained in the surrounding stroma. Finally 7/25 of RMS samples were defined as 'Immune-desert' with very few T-cells in either the parenchyma or the stroma of the tumor burden [70].

In vitro, experiments demonstrate how cytotoxic drugs, as doxorubicin, increases the expression of macrophage inhibitory factor (MIF) – an important soluble factor involved in oncogenic transformation, tumor progression and immunosuppression – in RMS cell lines. MIF induces the recruitment of pro-tumorigenic CD33+ CD14+ Myeloid Derived Suppressor Cells (MDSC) from Peripheral Blood Mononuclear Cells (PBMC). Inhibition of MIF impairs migration potential of RMS cells, designating MIF as a potential target to restore immune sensitivity in RMS TME and preventing metastatic cell migration [71]. Immune therapy in sarcomas is still largely undeveloped, however some studies as the ones presented before [69,70] highlighted the complexity and the heterogeneity of immune infiltrates across sarcoma subtypes. In general, 2 groups of sarcomas can be defined according to immune involvement: "Hot" tumors, with high number of immune infiltrate (TILs or tumor associated macrophages -TAM-) that are more prone to respond to immunomodulatory therapies; and "Cold" tumors, that are not recognised by the immune system. "Hot" sarcomas are shown to respond to checkpoint inhibitors (anti-CTLA-4 and anti-PD1) in mouse models of metastatic osteosarcoma and are giving promising results in clinical trials. However, progresses in this field are still limited due to the limited availability of checkpoint inhibitors. “Cold” tumors have shown to respond to cytokine treatment, immune cell engineering and tumor vaccines; all these approaches aimed to activate the immune system and help recognition tumor cells. Clinical trials demonstrate the feasibility and the potentials of these approaches in particular activating *ex vivo* autologous dendritic cells to target malignant cells [58].

Fibroblasts

Fibroblasts are the main players in ECM remodelling. In physiological condition they remain quiescent but, upon wound healing response, they transiently activate to myofibroblasts, with enhanced contractile and secretory properties. They synthetize new ECM proteins, modulate immune response and stimulate angiogenesis. At the end of the regenerative response, myofibroblasts can deactivate, returning to a quiescent state, or go through programmed cell death. In pathologic condition of chronic inflammation, myofibroblasts become from transiently activated to stably active, via TGF-β signaling and epigenetic regulation, resulting in drastic ECM remodelling and impairment of tissue functionality. This fibroblast population associated to fibrosis is then called Fibrosis Associated Fibroblast (FAFs). Similarly, activated fibroblasts in the tumor microenvironment has different features compared to myofibroblasts and FAFs, and are termed as Cancer Associated Fibroblasts (CAFs). CAFs in tumor stroma are stably active, secrete pro-tumorigenic growth factors and chemokines, together with ECM and tissue-remodelling enzymes. They exert immunomodulating effects in the TME, sustaining cancer metabolism, angiogenesis and drug resistance [72]. There is a growing interest regarding CAF and their role in TME; emerging evidences are also identifying a classification of CAF similar to the one of TAM and TIL, with CAF subpopulation with different functions and properties, some of them reported to be also tumor suppressing. Other insights on the role of fibroblasts in tumor microenvironment can be deepen in more specialized reviews [73–76].

The role of fibroblasts in sarcomas is still largely unexplored. Tarnowski and colleagues showed upregulation of MIF in several RMS cell lines. MIF acts in a paracrine loop on the receptors CXCR4 and CXCR7 increasing RMS cell adhesion but not proliferation, survival or chemotaxis. MIF conditioned medium displayed angiogenic potential. Moreover, *in vivo* studies conducted on mice showed that RMS cells with impaired MIF secretion formed larger tumors with superior stromal contribution and higher number of circulating RMS cells in the peripheral blood, indicating MIF as an inhibitor for CAF recruitment in sarcoma TME [77]. This view agrees with the “One compartment” tumor described by Tomlinson and colleagues discussed above [52]. Since information on CAF in RMS tumor stroma are scarce, no clinical trials or therapeutic approaches targeting this cell population have been developed yet.

Acellular components of TME

As previously anticipated, we refer to acellular components of the tissue to all the secreted proteins that form the natural scaffold in which cells are embedded. Following the classification outlined by Naba and colleagues, these proteins can be divided in two main categories: “Core” ECM proteins, further subdivided in collagens, proteoglycans and ECM-glycoproteins, and “ECM-associated” proteins that comprise ECM-affiliated proteins, ECM regulators and secreted factors [48,49].

Core ECM proteins

Collagens have a crucial role in conferring mechanical properties and structural architecture to the tissues; 28 type of collagens are reported to date, they are combination of 3 α chains that assemble in at least one triple-helix domain. Collagen fibrils can be composed of homotrimeric (e.g. collagen II) or heterotrimeric α chains (e.g. collagen IX). Different α chains can derive from alternative spicing variants of the same collagen gene. The large heterogeneity among α chains reflects the diversity of collagens, with triple-helix domain that can range from 96% to less than 10% of the length. In turn different collagens can organize in fibrils, networks or they associate along with fibrils as in the case of fibril-associated collagens with interrupted triple-helices (FACIT) [78].

RMS cell lines were extensively used between '80 and '90 to study collagen matrix deposition *in vitro* but some experiments report contradictory results [79–81]. Among collagens produced by RMS cell lines, collagen XIX, member of the FACIT family, is strongly upregulated upon *in vitro* induction of differentiation. In response to differentiation stimulus, ERMS cell line CCL136, besides increasing collagen XIX deposition, changed morphology from polygonal to structures resembling myotubes and upregulated genes responsible for differentiation, as myosin heavy chain (MyHC) and α-actinin [82]. More recently collagen XIX, and in particular its non-collagenous domain 1 (NC1) showed anti-tumor properties on melanoma cell line inhibiting migration and invasion acting through $\alpha v\beta 3$ integrin and PI3K/AKT/mTOR pathway [83].

Proteoglycans (HSPGs) are proteins with highly glycosylated sidechains (glycosaminoglycans - GAGs). GAGs confer to proteoglycans negative charge, enabling them to sequester and store water, cations and positively charged molecules as cytokines and growth factors. Rather than structural support, proteoglycans have a spacer function serving also as a reservoir of soluble factors that can be released upon proteolytic cleavage of GAGs sidechains [84].

In the field of sarcomas, glypicans and the relative degrading enzyme, heparanase, are reported to be remarkably active. They are getting attention for they roles in enhancing proliferation and migration of tumor cells but also for their restricted expression in embryonic tissues and complete absence in adults, suggesting them as optimal target for molecular therapy. Among HSPGs, the most expressed in sarcomas are GPC3 and GPC5, the latter is amplified in 20% of ARMS and associated in particular with the PAX7-FOXO1 alteration, enhancing the action of heparin-binding cytokines and growth factors involved in RMS tumorigenesis, as FGF2, HGF, Hh and Wnt1A. Heparanase levels however, did not show any correlation with tumor aggressiveness or patient outcome in soft tissue sarcoma patients [85]. Preclinical studies showed the efficacy of an heparanase blocking antibody, roneparstat, on a xenogenic model of Ewing sarcoma, reducing tumor growth alone or even with better result when used in combination with antiangiogenic treatments [85]. GPC3 is highly expressed not only in RMS but also on others pediatric solid embryonal tumors as hepatoblastoma, Wilms tumors and rhabdoid tumors. The protein core of GPC3 has been shown to act via Wnt/β-catenin pathway. Since the interest in targeting this protein is particularly high, thanks to the advantages of high specificity and low toxicity mentioned above, a growing number of therapeutic approaches are emerging. Among these, vaccines, monoclonal antibodies, antibody-drug conjugates, bispecific antibodies, cytolytic T lymphocytes (CTL), and chimeric antigen receptors are administered to different type of sarcomas [86].

Glycoproteins are a large group of proteins that are functionalized with oligosaccharide chains by post transcriptional modifications. This large heterogeneous group mediate many functions: from ECM assembly to cell adhesion, proliferation and migration. The most representative proteins of this category are laminins and fibronectin [78]. In a study from 1991, Vogel and colleagues studied the different pattern of laminin and fibronectin deposition in a methylcholanthrene-induced murine model of rhabdomyosarcoma. They reported that in histologically less differentiated areas of RMS, with vimentin positive and myoglobin negative spindle shaped tumor cells, there was a prominent deposition of fibronectin and absence or discontinuous deposition of laminin. Conversely, well differentiated tumor areas, polygonal shaped, desmin and myoglobin positive cells, were surrounded by continuous layer of laminin and considerably less fibronectin, that was not directly in contact with cells [87]. Similarly, *in vitro* experiments compared the adhesion abilities of carcinoma and sarcoma cell lines. Carcinoma cells were shown to adhere firmly to ECM deposited by endothelial cells; however, immunoprecipitation of laminin, but not of fibronectin and collagen IV, profoundly impaired adhesion and flattening of carcinoma cells. On the other hand, also Ewing sarcoma cells adhered strongly to endothelial cells ECM, but depletion of fibronectin by immunoprecipitation inhibited cell adhesion and conversely, depletion of laminin or collagen IV had no effect [88]. In a more recent study conducted on 65 patients affected by osteosarcoma, authors showed: a significantly higher expression of the proteoglycan syndecan 4 (SDC4) and fibronectin in high grade osteosarcomas and correlations between SDC4 expression and larger tumor size, distant metastases and poor overall survival. Fibronectin overexpression was associated with distant metastases and poor overall survival [89].

ECM-associated proteins

The “ECM-associated” proteins includes ECM-affiliated proteins, that share some domains with ECM proteins or are known to be associated with ECM; ECM regulators: matrix-remodelling enzymes such as transglutaminases and matrix metalloproteinases, and secreted factors such as growth factors and cytokines [49]. This category covers hundreds of proteins and only the most representative will be discussed here. In a cohort of 33 RMS patients, the matrix metalloproteinases 1, 2 and 9 have been reported significantly higher expressed in alveolar compared to the embryonal subtype. Moreover, expression of the MMP-9 has been reported in the vascular and perivascular stroma, suggesting that other cell type can cooperate to metastatic progression of RMS [90]. It is important to underline that the interaction network between cells, ECM and secreted factors is highly interconnected and the protein expression is highly dependent on the microenvironment in which cells are integrated. As an example of this, Ito and colleagues demonstrated that cyclooxygenase-2 (COX-2), an enzyme that converts arachidonic acid into prostaglandins and thromboxane, is overexpressed in 60 to 82% of sarcomas. RMS cell lines cultured on fibronectin were shown to upregulate, with about a 2-fold increase, both COX-2 and MMP-2. Moreover, addition of COX-2 substrate, prostaglandin E_2 (PGE_2), on RMS cells cultured on fibronectin, secretion of MMP-2 increased from 95 to 160%; conversely inhibition of COX-2 lead to reduction of MMP-2 secretion by about 60%, probing the role of COX-2/ PGE_2 in RMS invasiveness [91]. Transforming Growth Factor β (TGF-β) is also found associated with ECM and it has been reported as an inhibitor of myogenic differentiation. Bouchѐ and colleagues studied the role of TGF-β on ERMS cell line (RD) differentiation, proving that, reducing the concentration of active TGF-β in the culture medium with phorbol ester 12-O-tetradeca noylphorbol-13-acetate (TPA), cell proliferation was reduced and myogenic differentiation activated. However complete depletion of TGF-β suppressed tumor growth but failed to induce differentiation [92]. A more recent study, also conducted on RD cell line, showed induction of myogenic differentiation upon TGF-β gene silencing together with growth inhibition, contrasting the results from Bouché and colleagues [93]. This ambiguity reflects the need to appropriate models to study biological effects, indeed none of the previous models considered the latent TGF-β associated with ECM, and this could strongly influence the availability of TGF-β in the TME.

Tumor migration and metastases

With a general description of the tumor microenvironment, in its cellular and acellular component, we described the main players in the biological process of metastatic migration. For cancer cells, the route from the primary site to metastatic niche is a multistep process that involves: the support from stromal cells, adhesion to different substrates (composing the ECM of diverse tissues), directional migration through gradients, entering and surviving in the blood stream, recognition of the metastatic site and extravasation to finally start growing and repeat the process. In the next paragraphs we will summarize the strategies for cancer cell migration with a focus on the proteins that mediate the interactions between cells and ECM reporting, when it is possible, the information concerning RMS.

Mechanisms of cancer cell migration

The complexity of the TME, in terms of the different stromal populations and ECM topology, regulates the multiple strategies adopted by cells for spreading in the surrounding tissues. Cancer cells integrate multiple cues from the TME as ECM binding sites availability, mechanical properties (e.g. stiffness), presence of cell-cell adhesion and gradients of pro-migratory factors. Integration of these cues results in the choice from different migration strategies (Figure 8.1A). A main distinction can be drawn between single cell and collective migration.

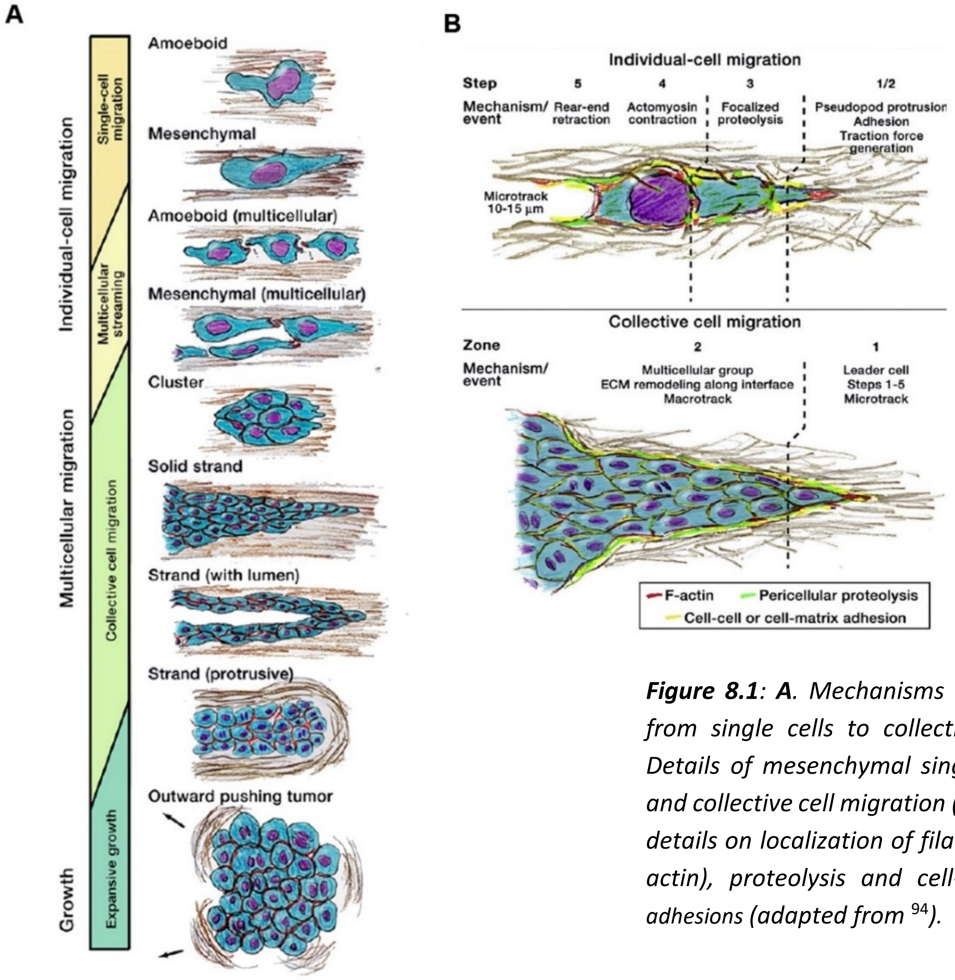

Figure 8.1: ***A***. *Mechanisms of cell migration, from single cells to collective migration.* ***B***. *Details of mesenchymal single-cell migration and collective cell migration (solid strand) with details on localization of filamentous actin (F-actin), proteolysis and cell-cell or cell-ECM adhesions (adapted from [94]).*

Single cell migration results from reduced cell-cell adhesions and directional movement of cancer cells following a pro-migratory stimulus. This can occur both in absence or presence of cell-ECM interactions, resulting in ameboid or mesenchymal migration respectively. Cells that display ameboid migration adopt spherical shape, reduced adhesion sites, membrane blebs and often absence of proteolytic degradation of the ECM. Indeed, rather than create trails through the ECM and adhere to substrates, ameboid cells squeeze through tissue fibers. Conversely, mesenchymal migration strongly relies on cell-ECM adhesions, giving to cells a peculiar spindle-shape morphology with a leading edge on the invasive front and a trailing edge on the opposite site. On the leading edge, focal adhesions and actin cytoskeleton polymerization ensure strong attachment to the substrate and mechanical coupling between ECM and cytoskeleton. Proteolytic degradation occurs at the trailing edge and on lateral surface of the cell to generate a track for following invasive cells (Figure 8.1B).

Single cell migration can be described in 5 steps: 1) protrusion of the cytoskeleton and cell polarization establishing the leading and the trailing edge; 2) engagement of the ECM by the leading edge, that couple ECM with cytoskeleton via adhesion proteins; 3) recruitment of proteases to locally degrade ECM and open the way for cell advancement; 4) small GTPase Rho inducing contraction of the actin cytoskeleton via myosin II; 5) detachment of the trailing edge and recycling of adhesion proteins from the trailing to the leading edge.

Collective cell migration requires a higher level of organization and the retention of cell-cell contacts. One or more “leader” cells, usually exhibiting mesenchymal morphology and pericellular proteolytic properties, protrude from the tumor burden (Figure 8.1B). Depending from cell type, tissue stiffness and density, invading cells can arrange in morphologically different types of strands: cell clusters, solid strands, strands with empty cavity or strands with blunt end.

Finally, expansive growth occurs in tissue with limited physical confinement, in these tissues proliferation of malignant cells generates a pression that passively displaces cells, contributing to collective migration without requirement of adhesion or proteolysis [94].

RMS modes of migration has been investigated for ARMS and ERMS cell lines, in a 3D model with spheroids embedded in collagen I matrix. ERMS cells showed morphological characteristics of mesenchymal motility with elongated shape, whereas ARMS cell lines showed rounded or ellipsoid morphology and membrane blebs. Enhanced metastatic potential of ARMS compared to ERMS seems to be due to ameboid migration, that has higher velocity compared to mesenchymal movement. Oversimplifying, the mesenchymal motility is regulated by Rac pathway and ameboid motility is regulated by Rho/ROCK pathway. These two pathways are interconnected to establish molecular circuitry with additional “control” levels that confer to cells the ability to shift from mesenchymal to ameboid invasion depending on the TME. In ARMS it has been demonstrated that the migration in collagen I matrix is ROCK dependent. In particular ARMS cell lines downregulate RhoE, inhibitor of ROCK kinase activity, and display higher expression of the GTPase Activating Protein (GAP) ARGHAP25, inhibitor of Rac activity, regulated by ROCK II [27]. However, it is important to remember that cancer cell migration in physiological conditions is characterized by plasticity, the ability of invading cells to switch from one migration strategy to another, and the mutual influence between cancer, stromal cells and ECM defined as reciprocity.

Role of integrins and adhesion molecules in migration

The main class of proteins mediating mechanical coupling between the ECM and cell cytoskeleton is the integrin family. Integrins are transmembrane heterodimeric proteins composed of one α and one β subunit. Up to date 18 α and 8 β subunits have been catalogued; these associate in 24 different combinations that recognise distinct ECM molecular partners. Upon binding of extracellular ligands, and in cooperation with receptor tyrosine kinases (RTKs), activation of integrins has a dual role:

1) orchestrating phosphorylation cascade of the Ras, Rac and Rho pathways via focal adhesion kinase (FAK) and Src-family kinases (SFKs), that control assembly, contractility and turnover of the focal adhesions;

2) the mechanical coupling of β integrin subunit cytoplasmic domain to the actin cytoskeleton via adaptor proteins (Figure 9.1A).

In metastatic cascade, besides migration and matrix remodelling, integrins are involved in other important process such as bypassing the programmed cell death in absence of substrate adhesion (anoikis), and clustering of cancer cells with platelets and leukocytes in the bloodstream, forming small emboli that support tumor cell survival and colonization of distant organs [95,96].

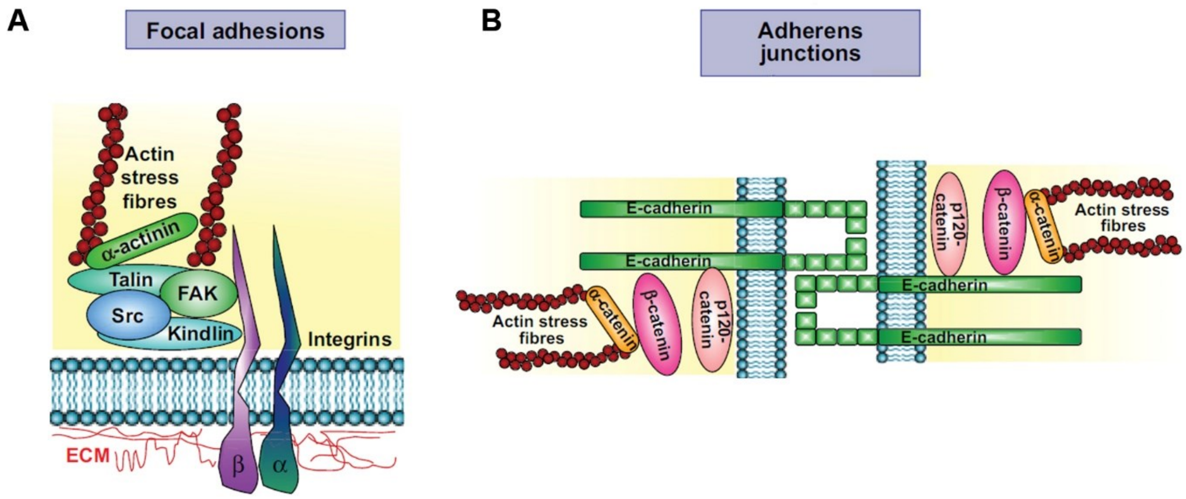

***Figure 9.1**: **A**. Molecular assembly of integrin focal adhesion complex. Cytoplasmic domain of integrin β subunit interacts directly with focal adhesion kinase complex (FAK) and with Src via the molecular adaptor protein Kindlin. Molecular coupling with actin cytoskeleton in mediated through Talin and α-actinin. **B**. Molecular assembly of cadherins adherent junction complex. Cadherins extracellular domain bind homologous cadherins on adjacent cell surface via Ca^{2+} binding domains. Cytosolic domain mediate mechanical coupling with cytoskeleton via p120-catenin and β-catenin that mediate interaction with α-actinin and actin cytoskeleton (adapted from [97]).*

In transfected ERMS cell line (RD), expressing integrin $\alpha 2\beta 1$, it has been shown that this surface receptor, and in particular the cytoplasmic tail of the $\alpha 2$ subunit, mediates the RhoA dependent morphological shape switch upon EGF stimulation from a steady state condition to spreading phenotype with enhanced filopodial and lamellipodial protrusions [98]. The expression of cell-cell adhesion molecule N-cadherin and $\alpha 9$ integrin, have been shown to be dependent on Notch pathway, that controls cell invasiveness in RMS. Pharmacological inhibition of this pathway reduced cell adhesion of ARMS and ERMS cell lines *in vitro*, proving that this mechanism is shared between the two subtypes. Transcriptional activators of the Notch pathway are also found to interact with N-cadherin and integrin $\alpha 9$ genes, proving that these two adhesion proteins are positively regulated target genes upon the Notch activation. This prompts that Notch pathway can be targeted for a molecular therapy approach [99].

Cadherins are one of the major proteins controlling cell-cell adhesion, they are single pass trans-membrane glycoproteins with multiple Ca^{2+} binding sites on the extracellular domain that mediate homophilic recognition of cadherins on the surface of adjacent cells. The cytosolic domain contacts the actin cytoskeleton via p120-catenin/β-catenin/α-actinin adaptor complex (Figure 9.1B). Recruitment and turnover of cadherin complexes are highly dynamic and regulated by clatrin- and caveolin-dependent endocytosis.

Additional levels of cadherins regulation derive from mediators downstream integrin activation, as Src, FAK, integrin linked kinase (ILK) and small GTPases. This crosstalk reflects the plasticity already discussed between the different mechanisms for cell migration; however, the precise interactions among these mediators has to be clarified yet, and the contribution of other elements, as reactive oxygen species (ROS) and mechanotransduction, are emerging [97].

Expression of cadherins in RMS is reported to be altered. In 3 ERMS cell lines (RD, A-204 and HS 729) neural cell adhesion molecule (N-CAM) is expressed only by RD, but it is highly sialylated, impairing its adhesion properties; whereas N-cadherin is not expressed in all three cell lines. N-CAM and N-cadherin are important mediators of myoblasts adhesion and fusion, ERMS impaired differentiation potential could also be sustained by downregulation of these proteins [100]. Caderin-11 has also been reported altered in ERMS cell lines and, interestingly, also in fusion negative ARMS. In normal skeletal muscle development, cadherin-11 is expressed but down-regulated after myotube formation [101]. Another study considered the expression of N-cadherin, M-cadherin and R-cadherin in RMS cell lines and tumor biopsies, showing downregulation of both M- and N-cadherins, compared to control myoblasts, and reporting R-cadherin overexpression in both ARMS and ERMS. Localization of M- and N-cadherins has been verified, displaying differential localization between ARMS and ERMS cell lines. ARMS expressed high levels of both in cell-cell contacts, whereas ERMS showed positive but abnormal (cytosolic) localization of N-cadherin and very scarce presence of M-cadherin on cell surface. Finally, inhibition of R-cadherin via siRNA silencing showed reduced proliferation [102]. More recently P-cadherin expression is shown to be expressed uniquely in PAX3/7-FOXO1 positive ARMS cell lines. P-cadherin gene is transcribed under the regulation of the Pax3 transcription factor and is also a transcriptional target of the ARMS fusion oncoprotein. During embryonic development, P-cadherin regulates myogenesis inducing myoblast transformation and migration. *In vitro* differentiation tests displayed also an impaired cadherin switch in a model of P-cadherin expressing C2C12 myoblasts: M- and N-cadherins, expressed by control differentiating myoblast, were absent in the P-cadherin expressing C2C12 myoblasts [103].

An example of cadherin function in tumour microenvironment is given by the outstanding work of Labernardie and colleagues that demonstrated that cell-cell interaction, between cancer associated fibroblasts (CAF , were indispensable for epidermoid carcinoma cell line (A451) collective invasion. Force transmission was mediated by heterotypic interaction of N-cadherin expressed by CAF and E-cadherin expressed by cancer cells. Force generation was also responsible for cytoskeleton reorganization that stabilized the interaction. Impairment in N-cadherin in CAF or E-cadherin in A451 cell line completely abrogated the cancer cell collective invasion [76].

Aims

This work aims at:

- The development of a consistent and reliable 3D model of ARMS able to recreate the complexity of the TME and to provide to cells a biomimetic scaffold, for the investigation of the metastatic migration.
  Two different approaches will be considered:

  - The “conservative” approach, that implied the decellularization of ARMS tissue to obtain a dECM based model that takes advantage of tissue-derived complexity in terms of protein composition and spatial architecture.
  - The “deconstructive” approach, that required the precise knowledge of the proteins composing ARMS ECM. Two bottom-up models were developed according to this approach: a Ultrafoam collagen I sponge in combination with a perfusion bioreactor and a hyaluronic acid/PEG hydrogel enriched with ARMS specific ECM proteins.

  These models will be used to recreate, in a dynamic and spatially defined context, the cellular interactions with extracellular proteins taking place in the tissues. It will also elucidate the mechanisms of cancer cells migration.

- Since integrins are the main adhesion proteins that mediate ECM recognition and mechanical coupling with the cytoskeleton, the role in ARMS cell motility and metastatic migration of these proteins will be investigated, *in vitro* and *in vivo*.

Materials and Methods

Cell lines and spheroids:

ARMS RH30 and cell line was kindly provided by the Solid Tumors lab (Prof. Bisogno, Padova, Italy). RH30-GFP were stably modified by Dr. Rampazzo, who transduced the cell line using pRRLsin.PPTs.hCMV.GFPpre vector. Cell lines were cultured in high glucose DMEM (Gibco, Dublin, Ireland) supplemented with 10% fetal bovine serum (Gibco, Dublin, Ireland) 1% 10000 U/mL penicillin/10000 μg/mL streptomycin (Gibco, Dublin, Ireland), 1% 200 mM L-glutamine (Gibco, Dublin, Ireland) in tissue culture flasks (Sarstedt, Nümbrecht, Germany) at 37°C, 5% CO2 and 95% relative humidity. For storage, cells were detached with 0.05% trypsin-EDTA (Sigma-Aldrich, St. Louis, Missouri, USA) and resuspended at 4 to 5 million per ml in freezing medium: 900 μl FBS and 100 μl DMSO (Sigma-Aldrich, St. Louis, Missouri, USA)

For spheroid formation: cells were detached from tissue culture flasks with Dissociation Buffer (Gibco, Dublin, Ireland), seeded in low glucose DMEM (Gibco, Dublin, Ireland) supplemented with 1x B27 (Gibco, Dublin, Ireland), 20 ng/ml EGF (ORF Genetics, Kopavogur, Iceland), 10 ng/ml FGF (ORF Genetics, Kopavogur, Iceland) and 1% 10000 U/mL penicillin/10000 μg/mL streptomycin using "U" bottom, ultra-low adhesion 96 well plates (Corning, New York, USA). Cells were seeded at 20 cells/μl in a total volume of 200μl for well. And kept at 37°C, 5% CO2 and 95% relative humidity for 5 days.

Alveolar rhabdomyosarcoma xenografts:

Xenograft procedure was carried out in accordance with the Italian Law (DL n. 16/92 art. 5) and was approved by the Ministry of Health and the local authorities (CEASA, protocol 304/2017). Twelve-week-old male and female Rag2$^{-/-}$γc$^{-/-}$ were used as recipients for flank subcutaneous injections and xenograft production. RH30 cells were detached from culture flasks with Dissociation Buffer and 2 million cells were prepared in 30 μl 1X PBS (Gibco, Dublin, Ireland). Xenogenic ARMS were harvested 21 days post injection.

Bioinformatics analysis:

Publicly available Gene expression datasets: GSE108022, GSE28511 and GSE66533 were downloaded from NBC Gene Expression Omnibus (www.ncbi.nlm.nih.gov).

Dataset n° GSE108022, with RNA-seq data from 101 RMS patients and 5 healthy donors, was selected as training set for cluster analysis due to the inclusion of healthy controls and high number of patients. Unfortunally no additional clinical information were included.

Cluster analysis of the genes related to the expression of ITGA5 and ITGB1 was run in "R" software, in collaboration with Bioinformatic Core Service at IRP "Città della Speranza". Expression levels are firstly normalized among patients – the total expression level of each patient was adjusted to the mean total expression level of the cohort – to compensate for patient to patient differences in total mRNA hybridization efficiency on the micro-array platform.

Genes were ordered according to the highest different expression among ARMS and ERMS groups. The top 100 differentially expressed genes were clustered together in accordance with their expression profile. Data were visualized with a heat-map where numeric values of expression were converted in a range of colours between red (assigned to the highest value) and blue (assigned to the lowest value).A second normalization for each gene, according to the mean expression level of healthy control, helped the visualization of single gene variation in expression levels on the heat-maps.
Enrichment analysis were performed with EGAN software (http://akt.ucsf.edu/EGAN/) on KEGG Pathways and Pathway Interaction Database (National Cancer Institute).

Immunofluorescence:

Samples were fixed in 4% PFA for 1 hours and dehydrated in sucrose (Sigma-Aldrich, Saint Louis, USA) gradients (10%, 15%, 30%). They were finally included in OCT embedding medium (Kaltek, Padua, Italy) using isopentane (Sigma-Aldrich, Saint Louis, USA) fumes chilled on liquid nitrogen. Samples were stored at -80°C until they were cut in 10 μm slices using Leica CM1520 cryostat (Leica Biosistems, Wetzlar, Germany). For immunofluorescence analyses, fixed cells or frozen sections were permeabilized for 15 min with 0.5% Triton X-100 (Bio-Rad, Hercules, USA), blocked for 15 minutes with 10% horse serum (Gibco, Dublin, Ireland) and incubated with primary antibodies overnight at 4°C. After washings, slides were then incubated 1 hour at room temperature with secondary antibodies Alexa Fluor-conjugated, protecting samples from light. Nuclei were counterstained with 4',6-diamidino-2-phenylindole (DAPI) (Sigma-Aldrich, Saint Louis, USA) on glass slides or with 1:10.000 Hoechst solution on multiwell plates. Antibodies used are listed in Table 2.1.

ARMS fresh tissue digestion:

Tumor masses were extracted from recipient mice, residual non-tumoral tissues were removed using sterile tweezers, forceps and scalpel. Tissues were then minced using sterile blades in a 6 wells multiwell plate and incubated with 3 ml of 0.5% mg/ml collagenase II, 0.5 mg/ml collagenase IV solution for 90 minutes at 37°C. Samples were collected in a falcon tube, centrifuged 1200 rpm for 10 minute and supernatants discarded. Pellets were transferred to a 6 wells multiwell plate and incubated with 2ml of trypsin-EDTA 0.05% for 90 minutes at 37°C. Trypsin was inactivated with 10 ml of culture medium and homogenates filtered through 70 μm and 40 μm cell strainers. Centrifugation at 1200 rpm for 10 minutes allowed the recovery of isolated cells from the pellet.

Flow cytometry and sorting:

Cells were first washed twice with PBS, detached from culture supports by incubation at 37°C for 5 minutes with Cell Dissociation Buffer (Gibco, Dublin, Ireland), counted and centrifuged 5 minutes at 1300 rpm. Pellets were resuspended in PBS supplemented with 3% FBS. For staining, 500.000 cells were transferred in a cytometry tube, resuspended in 100 μl and incubated in the dark with 5 μl of antibody solution (see Table 2.1) and 5 μl of 7AAD (Invitrogen, Invitrogen, Carlsbad, California, USA) for 20 minutes at room temperature. After washes in PBS 3% FBS, pellets were resuspended in 350 μl of PBS+3%FBS. The FC500 flow cytometer (Beckman Coulter, Brea, USA) was used for flow cytometry. For sorting, MoFlo XDP FACS (Beckman Coulter, Brea, USA) was employed. Sorted cells were plated in a T25 flask with 20% FBS supplemented culture medium, 24 hours later medium was substituted with standard culture medium.

Zymography:

50.000 cells were seeded in 6-well plate in 1,5 mL serum-free DMEM. The serum-free conditioned medium was harvested after 24h for zymography. Analogously, culture medium in the perfusion bioreactor was replaced with 6ml of serum free medium 24 hours before collection. Zymography was carried out as described by Frankowski and colleagues[104]. Briefly, 1% gelatine (J.T. Baker, Rodano, Italy) was added to the 12.5% polyacrylamide gel (Bio-Rad, Hercules, USA). After the developing, the gel was washed in 2.5% Triton X-100 (Bio-Rad, Hercules, USA) for 1 hour and then incubated in a development buffer containing 100 mM CaCl2 and 0.2% NaN3 (Carlo Erba Reagents, Cornaredo, Italy) overnight. Finally, it was stained in a Coomassie brilliant blue R-250 solution (Bio-Rad, Hercules, USA).

Real Time PCR:

Total RNA was extracted using RNeasy Plus Mini kit (Qiagen, Hilden, Germany) following the instructions. RNA was quantified with NanoDrop-2000 spectrophotometer. For all the samples 0,5 μg of total RNA was reverse transcribed with MultiScribe Reverse Transcriptase (Invitrogen, Carlsbad, California, USA) in a 10 μL reaction containing: 2 μl Buffer 10x (Applied Biosystems, Foster City, California, USA), 0,8 μl dNTPs (Applied Biosystems, Foster City, California, USA), 2 μl of random primers (Applied Biosystems, Foster City, California, USA), 1 μl RNase OUT (Invitrogen, Carlsbad, California, USA) and 3,2 μl RNase free water (Qiagen, Hilden, Germany). Real Time PCR reactions were performed using a Roche LightCycler II real-time PCR (Roche, Basel, Switzerland); reactions were carried out in duplicate using Sybr Green master mix (Applied Biosystems, Foster City, California, USA) and primer mix (final concentration, 200 nM) in a final reaction volume of 15 μL containing: 10 μl Sybr mix (Invitrogen, Carlsbad, California, USA), 2 μl primers, 1 μl BSA (Invitrogen, Carlsbad, California, USA) and 2 μl RNase free water (Qiagen, Hilden, Germany). Relative quantifications (RQ) were calculated by $\Delta\Delta$Ct methods. GAPDH was used as reference gene for normalization. Primer sequences used are listed in Table 2.2.

Anti-ITGA5 siRNA transfection:

Cells were detached from culture flask and counted as previously described. 50.000 RH30 cells were plated on each well of a 12 multiwell-plate (Sarstedt, Nümbrecht, Germany) in 1 ml of culture medium. 24 hours after seeding, transfection buffer was prepared mixing 100 μl serum free medium, 5,6 μl of 20μM ITGA5 siRNA (SantaCruz Biotechnology, Dallas, Texas, USA) and 2 μl of Mirus TransIT-X2 Transfection Reagent (Mirus Bio, Wisconsin, USA). The mix was incubated at 37°C for 20 minutes. 106,28 μl of the transfecting solution were then added to each well of the 12 well plate (final siRNA concentration 100nM). As a control a siRNA negative (SantaCruz Biotechnology, Dallas, Texas, USA) was used, this siRNA molecule is designed to not bind to any of mRNA. 48 hours after silencing, cells were detached with Cell Dissociation Buffer and used for further analysis.

In vitro cell migration tests:

Cells were detached and counted using non enzymatic treatment as described above.

Migration assay was assessed using 8 μm-pore transwell inserts (Sarstedt, Nümbrecht, Germany) in a 24-well plate. A solution with fibronectin at concentration 66 μg/ml was used to coat the inner and outer surface of the transwell membrane. Trans-wells with coating solution were kept in the incubator for 1 hour. 75.000 cancer cells were seeded in the upper chamber in 200 μl of serum free medium, and the lower chamber was filled with 600 μl of serum free medium (or standard medium as a positive control). After 24h, membranes were fixed in 4% PFA (Sigma-Aldrich, Saint Louis, USA) and stained with 1:10.000 Hoechst solution (Life Technologies, Carlsbad, California, USA) for 15 min. Pictures were taken using a Zeiss Axio Observer (Carl Zeiss, Oberkochen, Germany) microscope before and after cleaning the inner side of the membranes with cotton wool. Transmigrated cells were quantified using FIJI software.

Invasion assay was performed using 50 μl Matrigel (Corning, New York, USA), instead of fibronectin solution, to coat only in the inner side of the chamber. After Matrigel reticulation, 75.000 cancer cells were seeded in the upper chamber, and the lower chamber was filled with 600 μl of serum free medium (or standard medium as a positive control). Images of total cell number were taken 24 hours after seeding with Zeiss Axio Observer microscope. After cleaning the inner side of the membrane with cotton wool, images were taken to count cells that invaded the Matrigel coating and passed through the membrane.

Wound healing assay was performed with Ibidi "Culture-Insert 2 Well" (Ibidi, Gräfelfing, Germany) seeding 35.000 cells for each chamber and removing the insert 24 hours later. Cells, in culture medium, were followed with time-lapse microscope Zeiss Axio Observer equipped with temperature and humidity controller. Images were analysed with Fiji software and the cell tracking function.

Zebrafish *in vivo* injection:

Cells were detached and counted using non enzymatic treatment as described above. 1 million RH30 cells, ITGA5^{high} and ITGA5^{low}, were resuspended in 1 ml of serum free medium and incubated with 5 μl Vybrant Dil Cell-Labelling solution (Invitrogen, Carlsbad, California, USA) for 15 minutes at room temperature. Three sequential washes with 1x PBS followed, to remove the excess of dye. Cells were finally resuspended in 10 μl 1x PBS and loaded into borosilicate glass capillary needles (OD/ID: 1.0/0.75 mm, World Precision Instruments, Sarasota, Florida, USA).

The transgenic *Tg(fli1:GFP)* embryos [105] at 2 days post fertilization (dpf) were anaesthetized with 0.003% tricaine (Sigma-Aldrich, Saint Louis, USA) and positioned on a 10 cm Petri dish coated with 3% agarose. Approximately 200 cells were injected within the duct of Cuvier of the anesthetized *Tg(fli1:GFP)* embryos using a Pneumatic Picopump and a micro-manipulator (World Precision Instruments, Sarasota, Florida, USA). After implantation, zebrafish embryos were maintained at 33° C. Embryos showing less than 50 cells after four hours post-injection were discarded from the analysis. At least 30 embryos per group were analysed. The embryos were live photographed using a Leica B5000 inverted fluorescence microscope (Leica Biosistems, Wetzlar, Germany) at 4 24, 48 and hours post injection (hpi).

Statistical analysis:

Image based counts and measurements were performed with Fiji. For each analysis, at least five random pictures were used for data output. Data are expressed as means ± SEM and SD. Statistical significance was determined with GraphPad software using an equal-variance Student's t test or the Mann–Whitney U test for qRT-PCR analyses. A p value below 0.05 was considered to be statistically significant.

Conservative approach:

Decellularization:

Rag2$^{-/-}$$\gamma$c$^{-/-}$ mice were sacrificed, by cervical dislocation, 21 days after injection. Tumor masses were extracted and cleaned from undesired surrounding residual tissues (adipose, muscular, epidermal) with sterile tweezers, forceps and scalpel. Tumor mass were than weighted and measured with a calibre. Before processing the mass in pieces of approximately 250 – 300 mg, xenografts were cleaned with 10% povidone-iodide solution and washed twice with PBS 1x. Samples were kept overnight in PBS 1x supplemented with 3% (v/v) penicillin / streptomycin. The day after they started the decellularization process: 3 cycles of detergent and enzymatic treatment (DET). As a first step a maximum of 5 samples were incubated in 40 ml 1% (w/v) sodium dodecyl sulphate (SDS) solution for 4 hours at room temperature. After 2 washing steps in PBS 1x, samples were transferred to 40 ml tube containing 2000 kU/ml DNase I (Sigma-Aldrich, St. Louis, Missouri, USA) in 1 M NaCl and incubated for 3 hours at room temperature. Finally, after 2 washes with PBS 1x, samples were left overnight at 4°C in of 1% (v/v) Triton x-100 (Bio-Rad, Hercules, USA) solution. During all the decellularization process, tubes were maintained in constant agitation on a roller shaker. At the end of the decellularization process, the obtained matrices were washed in 40ml PBS 1x supplemented with 3% penicillin / streptomycin at 4°C on roller shaker for 5 days, changing solution daily. After 5 days decellularized ARMS ECMs were used for recellularization or alternatively stored at -80°C in a cryovial with 700 μl FBS, 100 μl DMEM low glucose and 200 μl DMSO. After thawing, washing steps were repeated.

Recellularization with microinjector:

The day before seeding, dECM were soaked overnight in culture medium supplemented with 20% FBS. The day after, matrices were transferred in 35 mm diameter Petri dishes and fixed with a surgical pin to a PDMS support. 1 million RH30 or RH30 GFP^{+} cells were resuspended in 15 μl of PBS 1x and were transferred in a glass capillary for the injection in multiple sites of the dECM using a stereoscopic microscope equipped with Pneumatic Picopump and a micro-manipulator (World Precision Instruments, Sarasota, Florida, USA). The injected matrices were kept in incubator at 37°C, 5% CO_2 and 95% humidity for 1 hour before adding 2 ml of culture medium. Live & Dead assay from ThermoFisher (ThermoFisher, Waltham, Massachusetts, USA) was used according to manufacturer instructions at 4 and 7 days after seeding to determine cell viability inside the dECM.

Recellularized dECM were gently washed with PBS 1x, fixed in PFA 4% for 1 hour and processed as indicated in ‘‘*Immunofluorescence*’’ paragraph for cryo-sectioning. Alternatively, for total RNA extraction, samples were transferred in 2ml Eppendorf with a sterile iron bead and 1 ml QIAzol Reagent (Qiagen, Hilden, Germany) and then processed with Tissue Lyser (Qiagen, Hilden, Germany) 30 Hz for 3 minutes. Processed samples were stored at -80°C or processed as indicated in the “*Real Time PCR*” section.

Recellularization with U-Cup Bioreactor:

For perfusion 3D culture we used U-Cup bioreactor provided by Cellec Biotek (Basel, Switzerland) (Figure 2.1). Briefly the system is composed by a disposable bioreactor and a syringe pump (Harvard Apparatus, Holliston, Massachusetts, USA). Silicon adaptors (2) allowed the insertion of a 8 mm in diameter and 6 mm height cell culture support (4) in the culture chamber (1). Decellularized ECM were cut to shape using a biopsy punch (8mm, Galiazzo Bruno Snc, Padua, Italy) and soaked in culture medium supplemented with 20% FBS overnight. Ultrafoam (BD Bard, Warwick, UK) disks were cut with a 10 mm diameter biopsy punch and soaked in culture medium supplemented with 20% FBS for 1 hour. Lower silicon adaptor was inserted in the plastic holder of the U-Cup bioreactor using sterile tweezers, 8 mm diameter sterile plastic grid (3) allowed the perfusion of medium in the culture chamber while holding in position the scaffold. Ultrafoam or dECM were placed on the lower grid, than the upper silicone adaptor, with the relative plastic grid in position, closed the culture chamber; finally, upper plastic holder closed the U-Cup bioreactor.

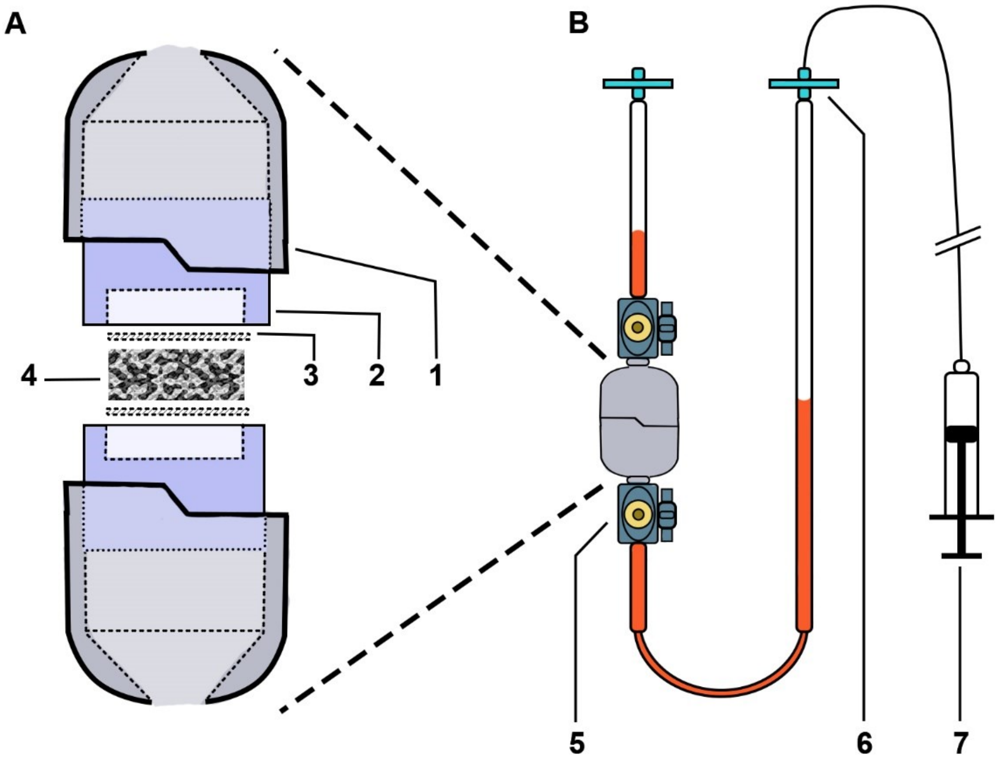

Figure 2.1: *Schematic representation of U-Cup bioreactor: A. detail of the culture chamber assembly: 1) culture chamber upper and lower holders; 2) silicone adaptors; 3) plastic grids; 4) cell culture support (dECM or Ultrafoam); 5) three-way valves; 6) 22 μm filters; 7) syringe pump.*

Once the bioreactor was mounted on the specific support, upper and lower valves (5) were cleaned spraying 70% ethanol. Cells were detached with trypsin 0.05%, counted as indicated above and resuspended at concentration 1 million cell per millilitre. Lower valve of the U-Cup was switched to allow infusion of 6 ml of culture medium below the culture chamber. Lower valve was then opened until level of medium is slightly above the upper valve in order to remove bubbles from the culture chamber. Upper valve was closed, and 2 ml of the cell suspension were injected. Finally, both valves were opened and cleaned with ethanol 70%. When the medium in the two arms of the bioreactor reached the same height (equilibrium) the culture chamber was placed in the incubator and connected to the syringe pump (7).

For the first 24 hours the “*seeding*” program of the pump was used:

1. 3 ml infusion – rate 1,2 ml/min
2. Pause 1 minute
3. 2,5 ml withdraw – rate 1,2 ml/min
4. Pause 1 minute
5. 2,5 ml infusion – rate 1,2 ml/min
6. Repeat from point 2

The day after the pump was stopped and bioreactor disconnected. Program of the pump was changed to “*culture*” mode. When the medium in the arms of the bioreactor reached the equilibrium, it was reconnected, and the pump restarted. Volumes and pauses in the “*culture*” mode remained unchanged, the infusion and withdraw rates were reduced to 0,3 ml/min. Medium was changed every 3 days. After 4, 7 or 15 days bioreactors were opened, the scaffolds recovered and gently washed in PBS 1x before being fixed in 4% PFA for cryo-sectioning or lysed with TRIzol for mRNA extraction.

Freeze & Thaw procedure:

Decellularized matrices were placed in 2 ml Eppendorf tube with 1 ml PBS. Tubes were deepened in liquid nitrogen for 5 minutes and then thawed in heated bath for 10 minutes; cycles are repeated 5 times. After the procedure matrices were soaked overnight in culture medium supplemented with 20% FBS and used as standard dECM from this point on.

Deconstructive approach:

Proteomic:

For proteomic analysis fresh ARMS tissue was processed as indicated in protocol published by Naba and colleagues [106] using the “Compartment Protein Extraction Kit” (Millipore, Burlington, Massachusetts, USA). Briefly, 75 mg of fresh tissues from ARMS xenograft were homogenized in 500 μl of Buffer C using tissue lyser 2 minutes at 30 Hz in 2 ml. After homogenization, samples were incubated at 4°C for 20 minutes on a tube rotator. Centrifugation at 16.000 g for 20 minutes at 4°C allowed the formation of the pellet and the recovery of the cytosolic fraction in the supernatant. Pellets were washed by resuspension in 400 μl Buffer W; incubation and centrifugation were repeated as described above and the supernatant was discarded. Pellets were then resuspended in 150 μl of Buffer N, incubated at 4°C for 30 minutes on a tube rotator and centrifuged at 16.000 g for 30 minutes at 4°C to collect the nuclear fraction in the supernatant; this passage is repeated twice. Pellets were resuspended in 100 μl Buffer M, incubated at 4°C for 30 minutes on a tube rotator and centrifuged at 16.000 g for 30 minutes at 4°C to collect the fraction containing transmembrane proteins. Finally, 200 μl of Buffer CS were added, samples incubated at room temperature for 30 minutes on a tube rotator and centrifuged at 16.000 g for 30 minutes at room temperature to collect the cytoskeletal proteins. Additional washing was performed with 150 μl of Buffer C incubating the samples at 4°C for 20 minutes on a tube rotator and centrifuged at 16.000 g for 20 minutes at 4°C; the supernatant was collected and added to the cytoskeletal fraction. All the fractions were flash frozen in liquid nitrogen for long term storage. Before flash freeze the ECM fraction, additional 3 washes with 500 μl of PBS 1x on a tube rotator for 5 minutes at 4°C and centrifugation at 16.000 g at 4°C for 5 minutes, allowed the removal of residual detergents. Pellets were stored at -80°C.

Pellets were resuspended in 50 μl 8M and 4 μl DTT (final concentration 10 mM), incubated 2 hours at 37°C in constant agitation at 1400 rpm (resuspension step). After incubation, samples were equilibrated at room temperature and 2,5 μl of 500nM iodoacetamide (IIA) were added, incubation for 30 minutes at room temperature followed (alkylation step). To each sample, 162 μl of ammonium bicarbonate pH8 in 2M urea solution plus 2 μl PNGaseF, were added; samples were incubated 2 hours at 37°C in constant agitation 1400 rpm (deglycolisation step). To digest ECM proteins, 10 μl Lys-C were added, and samples incubated 2 hours at 37°C in constant agitation 1400 rpm (digestion step). Addition of 6 μl of trypsin (500 ng/μl) followed and samples were left in constant agitation at 700 rpm at 37°C over-night. The day after, additional 3 μl of trypsin were added and incubation continued for other 2 hours at 37°C in constant agitation 1400 rpm (digestion II and III step). Digestion was inactivated adding 4 μl 50% trifluoro-acetic acid (TFA) then the pH was adjusted at 2. Samples were centrifuged at 16.000 rpm for 5 minutes at room temperature (acidification step). Quenched digests were centrifuged at 16000 g for 5 minutes, and supernatants were desalted using Oasis Solid-Phase Extraction (SPE) HLB cartridges (Waters Corporation, Massachusetts, USA). The cartridges were wetted with 1 μl of acetonitrile (ACN) 0.1% TFA and equilibrated with 1 ml of MilliQ water 0.1% TFA. Digested peptides were loaded on the sorbent, and then washed with 3% ACN 0.1% TFA. Finally, peptides were eluted with 0.7 ml of 60% ACN 0.1% TFA. The eluent was dried down using a SpeedVac (desalting step). Digested samples have been resuspended in 20 μl of 5% acetonitrile + 0.1 % formic acid (FA) before injection in the mass spectrometer. An Ultimate 3000 HPLC system coupled to a Q Exactive mass spectrometer (ThermoFisher, Waltham, Massachusetts, USA) was employed. The peptide mixtures were separated with a Biobasic C18 column, 5 μm, using a 3-45 % linear gradient of acetonitrile + 0.1 % TFA (mobile phase B) in H2O + 0.1 % TFA (mobile phase A) over at 110 minutes of analysis. Mass spec data have been acquired in data-dependent mode in the 300-1500 m/z mass range. Instrumental parameters were set as follow: source: ESI (+); precursor charge selection: from 2 to 5; precursor resolution: 10000; fragments resolution: 60000.

LC-MS/MS data have been processed by Proteome Discoverer 2.2 (ThermoFisher, Waltham, Massachusetts, USA) using the Sequest HT algorithm for proteins identification. Search parameters were set as follow: database, SwissProt; enzyme, Trypsin (max 2 missed cleavages); taxonomy, homo sapiens and *Mus musculus*; precursor mass tolerance, 10 ppm, fragment mass tolerance, 0.02 Da. Fixed modifications: carbamidomethyl (C). Dynamic modifications: oxidation (M, P); deamidation (N, Q), and phosphorylation (S, T, Y). An acceptable proteins false discovery rate (FDR) was set < 0.01 and a minimum of 2 non-redundant peptides was used to obtain proteins identification.

Western blot:

Protein concentration of each fraction, isolated from fresh ARMS tissue, was measured with “Pierce BCA Protein Assay Kit” (ThermoFisher, Waltham, Massachusetts, USA). Acrylamide gels were prepared as indicated by manufacturers using “TGX Stain-free FastCast Acrylamide starter kit, 10%” (Bio-Rad, Hercules, California, USA). 50 μg of protein from each fraction (cytosolic, nuclear, membrane proteins and cytoskeletal) were mixed with LDS Sample Buffer (4X) (Invitrogen, Carlsbad, California, USA) and loaded into the casted gel in a total volume of 20 μl. Gel electrophoresis was run with a voltage of 200 V and 160 mA for 1 hour. Proteins were transferred to PDVF membrane (Amersham, Little Chalfont, UK) with a voltage of 90 V for 1 hours at room temperature. Using the marker as reference, membranes were cut between 100 and 75 kDa, corresponding to the range of ITGA5 molecular weight (114 kDa), between 75 and 50, corresponding to Lam A/C molecular weight (74 kDa) and finally between 50 and 37 kDa to detect VIM (m.w. 53 kDa) and GAPDH (m.w. 35 kDa). Membranes were incubated separately with blocking solution (TTBS + 5% BSA) for 2 hours in a 50 ml Falcon tube on roller shaker. Primary antibodies (see Table 2.1) were used as reference of each fraction: ITGA5 as reference for membrane proteins, Lam A/C as reference for nuclear proteins, VIM as reference for cytoskeletal proteins and GAPDH as reference for cytosolic proteins. Antibodies were diluted 1:1.000 in TTBS + 1% BSA (m/v) and incubated with the corresponding membrane on roller shaker at 4°C overnight. Three washes with 20 ml TTBS, 15 minutes each, were performed on orbital shaker. Secondary antibody anti-mouse HRP-conjugated was used at dilution 1:10.000, in TTBS + 3% BSA, incubating the membranes for 1 hour on roller shaker at room temperature. Three washes are repeated as described above. HRP substrate, Pierce ECL (ThermoFisher, Waltham, Massachusetts, USA) prepared as described by supplier, was added to membranes and signal was recorded with UVITEC Alliance setting the exposition in automatic mode.

Ultrafoam scaffold digestion and evaluation of seeding efficiency.

At the desired time point bioreactors were stopped and the recellularized scaffold extracted from culture chamber using sterile tweezers. For fixation, sectioning and immunofluorescence, samples are processed as indicated for dECMs. To evaluate the seeding efficiency, the CyQUANT direct cell proliferation kit has been used (Invitrogen, Carlsbad, California, USA) after digestion of the collagen I Ultrafoam scaffold, that allowed the recovery of cells. Briefly, scaffolds were washes gently with PBS 1x and incubated for 1 hour with FBS depleted medium containing Collagenase IV (Gibco, Dublin, Ireland) 1 mg/ml in constant agitation at 37°C. Cells were then pelleted by centrifugation and resuspended in 400 μl of PBS 1x, 10 μl of cell suspension were diluted with 90 μl of PBS 1x and incubated at 37°C for 1 hour with 100 μl CyQUANT staining solution as indicated by the guidelines. Fluorescence was read with FITC filter. An aliquot of the cell suspension injected in the bioreactor was processed for CyQUANT quantification to determine the maximum fluorescence level derived from seeded cells. Seeding efficiency is finally calculated as the percentual ratio between fluorescence of cells extracted from bioreactor and control cells in the seeding suspension.

Hydrogel 3D culture:

Thiolated hyaluronic (HA) acid was produced in collaboration with Department of Pharmaceutical and Pharmacological Sciences (Padua University). Briefly, 250 mg of HA, 200 kDa mean molecular weight, were solubilized in 25 ml of anhydrous DMSO. Methanesulphonic acid was added in ratio 5:1 mole of HA, at 40°C in constant agitation until the solution was clear. 5 equivalents of carbonyl diimidazole (CDI) were then added and the reaction is maintained for 1 hour in constant agitation at room temperature. After correction of pH at 8 with triethylamine, 1,5 equivalents of 2-(Pyridyldithio)ethylamine (SPDC) were added for functionalization of (β,1-4)-D-glucuronic acid carboxylic groups and the reaction is maintained under stirring at room temperature overnight. 2,5 ml of a saturated NaCl solution were added to HA-SPDC, after 15 minutes the solution is precipitated drop by drop in cold ethanol and left at -20°C for 3 hours. The precipitate is recovered by filtration in Gooch filter. 5 washing steps were performed by serial resuspensions and centrifugations at 4000g for 5 min at 4°C: the first and the last washings were done resuspending the pellet with 30 ml of absolute ethanol, the second, the third and forth with ethanol 90% (v/v). Pellets were dried under N_2 gas flow. Dried pellets were resuspended in 8 ml of NaOH 0.25M, the pH adjusted at 7 with HCl 0.25M and the solution filtered through dialysis membrane – cut-off 12.000-14.000 Da – in ultra-pure water for 48 hours at room temperature. HA-SPDC solution is then lyophilized at -40°C with a pressure between 0.3 and 0.4 mbar for at least 48 hours.

The correct purification from unreacted SPDC was verified by TNBS assay: 2 mg of HA-SPDC pellet were resuspended in borate buffer 0.2 M pH 8 at the final concentration of 2.15 mM. 955 μl of borate buffer 0.2 M pH 9.3 were mixed with 25 μl of the 2.15 mM HA-SPDC solution.

As positive control we used a solution 2.15 Mm of Gly-Gly dimer, in 0.2 M pH 8 borate buffer, resuspended in 955 μl of borate buffer 0.2 M pH 9.3. As negative control 955 μl of borate buffer 0.2 M pH 9.3 was mixed with 25 μl borate buffer 0.2 M pH 8. To start the reaction 20 μl of 2,4,6-trinitrobenzenesulfonic acid (TNBS), solution 1 % (w/v) in H_2O (Sigma-Aldrich, St. Louis, Missouri, USA) were added to each sample an incubated 30 minutes at room temperature in constant agitation. Absorbance at 420 nm was measured with UV-vis spectrophotometer. The percentage of free amines was determined with the formula:

$$\%\, of\ free\ amines = \frac{Abs\ x}{Abs\ (GlyGly)}\ x\ 100$$

HA-SPDC, previously lyophilized, was resuspended at 1% (w/v) concentration in 50mM phosphate buffer, 2mM EDTA and 0.427 mmol DL-dithiothreitol (DTT), stirred for 1 hour to reduce the disulphide bond of the SPDC and obtain a thiolated functional group. The solution was transferred to a dialysis membrane (cut-off 12.000-14.000 Da) dipped in 1 l of 50mM phosphate buffer and 2mM EDTA solution, for 24 hours under N_2 gas flow. Next one day the dialysis solution was changed to EDTA 1mM in ultra-pure water. 24 hours later the solution is lyophilized for 24 hours at -40°C and pressure between 0.3 and 0.4 mbar.

To determine the degree of functionalization, or the number of repeating units (RU) functionalized with thiol groups, we conducted the Ellman assay: 2 mg of HA-SH pellet were resuspended in 1ml of 50mM phosphate buffer pH 7 and diluted in the same buffer at final concentration 0.1 mg/ml for the assay. Calibration curve is made by serial dilution of glutathione (GSH) at concentrations 0.005, 0.010, 0.015 and 0.020 mg/ml in 50mM phosphate buffer pH 7. A 5,5'-dithiobis-(2-nitrobenzoic acid) (DTNB) solution is prepared dissolving DTNB powder in 50mM phosphate buffer pH 7 at final concentration of 4 mg/ml; a solution of 1 M NaOH was added until buffer reaches yellow colouring. 3 μl of DTNB were added every 0.5 ml of sample (or standard) solutions. After 10 minutes absorbance has been read at 412 nm with a UV-vis spectrophotometer.

The mmol of thiolated RU of HA is calculated using the following formula:

$$mmol\ of\ RU - SH\ = \left(m\ \cdot Abs(x)\right) + q$$

Where m is the slope of the standard curve calculated on glutathione standards, q is the intercept and $Abs(x)$ is the absorbance value of the HA-SH sample. The percentage of thiolated residues relative to total number of RU is calculated as follow:

$$\% \, of \, RU - SH = \frac{mmol \, RU - SH}{mmol \, HA} \, x \, 100$$

Linear polyethylene glycol (PEG) (IRIS biotech, Marktredwitz, Germany), with a mean molecular weight of 1946 Da and functionalized with 2 maleimide groups the extremities, was used to crosslink with HA-SH chains. For each hydrogel, 1 mg of lyophilized thiolated HA was used. PEG was added in ratio 1:1 considering the functional groups (SH:Mal). PEG and HA-SH were weighted with analytical balance and sterilized under UV lights for 15 minutes before reconstitution. For example: using a thiolated HA with an efficiency of 20%, 0.48 mg of PEG were weighted for each 1 mg of HA used.

Cells were detached from flasks and counted as indicated above. 1 mg of thiolated HA was re-hydrated with 85 μl of complete medium. HA solubilized in culture medium was used to resuspend 500.000 cells, or 2 spheroids, and then transferred to a well of 96 multiwell plate. Lyophilized PEG is resuspended in 15 μl of PBS 1x and added immediately to the cell suspension in HA, while mixing with the tip (Figure 2.2). For HA-PEG hydrogels enriched with fibronectin, fibronectin solution (Sigma-Aldrich, St. Louis, Missouri, USA) at 1 mg/ml concentration was added to culture medium used for HA resuspension at final concentration of 1 μg/ml. Hydrogels formed instantaneously, 100 μl of culture medium was added after 24 h, medium was then changed every 2 days. Imaging of the hydrogels was performed using Zeiss LSM 800 confocal microscope (Carl Zeiss, Oberkochen, Germany).

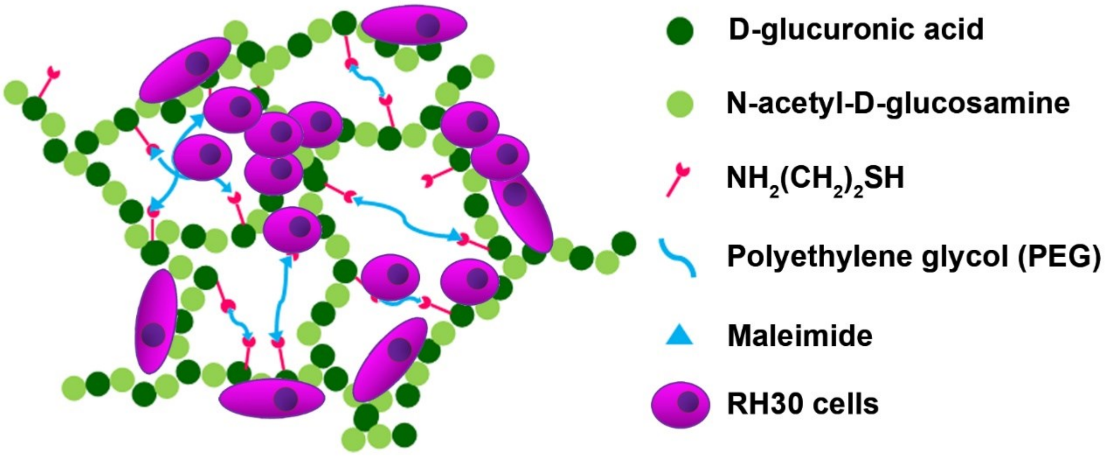

Figure 2.2: *Graphic representation of hyaluronic acid/PEG hydrogel with seeded cells.*

Table 2.1: Antibody list

Target Protein	Producer	Product Code	Host	Application
CD29	BioLegend	303004	Mouse	Flow Cyt
CD44	Invitrogen	11-0441-82	Rat	Flow Cyt
CD56	BD Pharmingen	5555516	Mouse	Flow Cyt
CD105	Beckman Coulter	PN A07414	Mouse	Flow Cyt
CXCR4	Beckman Coulter	PN A07409	Mouse	Flow Cyt
ITGA5	R&D Systems	FAB1864P	Mouse	Flow Cyt
MYOD	SantaCruz Biotechnology	sc-377460	Mouse	IF
HuNu	Millipore	MAB1281	Mouse	IF
LAM	Sigma	L0663	Rat	IF
COL1α1	Invitrogen	PA5-35379	Rabbit	IF
FN	Invitrogen	MA5-11981	Mouse	IF
Ki67	Abcam	ab 15580	Rabbit	IF
ITGA5	R&D Systems	MAB1864	Mouse	IF
VIM	Abcam	ab20346	Mouse	IF/ WB
ITGA5	SantaCruz Biotechnology	sc-376199	Mouse	WB
Lam A/C	Leica Biosystems	NCL-LAM-A/C	Mouse	WB
GAPDH	R&D Systems	NB300-221	Mouse	WB
αMo-488 Alexa Fluor	Invitrogen	A-11001	Goat	II° Ab / IF
αMo-594 Alexa Fluor	Invitrogen	A-11005	Goat	II° Ab / IF
αRb-488 Alexa Fluor	Invitrogen	A-21441	Chicken	II° Ab / IF
αRb-594 Alexa Fluor	Invitrogen	A-21442	Chicken	II° Ab / IF
αRat-488 Alexa Fluor	Invitrogen	A-11006	Goat	II° Ab / IF
αMo-HRP conjugated	Invitrogen	A16066	Goat	II° Ab / WB

Flow Cyt: *Flow cytometry;* ***IF:*** *Immunofluorescence;* ***WB:*** *Western blot*

Table 2.2: Primer list

Gene Symbol	Producer	Product Code	Temp. annealing (°C)
ITGB1	IDT	Hs.PT.58.39883300	60
ITGB2	IDT	Hs.PT.58.4982621	60
ITGB3	IDT	Hs.PT.58.24825754	60
ITGA1	IDT	Hs.PT.58.45528176	60
ITGA5	IDT	Hs.PT.58.4796384	60
ITGAV	IDT	Hs.PT.58.38998102	60
ITGA6	IDT	Hs.PT.58.453862	60
MET	IDT	Hs.PT.58.339430	60
CXCR4	IDT	Hs.PT.58.22298491	60

Results

Bioinformatic analysis of patient gene expression profile

Unsupervised cluster analysis on GSE108022 identified the most differentially expressed genes between ARMS and ERMS, that are correlated with $\alpha5$ or $\beta1$ integrins. We produced 3 lists with the top 50, 100 and 150 most differentially expressed genes. For further analysis, only the list with 100 genes was considered since it offered an optimal balance between false discovery rate and a good number of genes for clusters identification. The list was then compared with the Matrisome database[48] to identify genes related to structural ECM: 15 genes were identified as structural components of the ECM (highlighted in yellow in Figure 3.1).

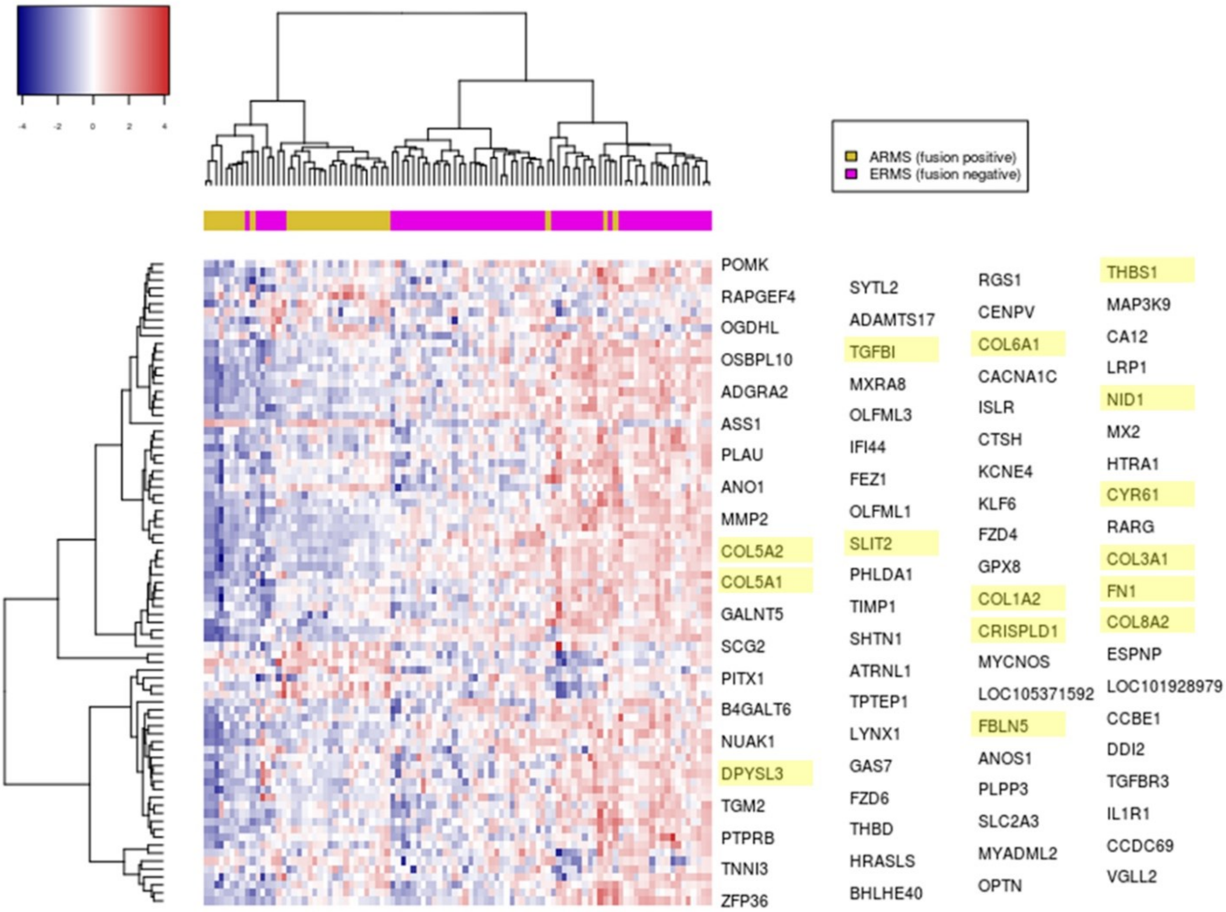

Figure 3.1: *Heat-map from the clustering of top 100 differentially expressed genes between ARMS (ochre) and ERMS (magenta). Compared to healthy control group, overexpressed genes are displayed in red, underexpressed genes in blue; on the right the highlighted genes are shared with the genes in the Matrisome database.*

Pathway enrichment analysis, calculated with EGAN on KEGG Pathways, displayed that the identified gene list was enriched in pathways of "ECM-receptor interaction" and "focal adhesion" with an FDR (false discovery rate) of 6,07e-13 and 6,07e-10 respectively. On Pathway Interactions Database (National Cancer Institute) the most recalled pathways are: "Beta1 integrin cell surface interactions"

(FDR 3,63e-16), “Beta3 integrin cell surface interactions” (FDR 2,21e-10), “Beta5 beta6 beta7 and beta8 integrin cell surface interactions” (FDR 3,02e-7) and “Integrins in angiogenesis” (FDR 3,43e-7) (Figure 3.2).

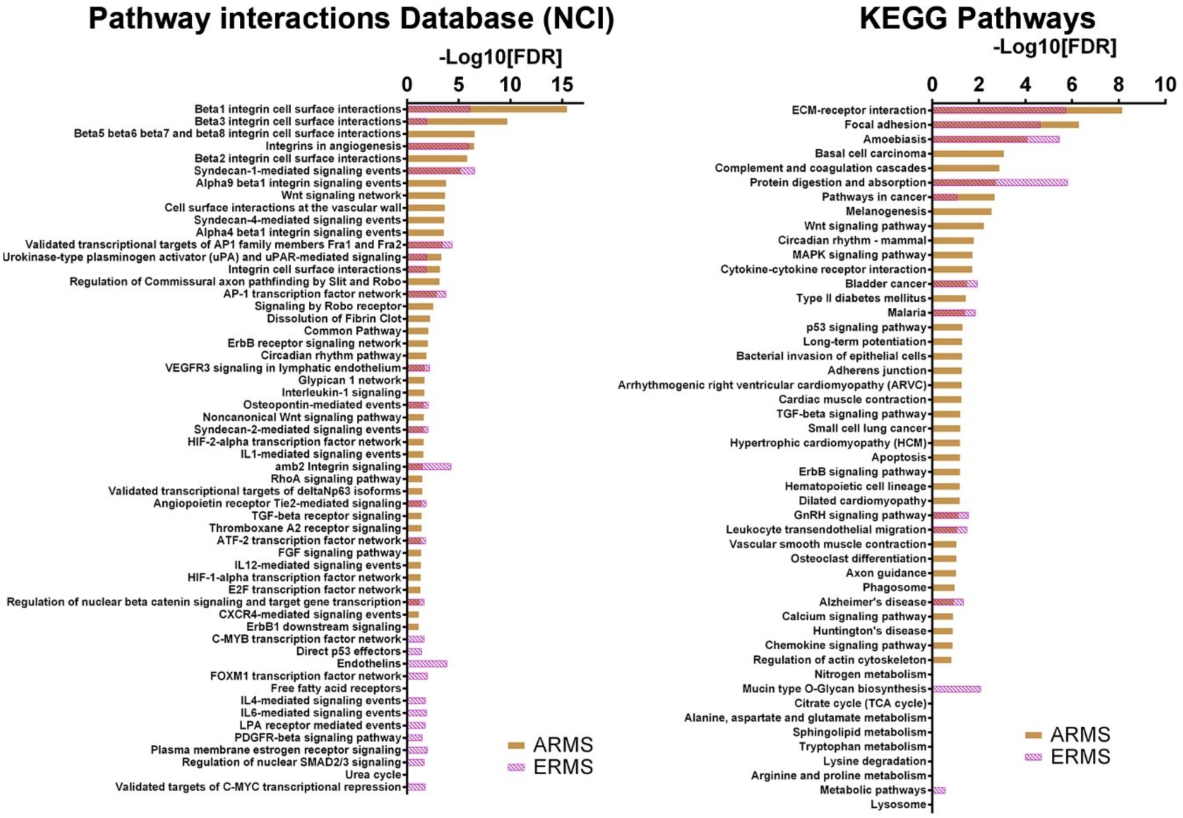

Figure 3.2: *Enrichment analysis of the top 100 integrin α5 or β1 related genes differentially expressed between ARMS (solid ochre bars) and ERMS (dashed magenta bars). Analysis was conducted on Pathway Interaction Database (NCI) and on KEGG Pathways.*

The 15 genes related to ECM (“ECM list”) were used to cluster ARMS and ERMS patients, according to their differential expression, in other public available datasets. We first tested the ECM list on the dataset of origin (GSE108022), showing that ECM related genes alone were still able to separate patients in the ARMS and ERMS subgroups. We then tested the “ECM list” on other public available datasets GSE28511 and GSE66533 (Figure 3.3). We here showed that the ECM subset of genes was able to discriminate patients with ARMS from patients with ERMS in accordance with the differential expression of those genes in the two pathologies.

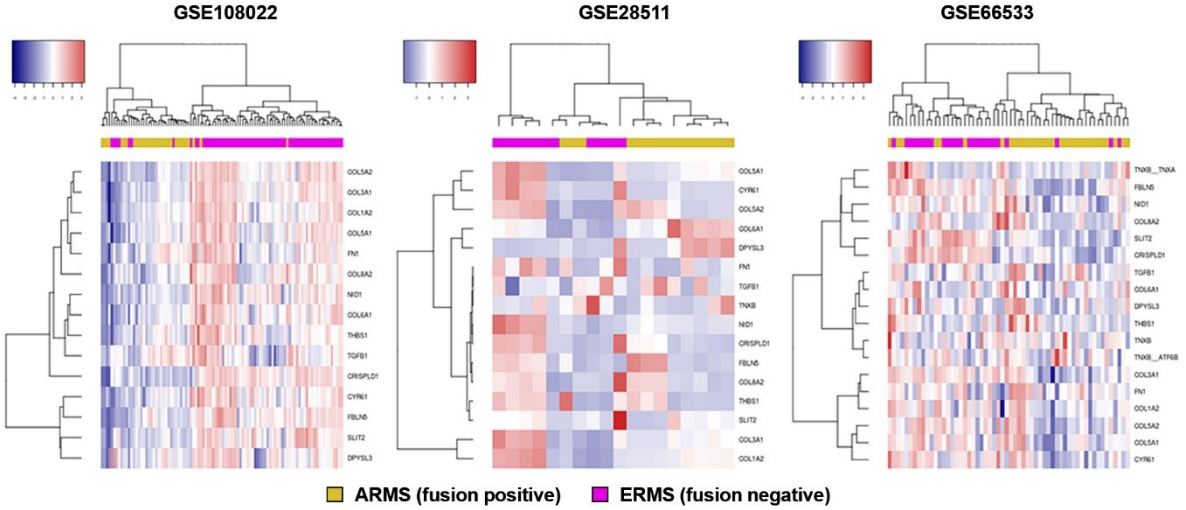

Figure 3.3: *Heat-maps displaying the clustering of "ECM list" of genes between ARMS (ochre) and ERMS (magenta) on 3 different datasets (GSE108022, GSE28511, GSE66533). Compared to healthy control group, overexpressed genes are displayed in red, underexpressed genes in blue.*

These results, taken together, suggest that genes related to integrins $\alpha5$ and integrin $\beta1$ are differentially regulated between ARMS and ERMS. In particular, the gene expression profile of a restricted class of genes, related to ECM, is still able to discern ARMS and ERMS patients, indicating a differential regulation of ECM genes in the two RMS microenvironments.

Xenograft production & characterization

Due to the lack of human specimens and the rarity of the disease, we used a xenograft model as source of tumor masses. Before the *in vivo* injection, the ARMS cell line RH30 was characterized by immunofluorescence (IF) and flow-cytometry for the expression of mesenchymal and RMS specific markers, as MyoD, vimentin, CD56, CD105 and CXCR4 (Figure 3.4A and B). After confirming the ARMS profile of the cell line, cells were used to produce xenografts by injection in immunodeficient mice (Rag2$^{-/-}$ γc$^{-/-}$).

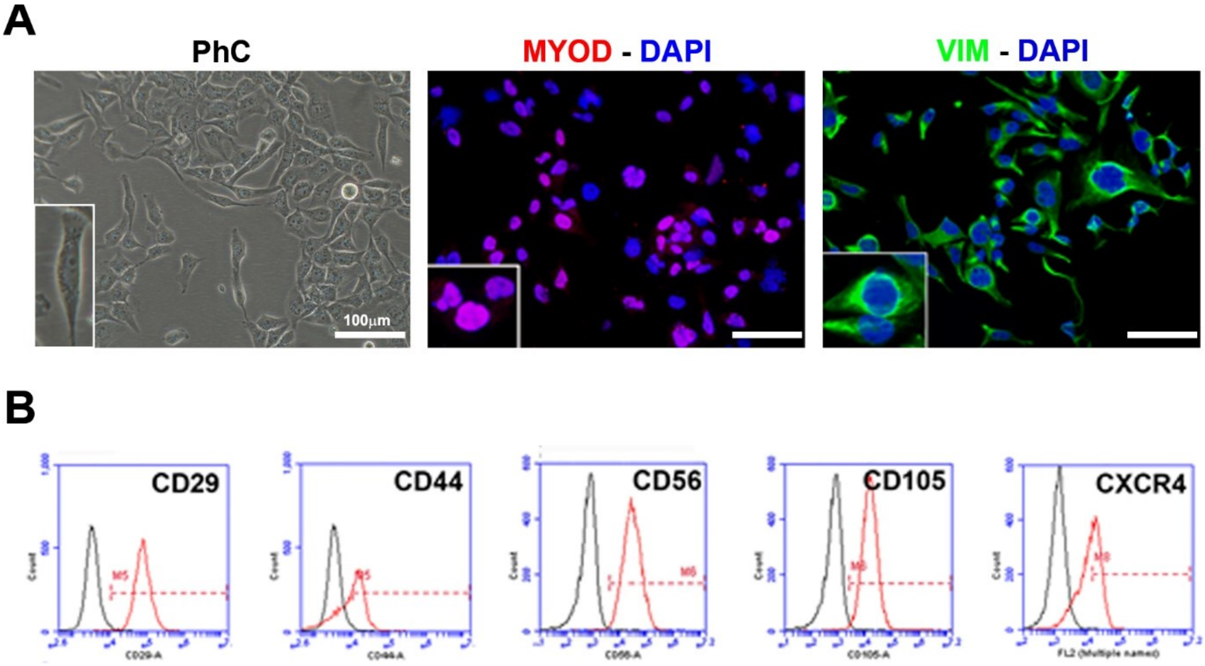

Figure 3.4: *Characterization of RH30 ARMS cell line:* ***A.*** *Phase contrast image showing characteristic spindle shape-morphology, immunofluorescence showing cell positivity for myogenic (MyoD) and mesenchymal (vimentin) markers.* ***B.*** *Flow cytometry displaying the expression of stromal mesenchymal markers CD29 and CD44, muscular marker CD65 and pathology related markers CD105 and CXCR4.*

Three weeks after RH30 cells injection in Rag2$^{-/-}$ γc$^{-/-}$ mice, the obtained xenografts were also characterized to ensure similarity with the human ARMS. H&E staining was compared to ARMS histology present in literature showing high grade of overall similarity, confirmed by a pathologist (Dott.ssa Luisa Santoro, Azienda Ospedaliera di Padova)(Figure 3.5A). MyoD expression was evaluated for the identification of cells committed to muscle lineage, Human Nuclei (HuNu) was used to determine the presence of mouse infiltrating cells in the tumor mass (Figure 3.5B).

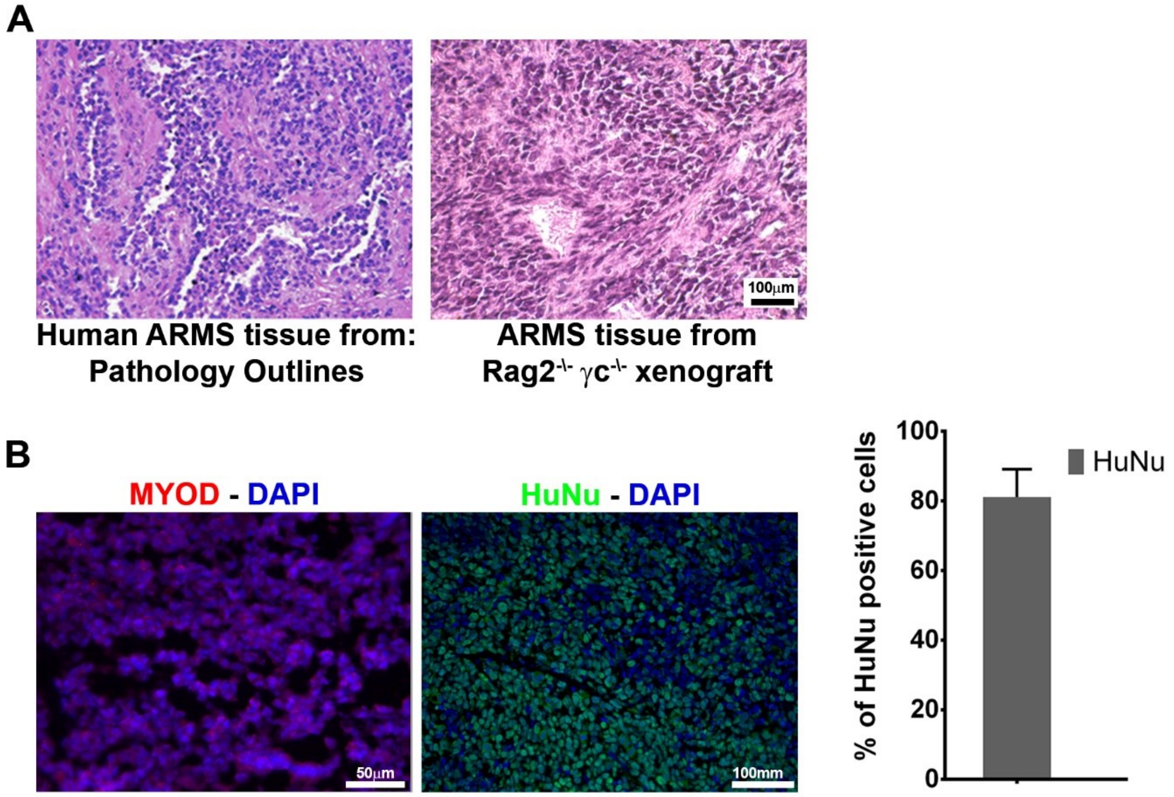

Figure 3.5: *Characterization of ARMS xenografts:* ***A.*** *Haematoxylin and Eosin (H&E) staining of human ARMS tissue and xenograft produced in mice by RH30 injection;* ***B.*** *Immunofluorescence staining for MyoD and HuNu expression in ARMS xenograft, HuNu positive cells were about 80% per field.*

Considering the tissue architecture, MyoD positivity, myogenic and RMS-specific marker, we assume a good similarity between human ARMS and xenografts. HuNu staining shows that most of the cells in the tumor mass are from human origin (81,2%). We then concluded that the produced xenograft recapitulates the feature of human ARMS tissue.

Direct use of dECM as scaffold for 3D culture:

Conservative approach:

In the conservative approach, the experimental strategy (Figure 3.6A) considered the decellularization of the xenografts for the direct use of the dECM as a scaffold for 3D cell culture. The experimental procedure designed to reach this goal developed the following steps: i) optimization of a decellularization protocol that balances the removal of cellular components and retains architecture and molecular composition of the tissue; ii) characterization of the dECM in terms of ECM protein content; iii) identification of the optimal recellularization strategy for reconstructing an homogeneous 3D tissue; iv) analysis of integrin expression profile and cell migration (Figure 3.6B).

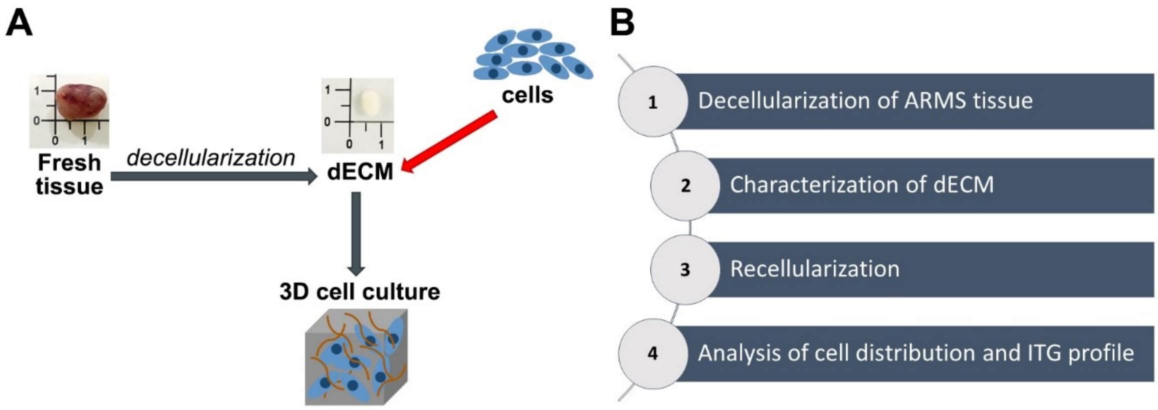

Figure 3.6: *Schematic representation of the conservative approach strategy:* ***A.*** *Graphic representation of the experimental strategy from fresh tissue to decellularized ECM and finally 3D cell culture.* ***B.*** *Experimental procedure steps.*

ARMS decellularization and characterization

The decellularization protocol has been optimized starting from a previous detergent enzymatic treatment used for the decellularization of mouse skeletal muscles, developed in our lab [41].However, using this protocol, the DNA content was much higher than the limit set for a good decellularization (>95% of DNA depletion compared to fresh tissue). The double substitution of SDC and water with SDS and Triton x-100 respectively, led to an optimal decellularization of the xenograft (Figure 3.7A and B). DNA depletion was confirmed by Nanodrop quantification (-97% of total DNA content), gel electrophoresis and by IF with the vanishing of DAPI signal (Figure 3.7C and E). Collagen and GAG quantification (Figure 3.7D), together with IF, revealed the retention of the structural proteins: collagen 1, fibronectin and laminin. Tissue architecture was preserved as shown by H&E staining (Figure 3.7E).

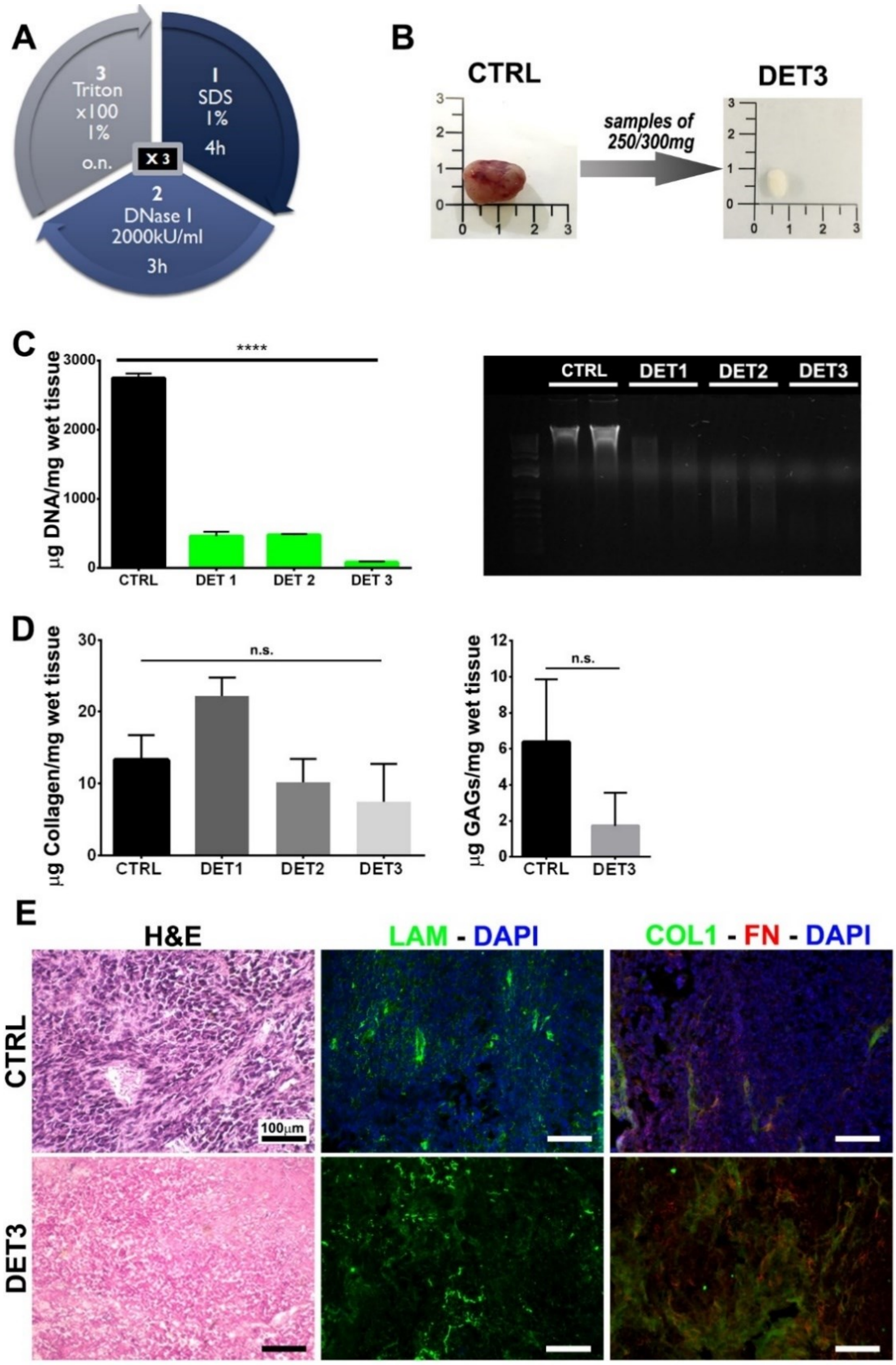

Figure 3.7: *ARMS xenograft decellularization and characterization:* ***A:*** *Schematic representation of detergent-enzymatic decellularization protocol;* ***B:*** *Macroscopic appearance of ARMS tissue before and after decellularization;* ***C.*** *DNA quantification with NanoDrop and fragmentation assessed by gel electrophoresis;* ***D.*** *Collagen and GAG quantifications;* ***E.*** *H&E staining and IF of fresh and decellularized ARMS xenografts.*

The attained matrices proved to be efficiently decellularized with strong reduction of DNA content and retention of ECM proteins. We thus proceeded to set a recellularization procedure for this scaffold.

Recellularization with microinjection

First attempts of recellularization were conducted seeding cells on top of the dECM or by injecting them with an insulin syringe inside the dECM. Superficial seeding resulted in cell distribution only on external surface of the support. Insulin syringes, conversely, did not allow precise and multiple injections. Cell viability in both cases was minimal (data not shown). The use of a microinjector combined with a stereomicroscope allowed multiple injections with a control of the injected volume in the order of the picolitres (Figure 3.8A). Conditioning of the matrices overnight in culture medium supplemented with 20% FBS considerably improves cell viability (Figure 3.8B). Recellularization with RH30 GFP$^+$ made possible to follow macroscopically the spreading, the over time, of cells inside the scaffold. However, cells remained confined in the sites of injection (Figure 3.8E and C). In addition, actively proliferating cells, stained with Ki67, decreased drastically between 4 and 7 days, from 69% to 24% respectively (Figure 3.8D).

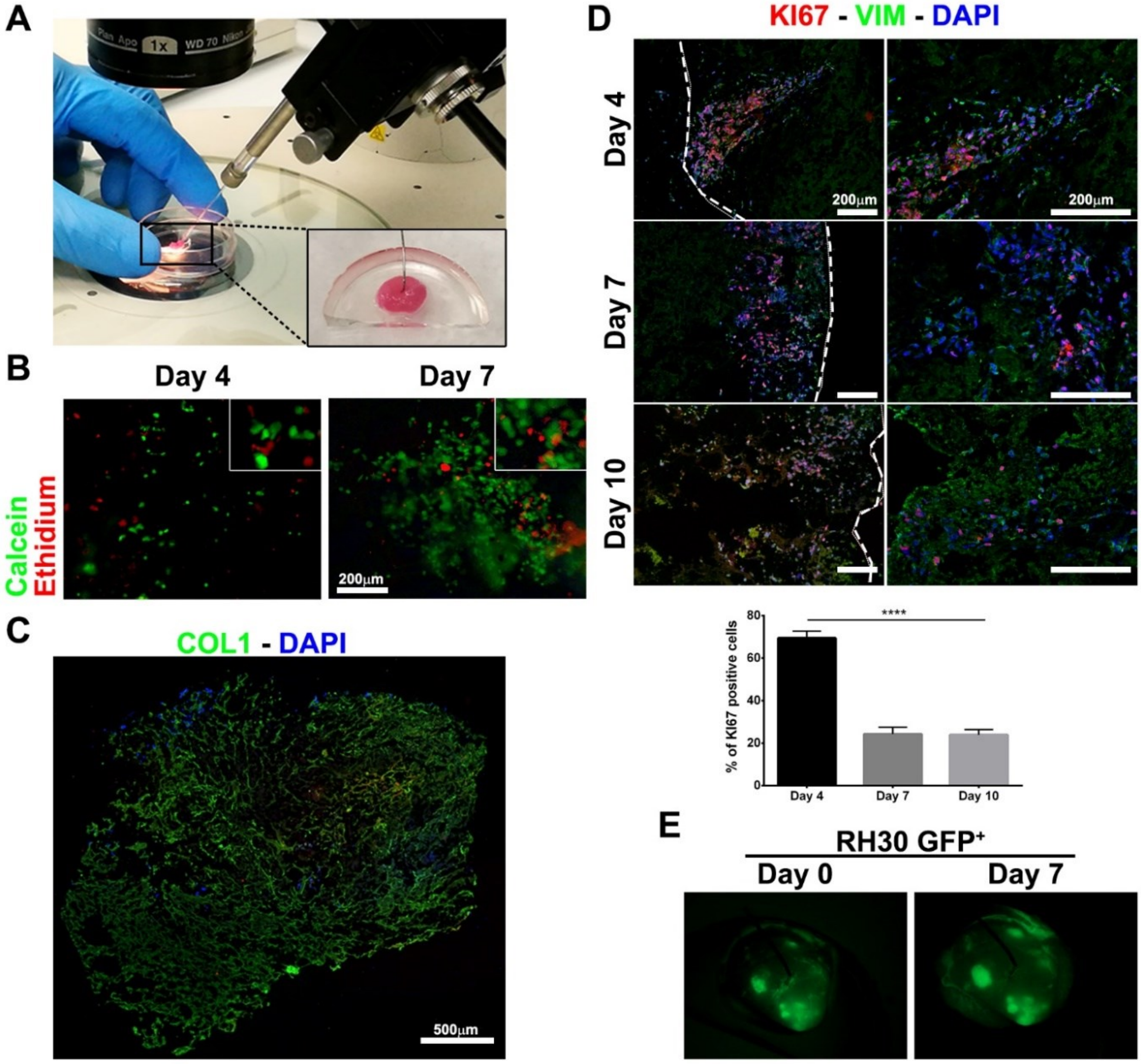

Figure 3.8: *ARMS dECM recellularization with microinjector:* ***A.*** *Microinjector seeding RH30 cell suspension, in the close-up is showed how ARMS dECM is fixed to a PDMS support;* ***B.*** *Live&Dead assay on RH30 cells 4 and 7 days after seeding, calcein (in green) stained alive cells, ethidium (in red) marked apoptotic cells;* ***C.*** *IF staining of recellularized dECM cross-section;* ***D.*** *IF staining of cells injected in dECM at 4, 7 and 10 days, Ki67 positivity marks active proliferating cells, percentages of proliferating cells per field at the three intervals are represented in the histogram below;* ***E.*** *IF image of the whole dECM seeded with GFP+ RH30 cells displays distribution of cells restricted to site of injections.*

The results obtained with cell microinjection technique were not completely satisfactory in terms of cell distribution and viability at long timepoints. We evaluated the possibility to perfuse cells through the whole matrix to obtain a homogeneous cell distribution and perfusion of fresh culture medium to improve nutrient diffusion and waste removal. To this end, the dynamic perfusion bioreactor U-Cup was employed.

Recellularization with U-Cup perfusion bioreactor

U-Cup bioreactor allows dynamic seeding and culture of 3D scaffolds (Figure 3.9A). After optimization of perfusion parameters, using the commercially available and clinical grade collagen I sponge Ultrafoam (UF), we employed ARMS dECM as scaffold of the 3D culture in the bioreactor. Cell distribution, assed with H&E staining, exhibited cell clustering mainly on the external surfaces of the dECM and not a homogeneous distribution as hypothesized (Figure 3.9B, Standard ECM). Comparing the pores dimension between UF and dECM we saw a significant difference in pore size (Figure 3.9C and D). To increase pores size in the dECM, we performed five freeze and thaw cycles; however, this procedure proved to be ineffective (Figure 3.9C and D). As a consequence, the seeding efficiency (n° of cells engrafted on the scaffold after 24 hours), was unchanged between standard and treated dECMs and about 75% lower compared to UF (Figure 3.9E). No difference can be seen in cell distribution on dECM before and after the freeze and thaw cycles (Figure 3.9B).

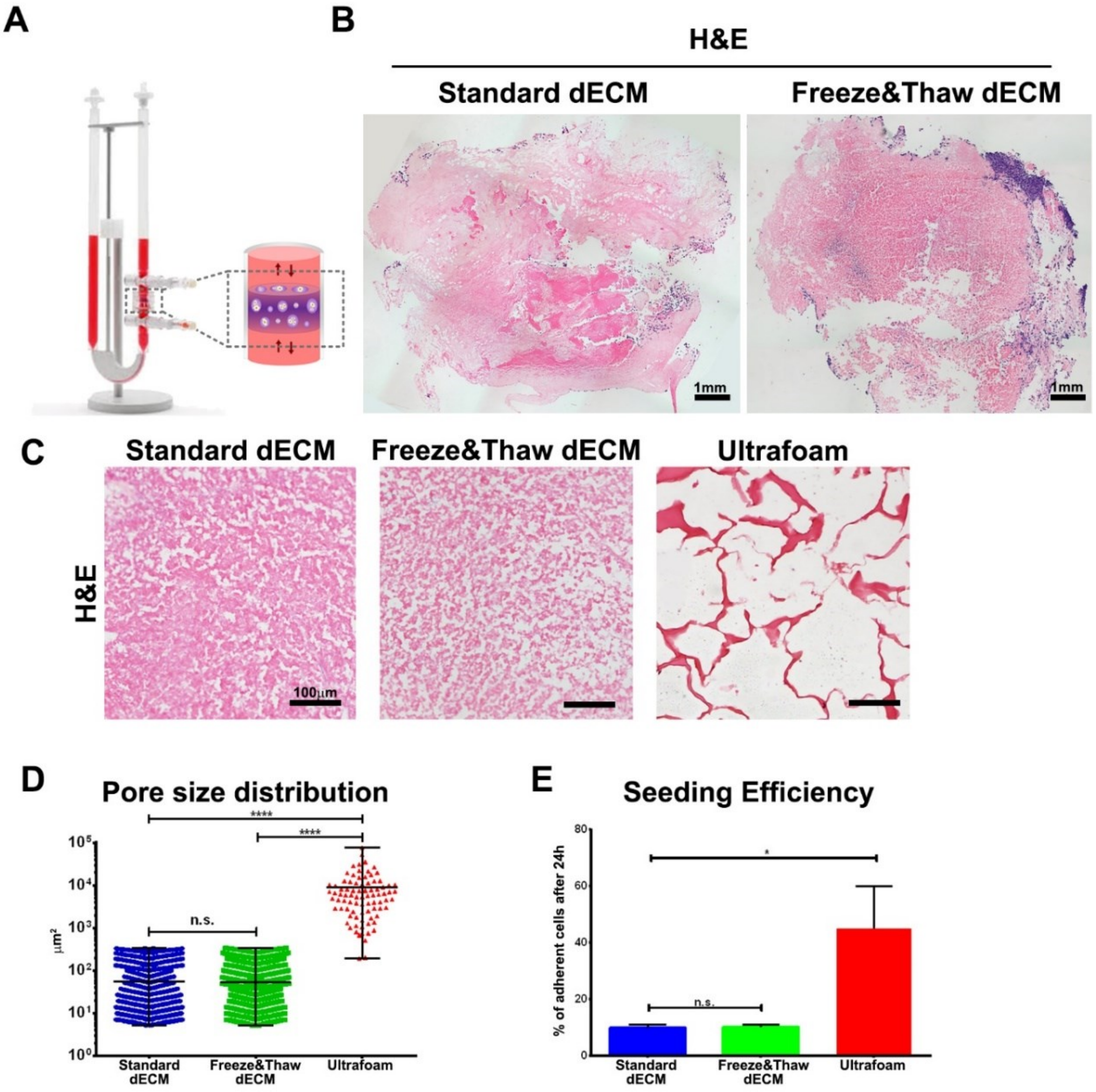

Figure 3.9:A. *Example of the U-Cup bioreactor from Cellec Biotek with enlarged representation of culture chamber;* ***B.*** *H&E staining of dECM recellularized with the bioreactor, on the left standard dECM on the right dECM treated with freeze & thaw cycles;* ***C.*** *H&E staining showing the difference in porosity between standard dECM, dECM after freeze and thaw cycles and Ultrafoam collagen I sponge;* ***D.*** *Pores dimension in standard dECM, dECM after freeze and thaw cycles and Ultrafoam collagen I sponge;* ***E.*** *Seeding efficiency in standard dECM, dECM after freeze and thaw cycles and Ultrafoam collagen I sponge;*

Taken together, these results demonstrated that the direct use of ARMS dECM for perfusion is not feasible. Freeze and thaw cycles were not sufficient to enlarge pores or improve seeding efficiency. An alternative approach for the development of the 3D model was evaluated.

Analysis of dECM composition for synthetic scaffold enrichment:

Deconstructive approach:

As demonstrated by the previous results, the conservative approach failed in the recellularization step. To overcome this issue, we decided to sacrifice the tissue architecture, enclosed in the dECM, in favour of a precise knowledge of its protein composition. Gaining this information, we developed the idea to include in a synthetic scaffold the most representative proteins of the ARMS tumor microenvironment (Figure 3.10A). The deconstructive approach considers: i) harsh decellularization of ARMS fresh tissue; ii) High Resolution Mass Spectroscopy(HR-MS) analysis of the ECM; iii) inclusion of ARMS cells in a 3D scaffold enriched with selected proteins and iv) analysis of integrin expression profile and cell migration (Figure 3.10B).

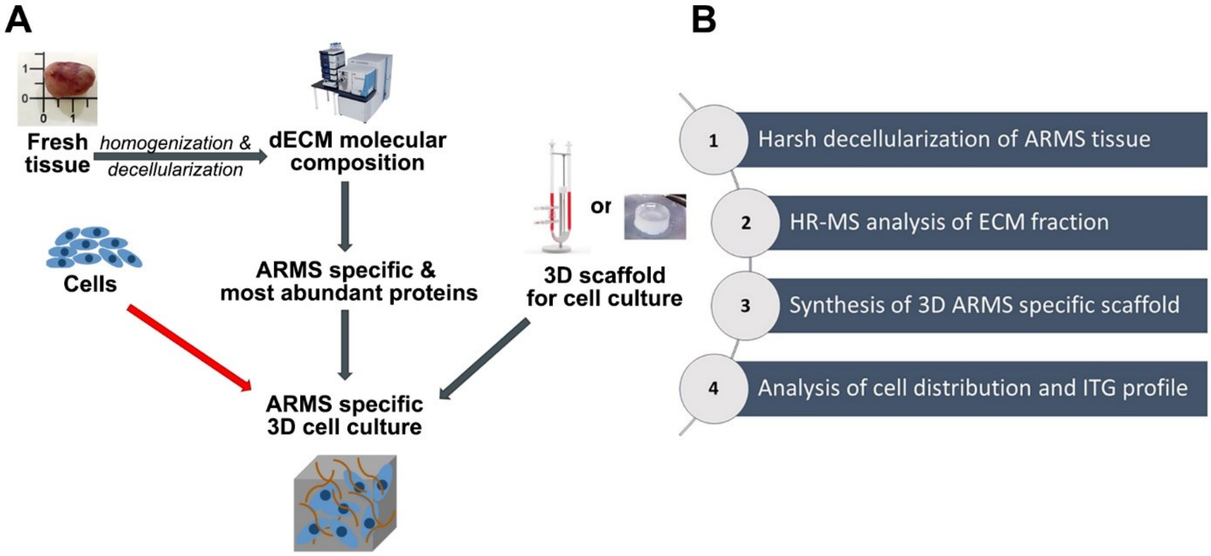

Figure 3.10: *Schematic representation of the deconstructive approach strategy:* ***A.*** *Graphic representation of the experimental strategy from fresh tissue to identification of most representative ECM proteins in ARMS and inclusion in 3D scaffold for cell culture;* ***B.*** *Experimental procedure steps.*

Decellularization protocol for ECM fraction enrichment from fresh tissue.

The decellularization of the fresh tissue was performed following the protocol published by Prof. Alexandra Naba [106]. This protocol shifts the balance between preservation of ECM structure and clearance of cellular components in favour of the latter. The procedure allowed the recovery of 5 protein fractions: cytosolic, nuclear, membrane associated, cytoskeletal and finally the insoluble pellet enriched in ECM proteins (Figure 3.11A). To confirm the purity of each fraction the presence of a reference protein for each fraction was verified by western blot (Figure 3.11B). For cytosolic fraction we used GAPDH as reference: the presence of GAPDH is higher in the cytosolic fraction with some residual in nuclear fraction, more importantly, almost no traces of GAPDH were reported in other fractions. Laminin A/C was the reference for the nuclear fraction and was found only in the first fraction (probably due to the lysis of nuclear membranes) and the second fractions. ITGA5 was used as reference for membrane associate proteins; besides the presence in the first fraction, the detection was restricted to the membrane associated fraction with a weak residual signal in the cytoskeletal fraction, probably due to the fact that integrins are associated with actin cytoskeleton. Finally, vimentin was used to determine contamination from the cytoskeletal fraction. In this case we had to overexpose the acquisition at the UVITEC Alliance chemiluminescence imaging system resulting in low signal/noise ratio, the specific vimentin band was not detected in all of the 4 fractions, this could be due to unsuccessful staining.

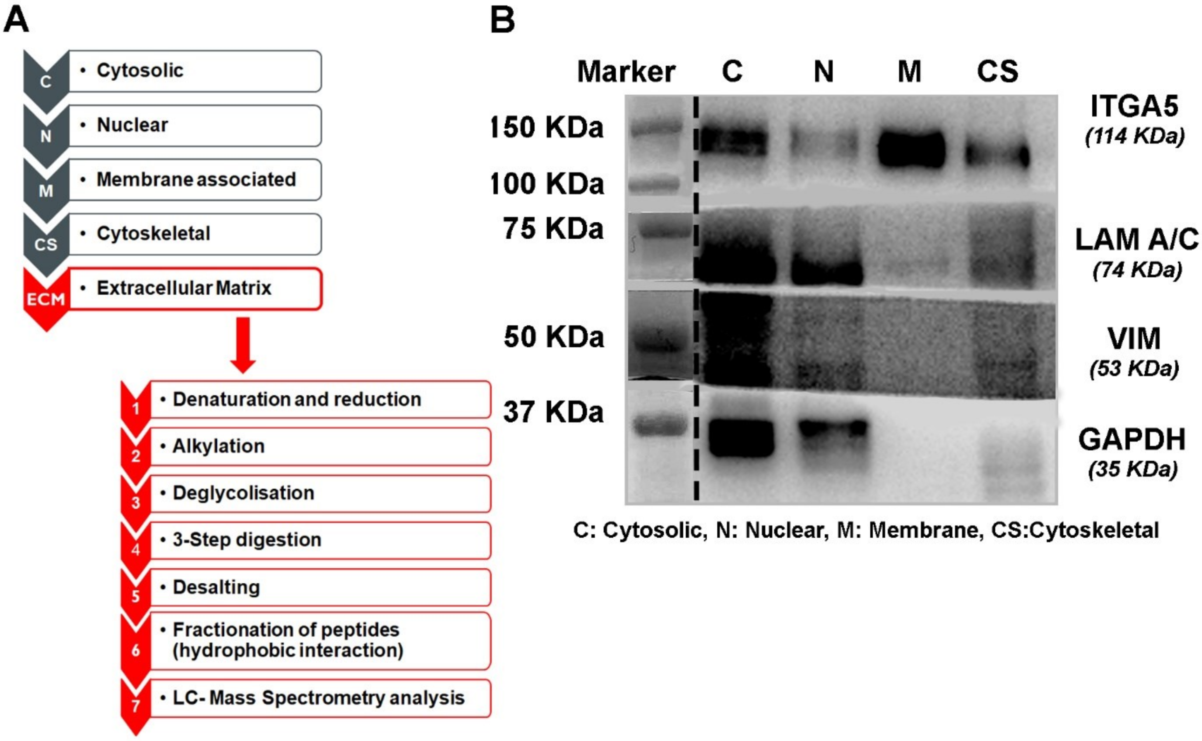

Figure 3.11: *Decellularization and fractionation of ARMS fresh tissue from Naba protocol:* ***A.*** *Schematic representation of the procedure for MS analysis of ECM enriched fraction;* ***B.*** *Western Blot of tissue fractions: cytosolic (C), nuclear (N), membrane associated proteins (M) and cytoskeletal (CS).*

Proteomic analysis of ECM enriched fraction

Proteomic analysis produced a list of 555 proteins present in ARMS xenografts. Since in the xenograft we expected contribution in ECM deposition both from murine stromal and human ARMS cells, proteins from both origin were considered in the analysis. The list of identified proteins was compared with the "the Matrisome project" dataset of ECM proteins developed by Prof. Naba and colleagues (http://matrisomeproject.mit.edu/) to classify ARMS ECM proteins. These were divided in structural ECM proteins, referred as Core ECM proteins, or proteins interacting with the ECM without a structural function, as growth factors or secreted proteases, referred as ECM-Associated proteins. This classification was done separately for mouse and human proteins. In terms of number of proteins detected, most of mouse proteins were relative to ECM (48/62), whereas human ECM proteins were less represented (68/493) and most of the proteins, indicated as "Others", were cytoplasmatic (probably residues of the decellularization procedure) (Figure 3.12, Number of Proteins). Peptide precursor ion abundance (Peptide Abundance) and number of peptides were used as indicators of relative abundance of the ECM proteins. Considering human and mouse together, these two indicators were about 39% and 86% respectively. This indicated that our samples were enriched in ECM proteins (Figure 3.12).

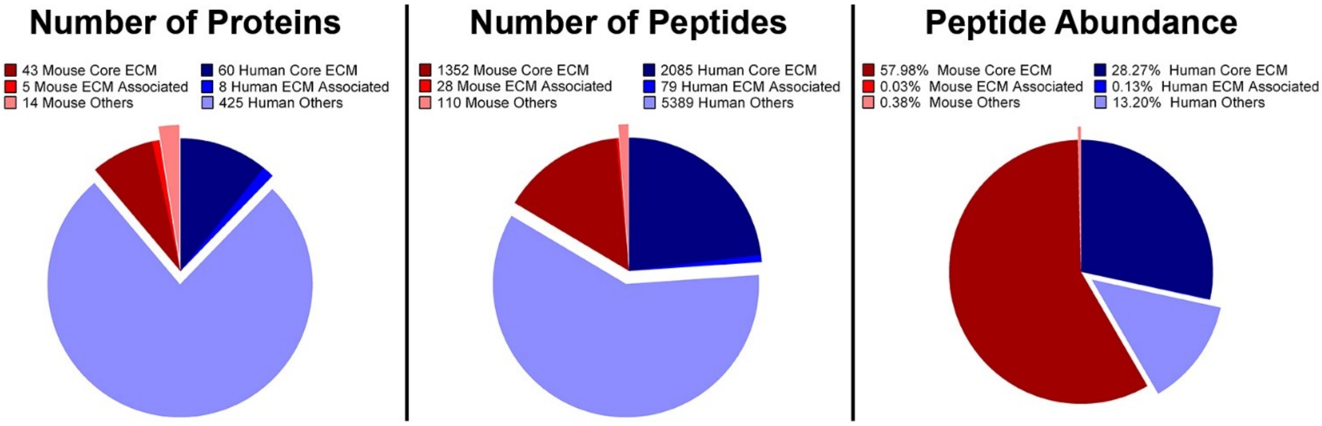

Figure 3.12: *Pie-charts showing from left to right: overall number, number of peptides and the peptide abundance of human (shades of blue) and murine (shades of red) Core ECM proteins, ECM associated proteins and ECM unrelated proteins.*

We then considered the number of peptides and peptide abundance for each protein of the 3 main categories of ECM structural proteins – "Collagens", "Glycoproteins" and "Proteoglycans" – to identify the most abundant in ARMS ECM. We excluded proteins identified with less than 10 peptides to reduce the false discovery rate. Highest signals of protein abundance were form collagens and among them the most represented were: COL1, COL4 and COL3. Considering the number of peptides, collagens producing higher number of peptides are COL6, COL12 and COL1. Glycoproteins had, in general, a lower Peptide Abundance compared to collagens, however the most represented were FBN, POSTN and FN. Number of peptides was higher for FBN, FN, LAMA2, LAMB2, LAMC1 and POSTN. Finally, the contribution of proteoglycans seems negligible for the protein abundance even if HSPG2 was well represented by more than 150 peptides (Figure 3.13).

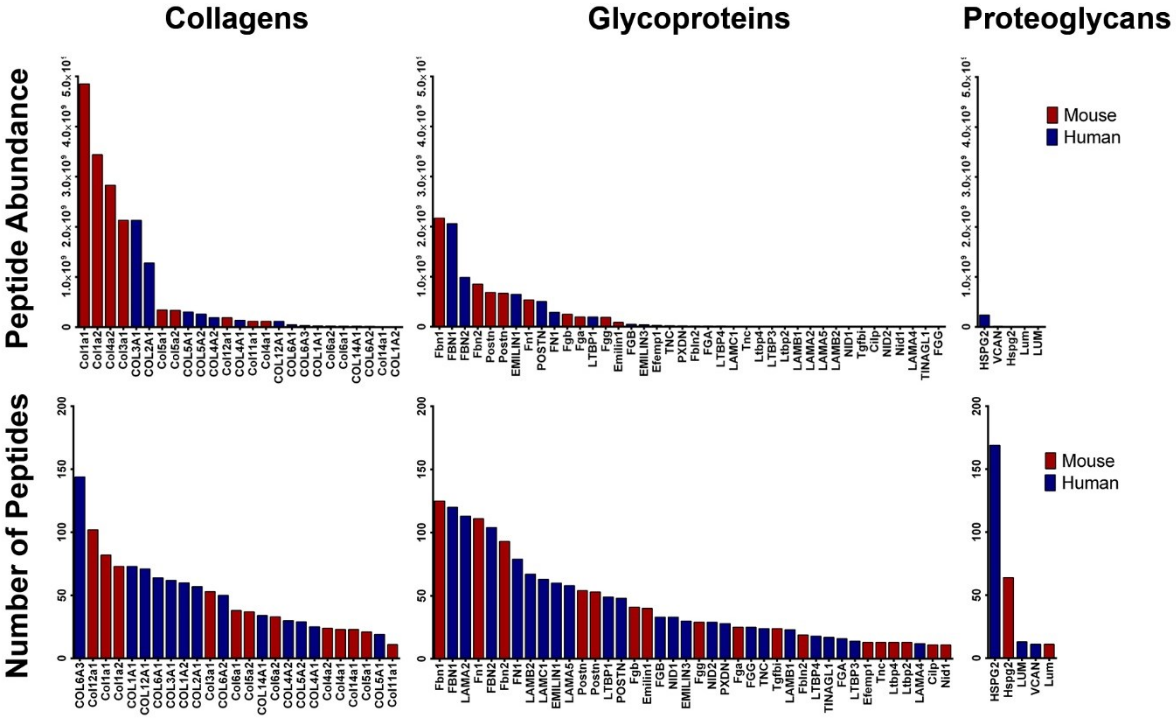

Figure 3.13: *Peptide abundance and number of peptides of single ECM proteins. Proteins were divided in 3 classes: collagens, glycoproteins and proteoglycans.*

In conclusion, combining peptide abundance and number of peptides, we could conclude that, from our analysis, ARMS ECM resulted rich in collagens and poor in proteoglycans. The structural ECM proteins that displayed higher peptide abundance and were more represented by number of peptides were COL1, FBN, FN and POSTN. These proteins will be considered for inclusion in a 3D scaffold.

Ultrafoam perfusion 3D culture

Firsts experiments for recellularization with U-Cup bioreactor were performed using Ultrafoam, without any additional ARMS ECM specific protein, to determine cell distribution upon perfusion. Cells at 4 days were well distributed inside the scaffold but dispersed at single cell level with an overall low density. At 7 days cells were concentrated mainly on the upper side of the scaffold forming a tissue-like structure with high cellularity. At 15 days cells were still growing on the external surface with some improvement in the recellularization of the inner part (Figure 3.14A). We selected for further experiments the condition at 7 days for the good surface cellularity and enhanced interaction between cell and ECM rather than cell-cell interactions, as reported for later timepoints. The percentage of proliferating cells evaluated with KI67 staining at 7days was about 41% of the total cells (Figure 3.14B). We than performed gene expression for integrin profile and we reported a significant upregulation of ITGA5 and CXCR4 (Figure 3.14C): respectively the fibronectin and SDF-1 receptors, the latter already reported to have a role in metastatic migration of ARMS cells [107]. The presence of active and latent forms of matrix metalloproteases 2 and 9 (MMP-2 and MMP-9), assessed by zymography, showed higher secretion of latent MMP-2 in UF 3D culture compared to 2D. However, the active form is detected only in the supernatant of xenograft derived RH30 (Figure 3.14D). Weak signal from active form of MMP-9 was found only in the supernatant of xenograft derived RH30 and MMP-9, in both latent or active form, was not detected neither in U-Cup bioreactor nor 2D culture.

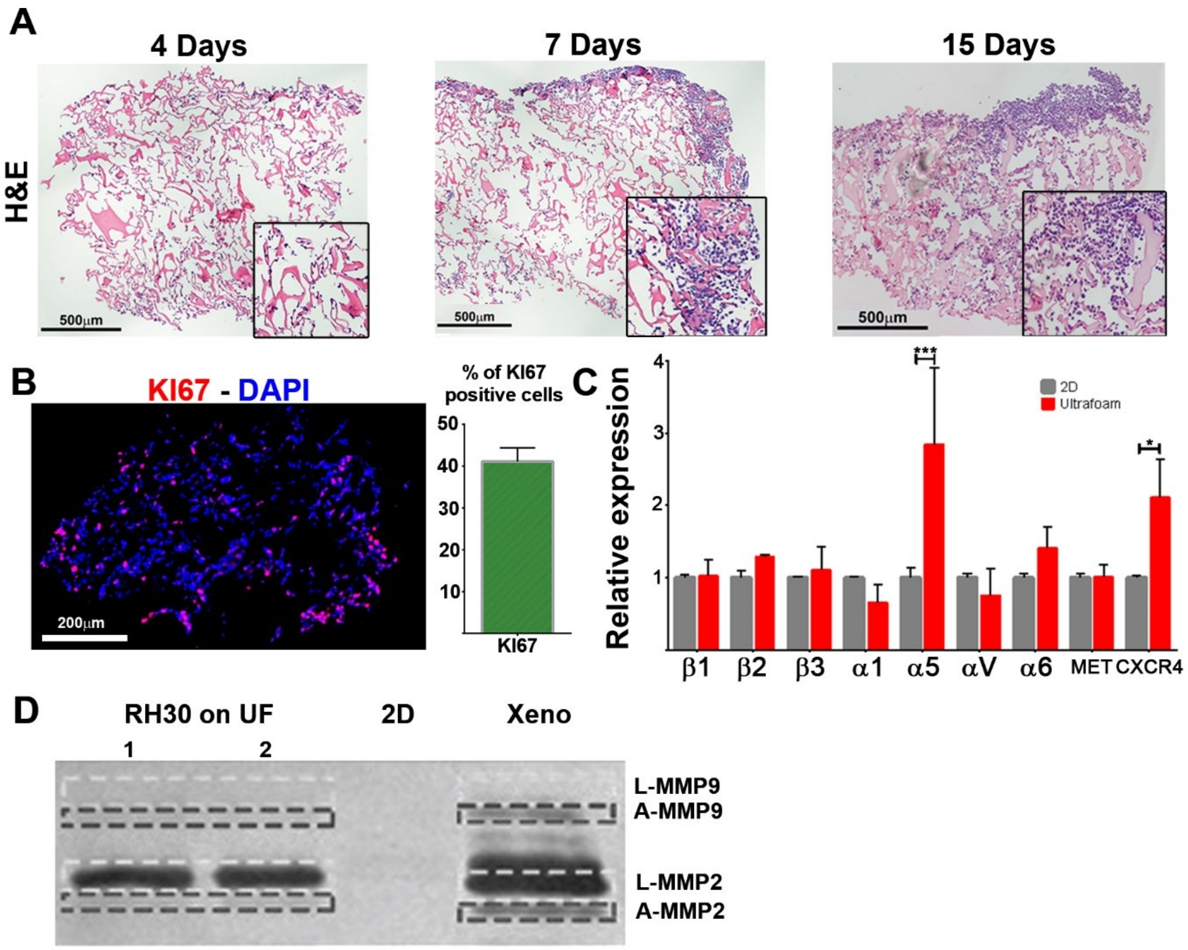

Figure3.14:*ARMS 3D culture on Ultrafoam collagen I sponge in U-Cup bioreactor:* ***A.*** *H&E staining of Ultrafoam scaffold cultured with RH30 cells for 4,7 and 15 days;* ***B.*** *IF staining of RH30 proliferating cells cultured on Ultrafoam scaffold for 7 days;* ***C.*** *Integrin expression profile of RH30 cultured on Ultrafoam for 7 days;* ***D.*** *Zymography of RH30 supernatants isolated from U-Cup bioreactor, 2D culture and cells extracted form ARMS xenograft.*

Culturing RH30 cell in Ultrafoam collagen I sponge improved cell proliferation compared to culture in static condition in dECM (from 24% with microinjection technique to 41% in bioreactor). A tissue-like structure is formed on the surface of the scaffolds at 7 days and gene expression analysis highlighted upregulation of ITGA5 and CXCR4 receptor. Finally, enhanced secretion of MMP-2 in 3D scaffold proved to be more similar to the *in vivo* condition compared to the traditional 2D culture, thus favouring the use of the 3D system for further analysis on cell motility.

Hyaluronic acid hydrogel and enrichment with fibronectin and collagen I

Hyaluronic acid (HA)-based hydrogel was developed to be used as tool for cancer niche recreation. First experiments aimed at assessing the cell distribution in the z dimension and cell viability over time of GFP$^+$ RH30 cells embedded in the HA hydrogel. Viability was assessed following the GFP protein signal by immunofluorescence microscopy. At 4 days, single cell suspension displayed three-dimensional distribution in the first 250 µm of the gel (technical limit of the microscope used). Most of the cells were located in the first 100 µm, proving that cells were actually embedded in a 3D matrix (Figure 3.15A). GFP signal was monitored over the days and cell were reported to be vital up to 10 days. The hydrogel was then enriched with fibronectin, following the indications from the proteomic analysis, and spheroids obtained from RH30 GFP$^+$ cells were cultured in this support to follow spheroid disaggregation and cell migration. In Matrigel, used as control, cells displayed elongated morphology typical of mesenchymal movement invading the surrounding matrix. Spheroids embedded in HA hydrogels displayed sharp margins and cells with spherical morphology, independently from the presence of fibronectin (Figure 3.15B).

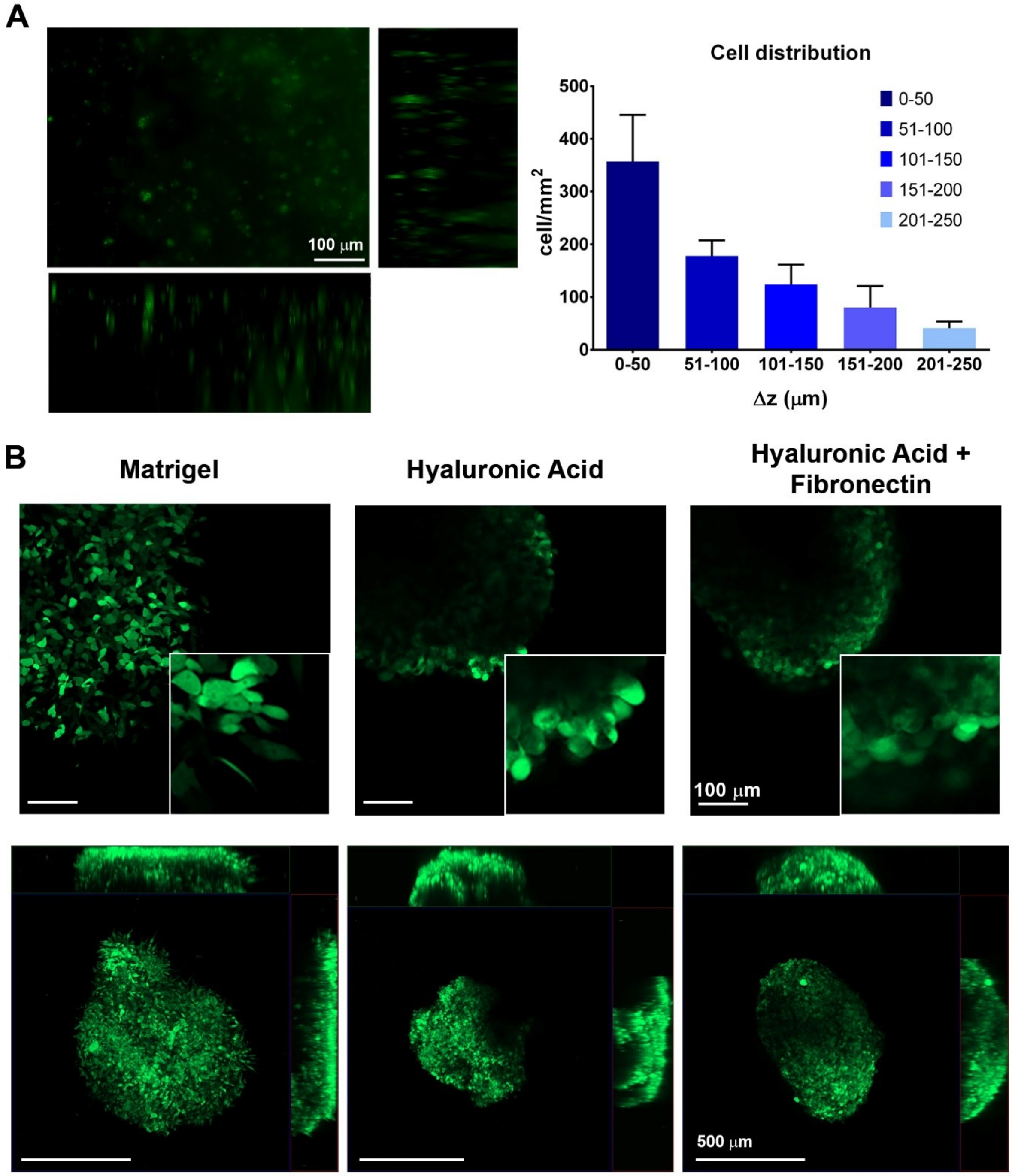

Figure 3.15:*RH30 GFP+ cultured in 3D hyaluronic acid/PEG hydrogels:* ***A.*** *Single cell 3D distribution over 250 µm z-stack with orthogonal projections, histogram displaying number of cells in intervals of 50 µm in z axis;* ***B.*** *Immunofluorescence analysis of spheroid margins in Matrigel (control), hyaluronic acid and hyaluronic acid enriched with 100ng of fibronectin.*

Further efforts have to be made to optimize the concentration and functionalization with other ECM proteins in the system.

RH30 migration of fibronectin and effect of ITGA5 siRNA inhibition

Preliminary results assessed the role of fibronectin in RH30 cell migration. Remarkable difference in cell invasion appeared monitoring over time the cell front of cell cultured on tissue culture petri dishes and petri dishes coated with fibronectin (Figure 3.16A). Quantification of speed and track displacement showed a slight increase in mean cell speed (from 19.4 to 20.8 μm/hour) and a much higher increase in mean distance covered by single cells (from 68 to 126.9 μm) (Figure 3.16B).

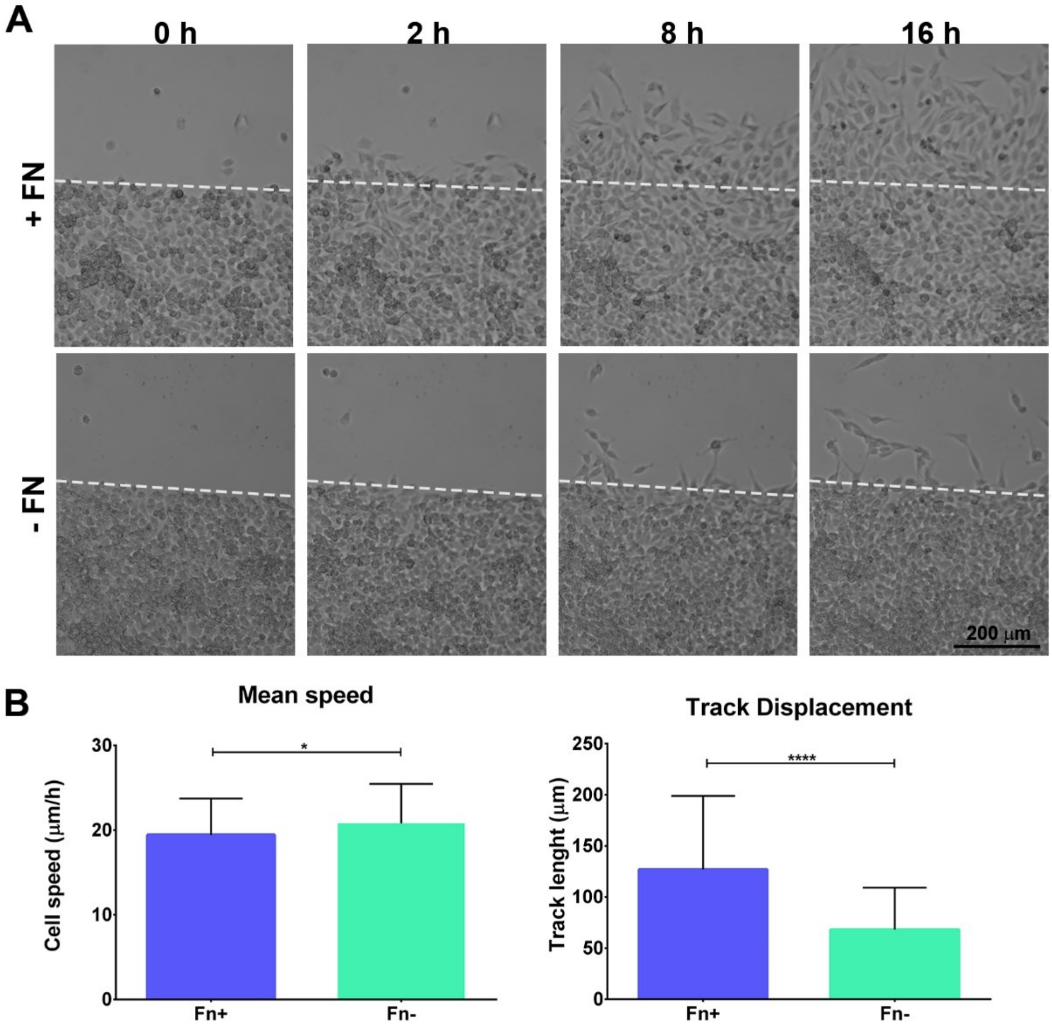

Figure 3.16: *Migration of RH30 cells in presence or absence of fibronectin* ***A.*** *Time lapse images of the invasive front for cells cultured on fibronectin coated petri dish or tissue culture petri dish, timepoints at 0h, 2h, 8h and 16h* ***B.*** *Histograms showing variation in cell migration speed and track displacement of migrating cells in presence or absence of fibronectin coating surface.*

The role of ITGA5 in rhabdomyosarcoma cell migration has been tested, upon siRNA inhibition, with transwell migration and invasion assays. In invasion assays, after 24 hours, none of the two cell populations - siNEG control and treated with siRNA ITGA5 - were able to invade the Matrigel and transmigrate on the other side of the membrane. However, significant difference has been noticed in cell organization. Control RH30 cells displayed a multicellular-strand organization, forming larger interconnected aggregates. ITGA5 silenced RH30 adopt a different organization with higher number of smaller spherical aggregates (Figure 3.17A).

In migration assay was conducted on transwell coated with fibronectin; 43.9% of control RH30 cells were able to migrate on the other side of the membrane whereas only 24.3% of the ITGA5 silenced transmigrated (Figure 3.17B).

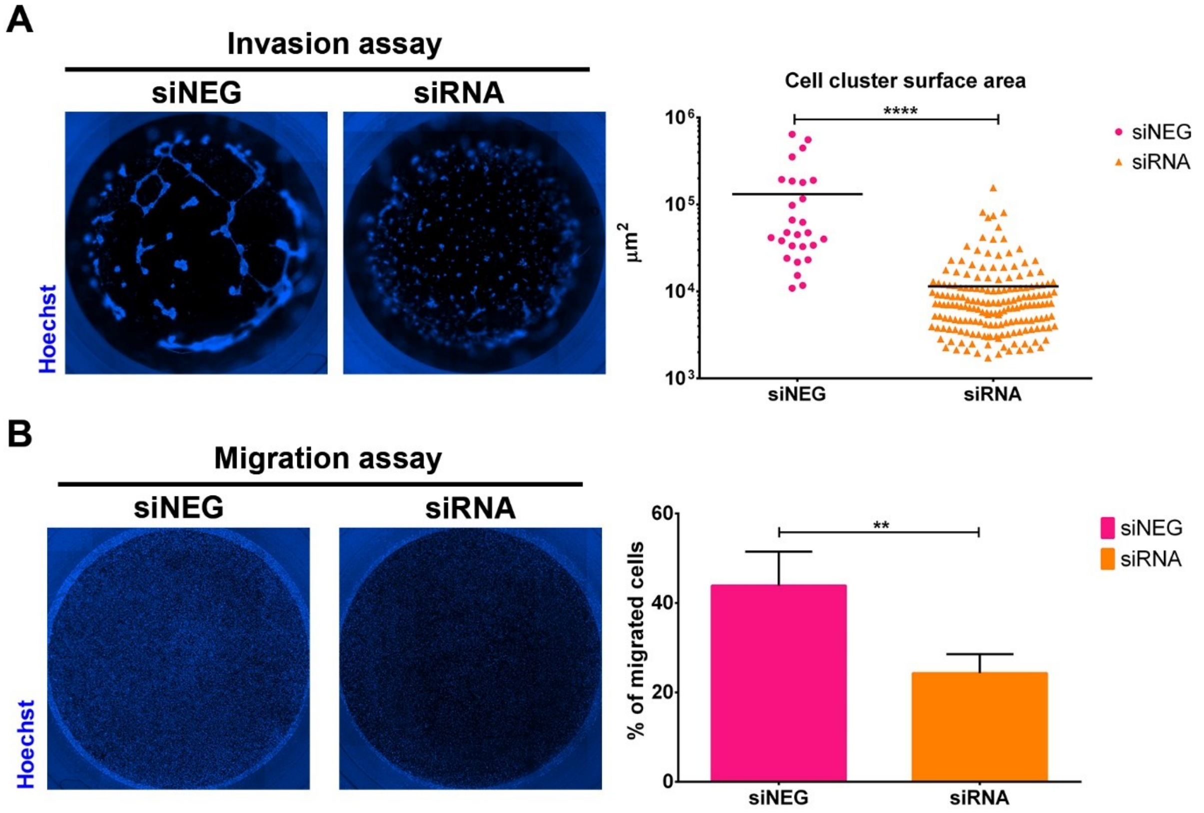

Figure 3.17: ***A.*** *Invasion assay on RH30 cells: IF of total cells in the transwell; Hoechst is used to visualize cell nuclei; dot-plot represents the size of cell aggregates* ***B.*** *Migration assay on RH30 cells: IF of migrated cells across the membrane; histogram representing the percentage of migrated cells.*

This data suggest that ITGA5 silencing partially impaired the ability to transmigrate through fibronectin coated membrane, indeed, more than 20% of cells are still able to transmigrate, probably due to recognition of fibronectin by other integrins (as α3β1, αVβ1, αVβ3 integrins) or fibronectin-independent migration. When cultured on Matrigel, ITGA5 silenced cells display a completely different organization compared to control and it is tempting to speculate an impairment in cell-cell adhesion contacts.

3.1. *In vivo* tumor growth of RH30 upon ITGA5 differential expression: mouse model

Flow cytometry analysis proved the expression of ITGA5 in 13.5% of RH30 cells. Gates were set to select by FACS two RH30 populations: one enriched in cells expressing ITGA5 (ITGA5^{high}) and a second enriched in cells that do not express ITGA5 (ITGA5^{low}) (Figure 3.18A). After a first step of expansion, the differential expression of ITGA5 was verified by flow cytometry (Figure 3.18B). After 4 passages, the ITGA5^{high} sorted cells had twice the ITGA5 expressing population of ITGA5^{low} counterpart (20.0% and 9.1% respectively). ITGA5^{high} and ITGA5^{low} populations were used for injection in recipient mice and xenografts production. The attained masses were measured and weighted to determine if the differential expression of ITGA5 has effects on the tumors size. Neither volume nor weight showed significant variation between the two groups (Figure 3.18C). Tumor masses were digested to analyse ITGA5 expression reporting the maintenance of differential expression levels between the two groups (Figure 3.18D).

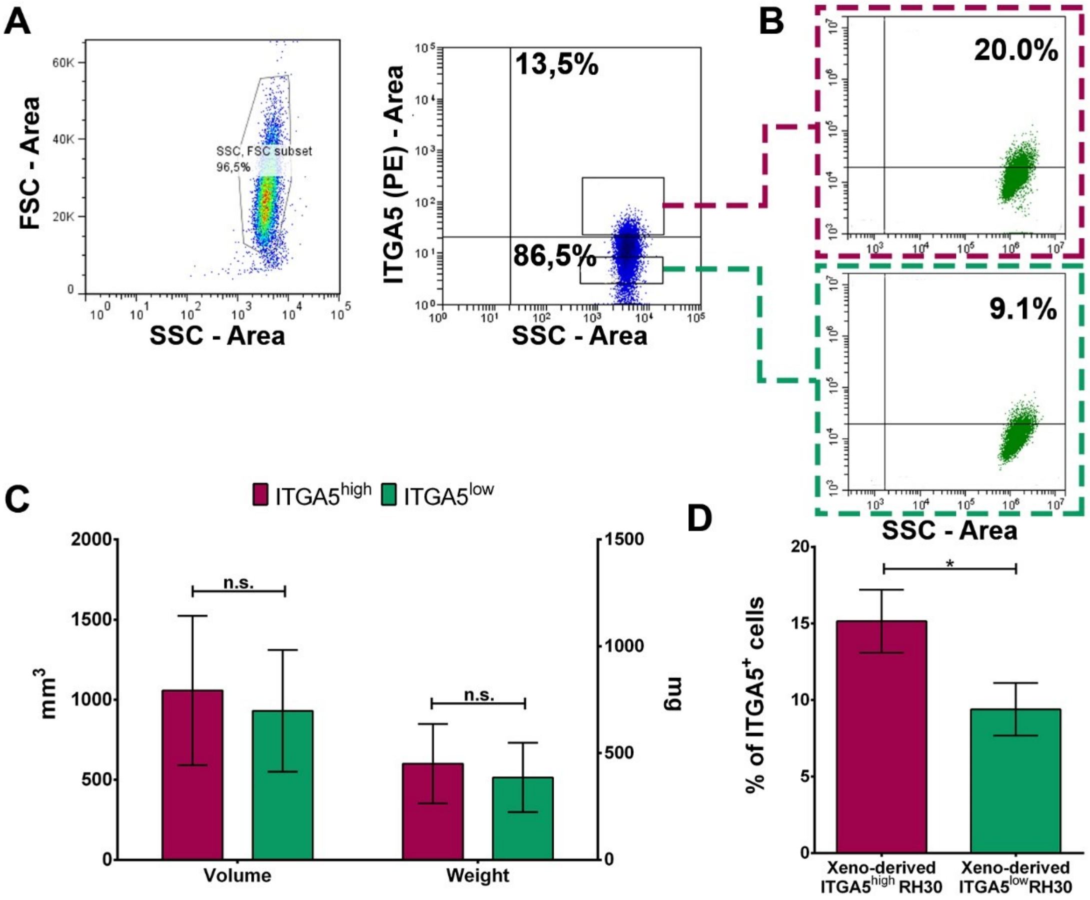

Figure 3.18:* *A. *Cytograms of ITGA5 stained RH30 cells: gate for single cell detection (on the left) and gates for selection of ITGA5$^+$ (green) and ITGA5$^-$ (purple) populations(on the right);* ***B.*** *ITG expressing levels in the two populations after 4 passages in culture;* ***C.*** *Histograms displaying volume and weight of xenografts produced by injection of ITGA5$^+$ (green) and ITGA5$^-$ (purple) populations;* ***D.*** *Flow cytometry showing ITGA5 expression in cells isolated from the xenograft produced with the two ITGA5$^+$ (green) and ITGA5$^-$ (purple) populations.*

In parallel, the two populations were injected in 48 hours post fertilization (hpf) zebrafish embryos to determine if the adhesion molecule have a role in bio-distribution and metastatic potential of ARMS cells. Cell distribution was assessed at 4 hours post injection (hpi), 24 hpi and 48 hpi. At the first two time-points no substantial differences were seen between the two populations; clustering of RH30 on the caudal vein plexus of the embryos was possibly due to passive accumulation where the blood flow was lower, and the vessels have smaller diameter. At 48 hpi RH30 cells started to actively extravasate from ventral and intersomitic vessels invading the somites (Figure 3.19A). Extravasation frequency was reported to be higher in zebrafishes injected with ITGA5^{high} RH30 (19/62 events) than the one injected with ITGA5^{low} (5/59 events) (Figure 3.19B).

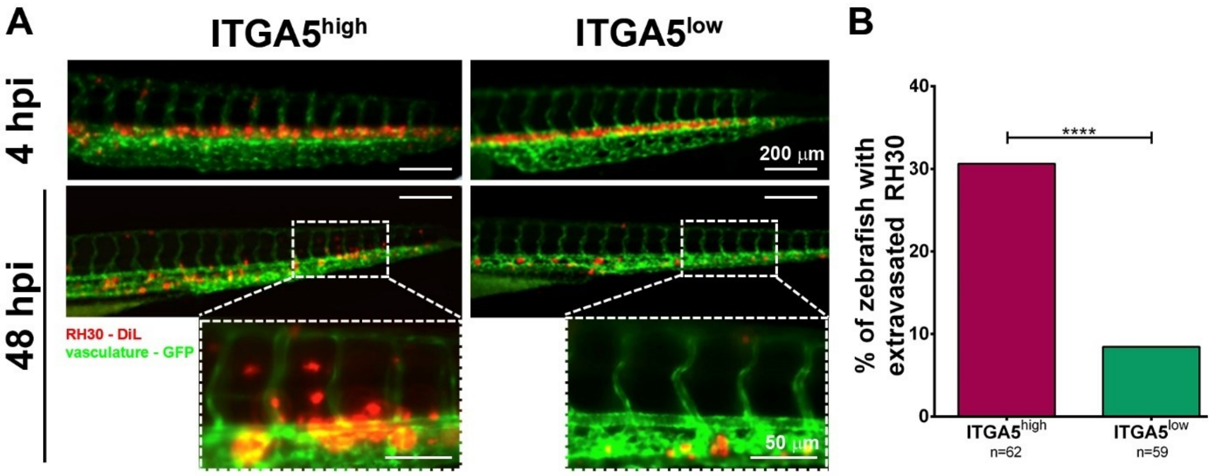

Figure 3.19: A. *Representative live images of RH30 ITGA5^{high} and ITGA5^{low} cells injected in zebrafish embryos at 4 hpi and 48 hpi; at the latter time-points extravasating cells can be visualized in the close-up;* ***B.*** *Histogram representing the difference in frequency of extravasation of the two population of RH30 at 48 hpi.*

This data taken together demonstrate that enhanced expression of ITGA5 *in vivo* did not affect tumor growth in mice. By injecting the two population in zebrafish Yolk sac, a higher extravasation frequency was observed in ARMS cells enriched in cells expressing ITGA5. Overall, ITGA5 appeared not to be indispensable for tumor growth *in vivo* rather than playing a role in metastatic extravasation.

Discussion

While in the last years the genetic background of RMS has been extensively studied, the characterization of the tumor microenvironment and the development of models able to recapitulate the complexity of RMS stroma are still in their infancy. This pioneer work aimed to dissect and re-built RMS microenvironment using three different 3D models to investigate integrin-mediated cell migration. A deeper knowledge of the cancer microenvironment, also in the case of RMS, would unveil multicellular interactions and complex mechanisms of tumor biology, as chemoresistance, neovascularization, immuno-editing and metastatic dissemination, hopefully together with new targeted therapies [108].

One of the major challenges in the study of RMS is the rarity of the disease. Indeed, the paucity of RMS patients within the cohorts affects statistical significance of the research. In the case of gene expression analyses, data from different datasets can be merged – considering adaptations for platform used, normalization methods and study design – in a unique, larger dataset and this can be interrogated to discover dysregulated genes or disease-associated pathways, achieving statistical significance in the analyses [109,110]. More importantly, datasets can integrate genomic and transcriptomic profiles with epigenomic, proteomic and phospho-proteomic information, offering more powerful collection of data for the identification of potential molecular targets and design new therapeutic approaches [111].

To begin our study on RMS stroma, we started from publicly available gene expression datasets. In our analyses, we observed the differential regulation of a subset of genes related to the adhesion molecules integrin $\alpha 5$ and integrin $\beta 1$. Among these genes we selected the ones relative to ECM proteins, by cross-reference with Matrisome dataset, and used differential expression of these genes in other RMS patient datasets, to cluster separately ARMS and ERMS patients and validate the gene list. We then proved that, at transcriptomic level, ECM genes related to ITGA5 and ITGB1 are differentially regulated between ARMS and ERMS. This led us to hypothesize that the differences in the two ECMs, and genes related to integrins binding these ECM proteins, could translate into difference in cell motility and aggressiveness of the two RMS subtypes. Similarly, the link between remodelled ECM and disease progression has been previously demonstrated in many types of cancer as colon [112], breast [113] and skin [114].

In general, to prove the functional significance of bioinformatic analyses, molecular target or altered pathways have to be tested with *in vitro* or *in vivo* models that are representative of the biological process investigated. In our case, since the 2D traditional cell cultures limit the possibility to recreate a model of cell migration that recapitulates the tissue complexity and ECM interactions, we considered three different models of 3D culture where ARMS cells can interact with ARMS specific ECM.

Tissue decellularization allows the obtainment of the acellular ECM (dECM). With a well-balanced protocol between removal of cellular components and preservation of ECM proteins, dECMs represent the most comparable scaffolds to the naïve tissue, with high number of ECM- and ECM-associated proteins that are almost impossible to include in artificial 3D constructs, moreover, the tissue architecture is maintained.

Many tumor models take advantage of this complexity to recreate the environment of primary or metastatic site of the malignancy and investigate disease progression, tumor growth, cell migration, drug resistance and immune cell polarization [115–120].

To follow this line, due to limited amount of human biopsies, we developed and characterized a representative xenogenic model of ARMS from which we obtained the tumor masses for decellularization. Decellularization procedure of ARMS xenogenic tissues proved to efficiently remove cellular fraction while preserving the main ECM structural proteins. However, in our hands, the tested recellularization strategies were inefficient in achieving homogeneous recellularization of the dECM scaffolds.

Although microinjection technique allowed the cell seeding directly into the matrix core, the high expertise required to use the microinjector, the risk of sample contamination and the low cell viability and proliferation, prompt us to change strategy. We decided to consider the use of a perfusion system to achieve homogeneous seeding and overcome the limit of nutrient diffusion through the scaffold.

Using U-Cup perfusion bioreactor the recellularization efficiency was not improved as expected and dynamic seeding resulted in cell adhesion manly on the external surface of the matrices. This is mainly due to extremely low porosity of the dECM compared to the traditional scaffolds used with perfusion bioreactors (e.g. Ultrafoam collagen I sponge). Freeze and thaw cycles, implemented to enlarge the pores in the dECM, have proven to be insufficient to enhance porosity and recellularization efficiency of the scaffolds. Loss of other ECM components and maintenance of tissue architecture has also to be evaluated since freeze and thaw is also used as physical method for decellularization [121].

The use of dECM remains the optimal support for tissue-like 3D culture; however, in our case, the high density and low porosity of ARMS decellularized matrix limits the ability of cells to repopulate homogeneously the scaffold displaying enhanced cell-cell instead of cell-ECM interactions. Increasing surface/volume ratio of dECM supports – by laser perforation or cutting samples in smaller chunks before perfusion – would offer more adhesion sites for cells.

The direct use of ARMS dECM, defined as "conservative" approach, was then temporary abandoned in favour of a deconstructive analysis of ARMS ECM that gains information on protein composition of the ECM, useful information for development of 3D bottom-up models: the "deconstructive" approach. Bottom-up approaches could overcome the limitation of starting material, offering an off the shelf platform with limited batch to batch variability. The development of an artificial 3D model requires the knowledge of the molecular composition and physical properties of the tissue that has to be recreated. For this reason, we decided to sacrifice the information regarding tissue architecture performing a decellularization protocol that maximized the removal of cellular proteins and solubilize ECM proteins for mass-spectrometry analysis [106].

Our results on ARMS xenografts allowed to shed light on protein composition of ARMS ECM and reported a high presence of collagens (collagen I and collagen III); among glycoproteins the most represented were fibrillin, fibronectin and periostin, while the contribution of proteoglycans seemed to be minimal. Further development of this deconstructive approach will include the characterization in protein composition of pediatric healthy muscle tissue, that will be compared with RMS tissue to identify differentially expressed disease-specific ECM proteins.

Two bottom-up 3D models were investigated for reconstructing ARMS microenvironment: one based on Ultrafoam collagen I sponge in combination with the U-Cup perfusion bioreactor, the other based on hyaluronic acid / PEG hydrogel enriched with fibronectin. The choice to use these two scaffolds is related to the type of analysis that has to be performed, considering advantages and disadvantages of each system.

Results obtained with Ultrafoam collagen I scaffold, cultured in dynamic perfusion bioreactor, showed uniform surface seeding at 7 days in culture, sustained proliferation and secretion of the matrix remodelling enzyme MMP-2 together with enhanced expression of ITGA5 and CXCR4. U-Cup bioreactor allowed long term cultures and formation of relatively large tissue-like structures. In the dynamic system it is easy to include other cell types – as endothelial or immune cells – at later timepoints, add stimulatory molecules or analyse the soluble factors secreted in the supernatant without perturbing the culture.
One of the biggest limits of perfusion bioreactor is that during culture, cells are inaccessible for live imaging, forcing to stop the experiment for direct analysis on cells. Moreover, even if Ultrafoam is mainly collagen I, and collagen I is the most representative protein of ARMS ECM, this represent only a minimal part of the ECM complexity. Further enrichments with other ARMS ECM proteins has to be considered but the functionalization of scaffolds as Ultrafoam can be trivial due to diffusion limit of other large proteins in the already formed collagen mesh.

The development and optimization of hyaluronic acid/PEG hydrogel is still ongoing. Attained results demonstrate the formation of a 3D support for cell culture that sustains cell viability up to 10 days. Incorporation of fibronectin in the scaffold has to be optimized and other ECM proteins has been recently implemented. HA/PEG hydrogels, and hydrogels in general, are optically transparent and allow live imaging of cultured cells, enabling studies cell motility. Nevertheless, hydrogels are static cultures and long-term experiments are difficult to maintain. Addition of other cell types for co-cultures has to be done before gel reticulation, resulting in homogeneous distribution of the cell types, or including the cured gel in a second layer of hydrogel with the other cell type, resulting in heterogeneous distribution between the inner and outer gel. Besides these complications, hydrogels offer a finely tuneable support in terms of physical properties, as stiffness and porosity, together with a relatively simple procedures for functionalization of scaffold backbone [122–124] making them suitable for modelling different tumor microenvironments [125–128].

In this work we developed in parallel three platforms – using a conservative or deconstructive approach – for 3D culture, focusing on the role of integrins in cell migration. Culturing ARMS cells on Ultrafoam scaffold, we reported an increase in ITGA5 expression together with CXCR4 receptor. Integrin α5 is reported to interact with integrin β1 to form the dimeric receptor for fibronectin and is associated with stemness and metastasis in triple negative breast cancer [129–132], oral squamous carcinoma [133] and renal carcinoma [134]. We then asked if ITGA5 is involved in ARMS cell migration.

Fibronectin, ligand of ITGA5, orchestrates different biological processes in several types of tumors: in hepatocellular carcinoma it enhances cell migration and invasion and correlates with poor prognosis of patients [135]; it promotes extravasation of colorectal cancer circulating cells from liver endothelium [136]; fibronectin networks, deposited by stromal CAF, showed to guide migration of prostate cancer cells and head and neck squamous cell carcinomas [137,138]. Similarly, in our experiments, RH30 cells displayed enhanced migration on fibronectin-coated surfaces compared to uncoated controls.

The migratory and invasive potential of ARMS cells, in absence or presence of ITGA5 expression, have been investigated *in vitro* transfecting RH30 cells with anti-ITGA5 siRNA. The two assays – transwell migration and transwell invasion – were performed within 24 hours after transfection to ensure reduced levels of ITGA5 mRNA. While only partial reduction in number of migrating cells is reported for ITGA5 silenced cells, probably due to "rescue" effect of other fibronectin-binding integrins (α4β1, α4β7, αvβ3, αvβ5, αvβ6, αvβ1, α3β1, α8β1 and α9β1) [139]; an unexpected difference in cell organization is reported in the invasion assays. Neither silenced nor control cells were able to invade and transmigrate trough the gel in 24 hours, with transfected cells displaying a completely different organization from the control group: cells clustered in small spherical aggregates instead forming large multicellular strands. This effect could be due to impairment of cell-cell contact rather than cell-ECM adhesions and further experiments are needed to clarify if impairment of ITGA5 expression induces also reorganization of cell-cell contacts. Crosstalk between integrin adhesions and cadherin complexes are already reported in other types of cancer and during development, for example: E-cadherin has been shown to regulate lamellipodia activity and integrin-mediated cell migration on collagen IV surfaces in epithelial cells [140]; in renal carcinoma, loss of E-cadherin – hallmark of epithelial to mesenchymal transition and enhanced migratory ability of cancer cells – induced by TGF-β1, is further enhanced by αvβ3 integrin signaling activation [141]; in ovarian cancer Wnt11 has been shown to up-regulate E- and N-cadherin expression and down-regulate expression of integrins α5, β2, β3 and β6 resulting in impaired migration, invasion and no tumor growth or metastasis *in vivo* [142]; finally migration on fibronectin of neural crest cells depends on integrins β3 and β1 and alterations on these adhesion molecules impaired migration inducing N-cadherin mediated cell clustering [143].

In vivo experiments required longer periods – 3 days in zebrafish up to 3 weeks in mice – and, since siRNA silencing efficiency decrease over time, we sorted by FACS two RH30 cell populations: one enriched in cells that express ITGA5 at high level and the second enriched in cells expressing ITGA5 at lower level. After proving that this difference in ITGA5 expression can be maintained over time, we searched for correlation between integrin expression level and tumor growth or metastatic potential in two different animal models.

We used mice to access the difference in tumor growth between the two populations (ITGA5^{high} and ITGA5^{low}) since flank injection in immunodeficient mice is very efficient in mimicking primary site of the disease. No differences were seen in tumor weight or size; however, cytofluorimetric analysis revealed that the difference in ITGA5 expression was maintained between the two groups even after 3 weeks, suggesting that ITGA5 was not indispensable for tumor formation and growth. The role of integrins in tumor proliferation has been assessed in other tumors: integrin α6 in glioblastoma identify a cancer stem cells population, siRNA targeting of this integrin impairs cell proliferation, survival, self-renewal, and *in vivo* growth [144]. In a mouse model of human breast cancer, integrin β1 is necessary for tumor initiation and proliferation *in vivo* [145]; finally, integrin α9β1 in breast cancer has shown to contribute to *in* vivo tumor growth, lymphatic metastasis and recruitment of CAF [146].

To determine the metastatic migration potential of ITGA5^{high} and ITGA5^{low} ARMS cells we used the zebrafish model. Cells enriched in ITGA5 expression displayed higher extravasation rates suggesting that this integrin could be involved in the metastatic process. Other integrins have been reported to mediate extravasation process: the role of $\beta1$ integrin in extravasation has been verified in breast carcinoma using a microfluidic model that recreates the microvascular network [147]; *in vivo* studies in metastatic breast and melanoma models highlighted the role of integrin $\alpha v\beta3$ in extravasation from pulmonary endothelium together with platelet degranulation [148]; an atypical interaction is reported, in metastatic model of aggressive breast cancer, between integrin $\beta1$ and the hepatocyte growth factor receptor (c-Met) resulting in the assembly of a receptor with enhanced affinity for fibronectin and displaying higher extravasation rates from the pulmonary endothelium [149].

Conclusions

In conclusion, we here reported three different models of alveolar rhabdomyosarcoma:

1. Extracellular matrix derived from decellularization of xenogenic tumors;
2. Ultrafoam collagen I sponge in combination with perfusion bioreactor;
3. Hyaluronic acid/PEG hydrogel enriched with ARMS specific ECM proteins.

Regarding the choice of the best model it is important to consider which is the biological question that has to be answered, the advantages and the limitations of each model.

Decellularized ECM offers the most heterogeneous support representative of ARMS tissue complexity; however, recellularization can be trivial due to low porosity and limited diffusion in the core of the scaffold. Moreover, since the xenograft is derived from animals, dECMs can be subjected to batch-to-batch variability. Recellularization issue could be addressed increasing the surface/volume ratio, to provide more adhesion sites to ARMS cells and to reduce the volume excluded from nutrient diffusion. If the diffusion would be improved, dECM could be used in combination with perfusion bioreactor or, if the thickness would be thin enough (50-100 μm), scaffolds could be used for superficial cell seeding and live imaging on confocal microscope. Finally, digested decellularized ECM could be used to enrich hyaluronic acid/PEG hydrogels but, in this case, the spatial information of ECM topology would be lost. It is important to acknowledge that human ARMS biopsies are generally very small and extremely precious for pathologists; as a consequence, the starting material to obtain a patient-derived 3D scaffold for personalized drug screening may be insufficient. Conversely, gaining the information on molecular composition of patient ARMS ECM, as we have done for the xenografts, requires minimal amount of tissue and the acquired information could be included in patient datasets or used to develop an off the shelf ARMS specific scaffolds that includes the most representative ECM proteins, as described in the "deconstructive" approach.

The U-Cup bioreactor with Ultrafoam scaffold and enriched hyaluronic acid/PEG hydrogel are 2 alternative models generated with the "deconstructive" approach, which presumes the knowledge of the molecular composition of ARMS ECM, sacrificing the information on tissue architecture.
U-Cup perfusion bioreactor offers dynamic seeding and culture conditions were, thanks to active perfusion of fresh medium and gas exchange, relatively large tissue-like constructs can be obtained in few days. Ultrafoam collagen I sponge, has the advantage to be commercially available, clinical grade and with minimal batch to batch variability. However, customization on this scaffold, by addition of other ARMS specific ECM proteins, is limited by the possibility to uniformly and covalently bind these proteins to the pre-existing framework. Other scaffolds are available on the market and if they better mimic ARMS microenvironment, for composition or physical properties, they can easily replace Ultrafoam. As anticipated above, U-Cup is inaccessible for live imaging but, during culture, medium can easily be collected for analysis of soluble proteins or microvescicles; additional seedings can be made to include other cell types establishing complex co-cultures. For these reasons U-Cup bioreactor is optimal for long-term, complex co-cultures but not suitable for direct cell visualization.

Hyaluronic/PEG hydrogel is still under development and preliminary results are encouraging. This model offers a consistent and easily tuneable scaffold for 3D culture where ARMS specific ECM proteins can be included in the gel mesh or covalently bound to hyaluronic acid backbone. As mentioned before, hydrogels are optically transparent, allow live imaging but cannot be perfused, co-cultures are complicated to establish and cell viability is reduced at longer timepoints. These characteristics make hydrogel useful for cell migration analyses and the use fluorescent reporters, but less functional for complex co-cultures and long-term cultures.

Further developments will include the study of ITGA5 function in ARMS migration on fibronectin and collagen enriched hyaluronic/PEG hydrogel, to mimic migration in the specific ARMS context. We would like also to conduct proteomic analysis of pediatric healthy muscle ECM to identify which are the dysregulated ECM proteins in ARMS microenvironment and find other potential molecular partners that can cooperate to ARMS metastatic migration. In future, we aim to apply the optimized models for the study of other complex biological processes as vascularization, immune editing and drug resistance.

Acknowledgments

This work was possible thanks to Fondazione Istituto di Ricerca Pediatrica Città della Speranza financial support.

I personally want to thank my tutors Prof. Maurizio Muraca and Dott.ssa Michela Pozzobon for having me in their lab, for teaching me what I know now and for having assisted the progresses of my professional career. I want to acknowledge also my colleagues Michele, Stefania, Annamaria and master students that worked in the Regenerative Medicine Lab – Fabio, Anna, Alessia, Federica, Riccardo, Marco and Agner – for sharing many hours of hard work and stressful periods but also many lunches and table tennis matches. Thanks to all the collaborators that helped me in the experimental procedures and dedicated some of their time to teach me something new: Martina Piccoli, Beppe Germano, Elena Rampazzo, Diana Corallo, Sara D'Aronco, Sara Crotti, Carlo Zanon and Chiara Frasson.

Special thanks to the Tissue Engineering group at Basel University and to Prof. Ivan Martin, for hosting me for ten extraordinary months in his lab, for motivating me in moments of hardship and being always extraordinarily helpful. A heartfelt thanks to my formal tutor Manuele Muraro for being more than precious guide that helped me inside and outside the lab, and for sharing priceless ideas, deep thoughts and passions.

In the lab I had the chance to learn new techniques for my experiments, but I also met many friend that made me feel like at home. Many thanks to Diana Robles, Giuseppe Isu, Gyözö Lehoczky, Paul Bourgine, Valeria Governa, Sebastian Pigeot, Miriam Filippi, Paola Occhetta, Boris Dasen, Clementine Le Magnen and all the other friends and colleagues that shared joyful time and tasty culinary traditions Alina, Gordian, Majoska, Lina, Andrea, Shikha, Andres, Chiara, Davide, Alessia, Deborah, Gregor, Francesca, Christoph, Laia, Vlad, Mansoor, Jesil, Jan, Laura, Max, Julien and Thibaut.

My highest gratitude to my parents Franca and Giordano that never stopped believing in me and always supported me. I owe all my successes to them and I will never thank them enough for their sacrifices.

Finally, thanks to all my friends in Padua and Verona, pleasant and indispensable distractions from my duties and companions of many adventures : Valentina, Andrea C., Marco, Edoardo C., Silvia, Alice, Carmine, Edoardo M., Andrea S. and many others.

Bibliography

1. Taylor, B. S. *et al.* Advances in sarcoma genomics and new therapeutic targets. *Nat. Rev. Cancer* **11**, 541–557 (2011).
2. Helman, L. J. & Meltzer, P. Mechanisms of sarcoma development. *Nat. Rev. Cancer* **3**, 685–694 (2003).
3. Jo, V. Y. & Fletcher, C. D. M. WHO classification of soft tissue tumours: an update based on the 2013 (4th) edition. *Pathology* **46**, 95–104 (2014).
4. Taylor, B. S. *et al.* Advances in sarcoma genomics and new therapeutic targets. *Nat. Rev. Cancer* **11**, 541–557 (2011).
5. Ognjanovic, S., Linabery, A. M., Charbonneau, B. & Ross, J. A. Trends in childhood rhabdomyosarcoma incidence and survival in the United States, 1975-2005. *Cancer* **115**, 4218–4226 (2009).
6. Ferrari, A. *et al.* Synovial sarcoma: A retrospective analysis of 271 patients of all ages treated at a single institution. *Cancer* **101**, 627–634 (2004).
7. Sultan, I., Qaddoumi, I., Yaser, S., Rodriguez-Galindo, C. & Ferrari, A. Comparing Adult and Pediatric Rhabdomyosarcoma in the Surveillance, Epidemiology and End Results Program, 1973 to 2005: An Analysis of 2,600 Patients. *J. Clin. Oncol.* **27**, 3391–3397 (2009).
8. Parham, D. M. & Barr, F. G. Classification of Rhabdomyosarcoma and Its Molecular Basis. *Adv. Anat. Pathol.* **20**, 387–397 (2013).
9. Sorensen, P. H. B. *et al.* PAX3-FKHR and PAX7-FKHR Gene Fusions Are Prognostic Indicators in Alveolar Rhabdomyosarcoma: A Report From the Children's Oncology Group. *J. Clin. Oncol.* **20**, 2672–2679 (2002).
10. Galili, N. *et al.* Fusion of a fork head domain gene to PAX3 in the solid tumour alveolar rhabdomyosarcoma. *Nat. Genet.* **5**, 230–235 (1993).
11. Davicioni, E. *et al.* Identification of a PAX-FKHR gene expression signature that defines molecular classes and determines the prognosis of alveolar rhabdomyosarcomas. *Cancer Res.* **66**, 6936–6946 (2006).
12. Weber-Hall, S. *et al.* Gains, losses, and amplification of genomic material in rhabdomyosarcoma analyzed by comparative genomic hybridization. *Cancer Res.* **56**, 3220–4 (1996).
13. Anderson, J., Gordon, A., Pritchard-Jones, K. & Shipley, J. Genes, chromosomes, and rhabdomyosarcoma. *Genes Chromosom. Cancer* **26**, 275–285 (1999).
14. Shern, J. F. *et al.* Comprehensive Genomic Analysis of Rhabdomyosarcoma Reveals a Landscape of Alterations Affecting a Common Genetic Axis in Fusion-Positive and Fusion-Negative Tumors. *Cancer Discov.* **4**, 216–231 (2014).
15. Hettmer, S. & Wagers, A. J. Uncovering the origins of rhabdomyosarcoma. *Nat. Med.* **16**, 171–173 (2010).
16. Keller, C. & Capecchi, M. R. New Genetic Tactics to Model Alveolar Rhabdomyosarcoma in the Mouse. *Cancer Res.* **65**, 7530–7532 (2005).
17. Ren, Y.-X. *et al.* Mouse Mesenchymal Stem Cells Expressing PAX-FKHR Form Alveolar Rhabdomyosarcomas by Cooperating with Secondary Mutations. *Cancer Res.* **68**, 6587–6597 (2008).

18. Rubin, B. P. *et al.* Evidence for an Unanticipated Relationship between Undifferentiated Pleomorphic Sarcoma and Embryonal Rhabdomyosarcoma. *Cancer Cell* **19**, 177–191 (2011).

19. Srinivas, B. P., Woo, J., Leong, W. Y. & Roy, S. A conserved molecular pathway mediates myoblast fusion in insects and vertebrates. *Nat. Genet.* **39**, 781–786 (2007).

20. Kashi, V. P., Hatley, M. E. & Galindo, R. L. Probing for a deeper understanding of rhabdomyosarcoma: Insights from complementary model systems. *Nat. Rev. Cancer* **15**, 426–439 (2015).

21. Chen, H. J. *et al.* A recellularized human colon model identifies cancer driver genes. *Nat. Biotechnol.* **34**, 845–851 (2016).

22. Baker, B. M. & Chen, C. S. Deconstructing the third dimension – how 3D culture microenvironments alter cellular cues. *J. Cell Sci.* **125**, 3015–3024 (2012).

23. Nath, S. & Devi, G. R. Three-dimensional culture systems in cancer research: Focus on tumor spheroid model. *Pharmacol. Ther.* **163**, 94–108 (2016).

24. Colella, G. *et al.* Sarcoma Spheroids and Organoids—Promising Tools in the Era of Personalized Medicine. *Int. J. Mol. Sci.* **19**, 615 (2018).

25. Ciccarelli, C. *et al.* Key role of MEK/ERK pathway in sustaining tumorigenicity and in vitro radioresistance of embryonal rhabdomyosarcoma stem-like cell population. *Mol. Cancer* **15**, 1–15 (2016).

26. Codenotti, S. *et al.* Caveolin-1 enhances metastasis formation in a human model of embryonal rhabdomyosarcoma through Erk signaling cooperation. *Cancer Lett.* **449**, 135–144 (2019).

27. Thuault, S. *et al.* The RhoE/ROCK/ARHGAP25 signaling pathway controls cell invasion by inhibition of Rac activity. *Mol. Biol. Cell* **27**, 2653–2661 (2016).

28. Mehling, M. & Tay, S. Microfluidic cell culture. *Curr. Opin. Biotechnol.* **25**, 95–102 (2014).

29. van Duinen, V., Trietsch, S. J., Joore, J., Vulto, P. & Hankemeier, T. Microfluidic 3D cell culture: from tools to tissue models. *Curr. Opin. Biotechnol.* **35**, 118–126 (2015).

30. Huh, D., Hamilton, G. a. & Ingber, D. E. From 3D cell culture to organs-on-chips. *Trends Cell Biol.* **21**, 745–754 (2011).

31. Bersini, S. *et al.* A microfluidic 3D in vitro model for specificity of breast cancer metastasis to bone. *Biomaterials* **35**, 2454–2461 (2014).

32. Knowlton, S., Onal, S., Yu, C. H., Zhao, J. J. & Tasoglu, S. Bioprinting for cancer research. *Trends Biotechnol.* **33**, 504–513 (2015).

33. Murphy, S. V & Atala, A. 3D bioprinting of tissues and organs. *Nat. Biotechnol.* **32**, 773–785 (2014).

34. Fong, E. L. S. *et al.* Modeling Ewing sarcoma tumors in vitro with 3D scaffolds. *Proc. Natl. Acad. Sci.* **110**, 6500–6505 (2013).

35. Gaebler, M. *et al.* Three-Dimensional Patient-Derived In Vitro Sarcoma Models: Promising Tools for Improving Clinical Tumor Management. *Front. Oncol.* **7**, 1–14 (2017).

36. Crapo, P. M., Gilbert, T. W. & Badylak, S. F. An overview of tissue and whole organ decellularization processes. *Biomaterials* **32**, 3233–3243 (2011).

37. GILBERT, T., SELLARO, T. & BADYLAK, S. Decellularization of tissues and organs. *Biomaterials* **27**, 3675–3683 (2006).

38. Badylak, S. F., Taylor, D. & Uygun, K. Whole Organ Tissue Engineering: Decellularization and Recellularization of Three-Dimensional Matrix Scaffolds. *Annu. Rev. Biomed. Eng.* **13**, 110301095218061 (2010).

39. Taylor, D. A., Sampaio, L. C., Ferdous, Z., Gobin, A. S. & Taite, L. J. Decellularized matrices in regenerative medicine. *Acta Biomater.* **74**, 74–89 (2018).

40. Hoshiba, T. Decellularized Extracellular Matrix for Cancer Research. *Materials (Basel).* **12**, 1311 (2019).

41. Piccoli, M., Trevisan, C., Maghin, E., Franzin, C. & Pozzobon, M. Mouse Skeletal Muscle Decellularization. in **12**, 87–93 (2017).

42. Piccoli, M. *et al.* Improvement of diaphragmatic performance through orthotopic application of decellularized extracellular matrix patch. *Biomaterials* **74**, 245–255 (2016).

43. Alvarèz Fallas, M. *et al.* Decellularized Diaphragmatic Muscle Drives a Constructive Angiogenic Response In Vivo. *Int. J. Mol. Sci.* **19**, 1319 (2018).

44. Trevisan, C. *et al.* Allogenic tissue-specific decellularized scaffolds promote long-term muscle innervation and functional recovery in a surgical diaphragmatic hernia model. *Acta Biomater.* **89**, 115–125 (2019).

45. Pozzobon, M. *et al.* Alveolar Rhabdomyosarcoma Decellularization. in **12**, 317–325 (2017).

46. Pati, F. *et al.* Printing three-dimensional tissue analogues with decellularized extracellular matrix bioink. *Nat. Commun.* **5**, 3935 (2014).

47. Balkwill, F. R., Capasso, M. & Hagemann, T. The tumor microenvironment at a glance. *J. Cell Sci.* **125**, 5591–5596 (2012).

48. Naba, A. *et al.* The Matrisome: In Silico Definition and In Vivo Characterization by Proteomics of Normal and Tumor Extracellular Matrices. *Mol. Cell. Proteomics* **11**, (2012).

49. Hynes, R. O. & Naba, A. Overview of the Matrisome--An Inventory of Extracellular Matrix Constituents and Functions. *Cold Spring Harb. Perspect. Biol.* **4**, a004903–a004903 (2012).

50. Mittal, D., Gubin, M. M., Schreiber, R. D. & Smyth, M. J. New insights into cancer immunoediting and its three component phases—elimination, equilibrium and escape. *Curr. Opin. Immunol.* **27**, 16–25 (2014).

51. Raza, A., Franklin, M. J. & Dudek, A. Z. Pericytes and vessel maturation during tumor angiogenesis and metastasis. *Am. J. Hematol.* **85**, 593–598 (2010).

52. Tomlinson, J. *et al.* Different patterns of angiogenesis in sarcomas and carcinomas. *Clin. Cancer Res.* **5**, 3516–22 (1999).

53. Gerber, H. P., Kowalski, J., Sherman, D., Eberhard, D. A. & Ferrara, N. Complete inhibition of rhabdomyosarcoma xenograft growth and neovascularization requires blockade of both tumor and host vascular endothelial growth factor. *Cancer Res.* **60**, 6253–8 (2000).

54. Gee, M. F. W. *et al.* Vascular endothelial growth factor acts in an autocrine manner in rhabdomyosarcoma cell lines and can be inhibited with all-trans-retinoic acid. *Oncogene* **24**, 8025–8037 (2005).

55. Miyoshi, K. *et al.* Close correlation between CXCR4 and VEGF expression and frequent CXCR7 expression in rhabdomyosarcoma. *Hum. Pathol.* **45**, 1900–1909 (2014).

56. Ehnman, M. *et al.* Distinct Effects of Ligand-Induced PDGFR and PDGFR Signaling in the Human Rhabdomyosarcoma Tumor Cell and Stroma Cell Compartments. *Cancer Res.* **73**, 2139–2149

(2013).

57. Taniguchi, E. *et al.* PDGFR-A is a therapeutic target in alveolar rhabdomyosarcoma. *Oncogene* **27**, 6550–6560 (2008).

58. Dancsok, A. R., Asleh-Aburaya, K. & Nielsen, T. O. Advances in sarcoma diagnostics and treatment. *Oncotarget* **8**, 7068–7093 (2017).

59. Maniotis, A. J. *et al.* Vascular Channel Formation by Human Melanoma Cells in Vivo and in Vitro: Vasculogenic Mimicry. *Am. J. Pathol.* **155**, 739–752 (1999).

60. Hendrix, M. J. C., Seftor, E. A., Hess, A. R. & Seftor, R. E. B. Vasculogenic mimicry and tumour-cell plasticity: lessons from melanoma. *Nat. Rev. Cancer* **3**, 411–421 (2003).

61. Sun, B., Zhang, S., Zhao, X., Zhang, W. & Hao, X. Vasculogenic mimicry is associated with poor survival in patients with mesothelial sarcomas and alveolar rhabdomyosarcomas. *Int. J. Oncol.* **25**, 1609–14 (2004).

62. Chen, L., He, Y., Sun, S., Sun, B. & Tang, X. Vasculogenic mimicry is a major feature and novel predictor of poor prognosis in patients with orbital rhabdomyosarcoma. *Oncol. Lett.* **10**, 1635–1641 (2015).

63. Dunn, G. P., Bruce, A. T., Ikeda, H., Old, L. J. & Schreiber, R. D. Cancer immunoediting: from immunosurveillance to tumor escape. *Nat. Immunol.* **3**, 991–998 (2002).

64. Gajewski, T. F., Schreiber, H. & Fu, Y.-X. Innate and adaptive immune cells in the tumor microenvironment. *Nat. Immunol.* **14**, 1014–1022 (2013).

65. Grivennikov, S. I., Greten, F. R. & Karin, M. Immunity, Inflammation, and Cancer. *Cell* **140**, 883–899 (2010).

66. Erreni, M., Mantovani, A. & Allavena, P. Tumor-associated Macrophages (TAM) and Inflammation in Colorectal Cancer. *Cancer Microenviron.* **4**, 141–154 (2011).

67. Chanmee, T., Ontong, P., Konno, K. & Itano, N. Tumor-associated macrophages as major players in the tumor microenvironment. *Cancers (Basel).* **6**, 1670–1690 (2014).

68. Werb, Z. & Lu, P. The Role of Stroma in Tumor Development. *Cancer J.* **21**, 250–253 (2015).

69. D'Angelo, S. P. *et al.* Prevalence of tumor-infiltrating lymphocytes and PD-L1 expression in the soft tissue sarcoma microenvironment. *Hum. Pathol.* **46**, 357–365 (2015).

70. Bertolini, G. *et al.* PD-L1 assessment in pediatric rhabdomyosarcoma: a pilot study. *BMC Cancer* **18**, 652 (2018).

71. Johler, S. M., Fuchs, J., Seitz, G. & Armeanu-Ebinger, S. Macrophage migration inhibitory factor (MIF) is induced by cytotoxic drugs and is involved in immune escape and migration in childhood rhabdomyosarcoma. *Cancer Immunol. Immunother.* **65**, 1465–1476 (2016).

72. Kalluri, R. The biology and function of fibroblasts in cancer. *Nat. Rev. Cancer* **16**, 582–598 (2016).

73. Augsten, M. Cancer-Associated Fibroblasts as Another Polarized Cell Type of the Tumor Microenvironment. *Front. Oncol.* **4**, 1–8 (2014).

74. Kalluri, R. & Zeisberg, M. Fibroblasts in cancer. *Nat. Rev. Cancer* **6**, 392–401 (2006).

75. Alexander, J. & Cukierman, E. Stromal dynamic reciprocity in cancer: intricacies of fibroblastic-ECM interactions. *Curr. Opin. Cell Biol.* **42**, 80–93 (2016).

76. Labernadie, A. *et al.* A mechanically active heterotypic E-cadherin/N-cadherin adhesion enables fibroblasts to drive cancer cell invasion. *Nat. Cell Biol.* **19**, 224–237 (2017).

77. Tarnowski, M. *et al.* Macrophage Migration Inhibitory Factor Is Secreted by Rhabdomyosarcoma Cells, Modulates Tumor Metastasis by Binding to CXCR4 and CXCR7 Receptors and Inhibits Recruitment of Cancer-Associated Fibroblasts. *Mol. Cancer Res.* **8**, 1328–1343 (2010).

78. Ricard-Blum, S. The Collagen Family. *Cold Spring Harb. Perspect. Biol.* **3**, a004978–a004978 (2011).

79. Krieg, T., Timpl, R., Alitalo, K., Kurkinen, M. & Vaheri, A. Type III procollagen is the major collageneous component produced by a continuous rhabdomyosarcoma cell line. *FEBS Lett.* **104**, 405–409 (1979).

80. Vaheri, A., Kurkinen, M., Lehto, V.-P., Linder, E. & Timpl, R. Codistribution of pericellular matrix proteins in cultured fibroblasts and loss in transformation: Fibronectin and procollagen. *Proc. Natl. Acad. Sci.* **75**, 4944–4948 (1978).

81. KLEMAN, J.-P., HARTMANN, D. J., RAMIREZ, F. & REST, M. The human rhabdomyosarcoma cell line A204 lays down a highly insoluble matrix composed mainly of alpha1 type-XI and alpha2 type-V collagen chains. *Eur. J. Biochem.* **210**, 329–335 (1992).

82. Myers, J. C., Li, D., Rubinstein, N. A. & Clark, C. C. Up-regulation of Type XIX Collagen in Rhabdomyosarcoma Cells Accompanies Myogenic Differentiation. *Exp. Cell Res.* **253**, 587–598 (1999).

83. Oudart, J.-B. *et al.* The anti-tumor NC1 domain of collagen XIX inhibits the FAK/ PI3K/Akt/mTOR signaling pathway through avb3 integrin interaction. *Oncotarget* **7**, 1516–1528 (2016).

84. Sarrazin, S., Lamanna, W. C. & Esko, J. D. Heparan Sulfate Proteoglycans. *Cold Spring Harb. Perspect. Biol.* **3**, a004952–a004952 (2011).

85. Cassinelli, G., Zaffaroni, N. & Lanzi, C. The heparanase/heparan sulfate proteoglycan axis: A potential new therapeutic target in sarcomas. *Cancer Lett.* **382**, 245–254 (2016).

86. Ortiz, M. V., Roberts, S. S., Glade Bender, J., Shukla, N. & Wexler, L. H. Immunotherapeutic Targeting of GPC3 in Pediatric Solid Embryonal Tumors. *Front. Oncol.* **9**, 1–8 (2019).

87. Vogel, W., Kosmehl, H., Katenkamp, D. & Langbein, L. Differentiation dependent matrix formation (fibronectin and laminin) in an experimental murine rhabdomyosarcoma model. *Acta Histochem.* **90**, 181–188 (1991).

88. Vlodavsky, I. & Gospodarowicz, D. Respective roles of laminin and fibronectin in adhesion of human carcinoma and sarcoma cells. *Nature* **289**, 304–306 (1981).

89. Na, K. Y., Bacchini, P., Bertoni, F., Kim, Y. W. & Park, Y.-K. Syndecan-4 and fibronectin in osteosarcoma. *Pathology* **44**, 325–330 (2012).

90. Diomedi-Camassei, F. *et al.* Different pattern of matrix metalloproteinases expression in alveolar versus embryonal rhabdomyosarcoma. *J. Pediatr. Surg.* **39**, 1673–1679 (2004).

91. Ito, H. *et al.* Fibronectin-induced COX-2 mediates MMP-2 expression and invasiveness of rhabdomyosarcoma. *Biochem. Biophys. Res. Commun.* **318**, 594–600 (2004).

92. BOUCHÉ, M. *et al.* TGF-β autocrine loop regulates cell growth and myogenic differentiation in human rhabdomyosarcoma cells. *FASEB J.* **14**, 1147–1158 (2000).

93. Wang, S. *et al.* TGF-β1 signal pathway may contribute to rhabdomyosarcoma development by inhibiting differentiation. *Cancer Sci.* **101**, 1108–1116 (2010).

94. Friedl, P. & Alexander, S. Cancer Invasion and the Microenvironment: Plasticity and Reciprocity. *Cell* **147**, 992–1009 (2011).

95. Schmidt, S. & Friedl, P. Interstitial cell migration: integrin-dependent and alternative adhesion mechanisms. *Cell Tissue Res.* **339**, 83–92 (2010).

96. Guo, W. & Giancotti, F. G. Integrin signalling during tumour progression. *Nat. Rev. Mol. Cell Biol.* **5**, 816–826 (2004).

97. Canel, M., Serrels, A., Frame, M. C. & Brunton, V. G. E-cadherin-integrin crosstalk in cancer invasion and metastasis. *J. Cell Sci.* **126**, 393–401 (2013).

98. Leabu, M. *et al.* Integrin a2b1 modulates EGF stimulation of Rho GTPase-dependent morphological changes in adherent human rhabdomyosarcoma RD cells. *J. Cell. Physiol.* **202**, 754–766 (2005).

99. Masià, A. *et al.* Notch-mediated induction of N-cadherin and α9-integrin confers higher invasive phenotype on rhabdomyosarcoma cells. *Br. J. Cancer* **107**, 1374–1383 (2012).

100. Soler, A. P., Johnson, K. R., Wheelock, M. J. & Knudsen, K. A. Rhabdomyosarcoma-Derived Cell Lines Exhibit Aberrant Expression of the Cell-Cell Adhesion Molecules N-CAM, N-Cadherin, and Cadherin-Associated Proteins. *Exp. Cell Res.* **208**, 84–93 (1993).

101. Markus, M. A. *et al.* Cadherin-11 is highly expressed in rhabdomyosarcomas and during differentiation of myoblastsin vitro. *J. Pathol.* **187**, 164–172 (1999).

102. Charrasse, S., Comunale, F., Gilbert, E., Delattre, O. & Gauthier-Rouvière, C. Variation in cadherins and catenins expression is linked to both proliferation and transformation of Rhabdomyosarcoma. *Oncogene* **23**, 2420–2430 (2004).

103. Thuault, S. *et al.* P-cadherin is a direct PAX3–FOXO1A target involved in alveolar rhabdomyosarcoma aggressiveness. *Oncogene* **32**, 1876–1887 (2013).

104. Frankowski, H., Gu, Y.-H., Heo, J. H., Milner, R. & del Zoppo, G. J. Use of Gel Zymography to Examine Matrix Metalloproteinase (Gelatinase) Expression in Brain Tissue or in Primary Glial Cultures. in *Astrocytes* (ed. Milner, R.) **814**, 221–233 (Humana Press, 2012).

105. Lawson, N. D. & Weinstein, B. M. In Vivo Imaging of Embryonic Vascular Development Using Transgenic Zebrafish. *Dev. Biol.* **248**, 307–318 (2002).

106. Naba, A., Clauser, K. R. & Hynes, R. O. Enrichment of Extracellular Matrix Proteins from Tissues and Digestion into Peptides for Mass Spectrometry Analysis. *J. Vis. Exp.* 1–9 (2015). doi:10.3791/53057

107. Libura, J. CXCR4-SDF-1 signaling is active in rhabdomyosarcoma cells and regulates locomotion, chemotaxis, and adhesion. *Blood* **100**, 2597–2606 (2002).

108. Valkenburg, K. C., De Groot, A. E. & Pienta, K. J. Targeting the tumour stroma to improve cancer therapy. *Nat. Rev. Clin. Oncol.* **15**, 366–381 (2018).

109. Romualdi, C. *et al.* Defining the gene expression signature of rhabdomyosarcoma by meta-analysis. *BMC Genomics* **7**, 287 (2006).

110. De Pittà, C. *et al.* Gene expression profiling identifies potential relevant genes in alveolar rhabdomyosarcoma pathogenesis and discriminates PAX3-FKHR positive and negative tumors. *Int. J. Cancer* **118**, 2772–2781 (2006).

111. Stewart, E. *et al.* Identification of Therapeutic Targets in Rhabdomyosarcoma through Integrated Genomic, Epigenomic, and Proteomic Analyses. *Cancer Cell* **34**, 411-426.e19 (2018).

112. Brauchle, E. *et al.* Biomechanical and biomolecular characterization of extracellular matrix structures in human colon carcinomas. *Matrix Biol.* **68**–**69**, 180–193 (2018).

113. Ma, X. J., Dahiya, S., Richardson, E., Erlander, M. & Sgroi, D. C. Gene expression profiling of the tumor microenvironment during breast cancer progression. *Breast Cancer Res.* **11**, 1–18 (2009).

114. Reuter, J. A. *et al.* Modeling Inducible Human Tissue Neoplasia Identifies an Extracellular Matrix Interaction Network Involved in Cancer Progression. *Cancer Cell* **15**, 477–488 (2009).

115. Chen, H. J. *et al.* A recellularized human colon model identifies cancer driver genes. *Nat. Biotechnol.* 1–9 (2016). doi:10.1038/nbt.3586

116. Pence, K. A., Mishra, D. K., Thrall, M., Dave, B. & Kim, M. P. Breast cancer cells form primary tumors on ex vivo four-dimensional lung model. *J. Surg. Res.* **210**, 181–187 (2017).

117. Pavlou, M. *et al.* Osteomimetic matrix components alter cell migration and drug response in a 3D tumour-engineered osteosarcoma model. *Acta Biomater.* **96**, 247–257 (2019).

118. Hoshiba, T. & Tanaka, M. Decellularized matrices as in vitro models of extracellular matrix in tumor tissues at different malignant levels: Mechanism of 5-fluorouracil resistance in colorectal tumor cells. *Biochim. Biophys. Acta - Mol. Cell Res.* **1863**, 2749–2757 (2016).

119. Pinto, M. L. *et al.* Decellularized human colorectal cancer matrices polarize macrophages towards an anti-inflammatory phenotype promoting cancer cell invasion via CCL18. *Biomaterials* **124**, 211–224 (2017).

120. Crotti, S. *et al.* Extracellular Matrix and Colorectal Cancer: How Surrounding Microenvironment Affects Cancer Cell Behavior? *J. Cell. Physiol.* **232**, 967–975 (2017).

121. Roth, S. P. *et al.* Automated freeze-thaw cycles for decellularization of tendon tissue - a pilot study. *BMC Biotechnol.* **17**, 1–10 (2017).

122. Khetan, S. & Burdick, J. Cellular encapsulation in 3D hydrogels for tissue engineering. *J. Vis. Exp.* 3–7 (2009). doi:10.3791/1590

123. Zhu, J. Bioactive modification of poly(ethylene glycol) hydrogels for tissue engineering. *Biomaterials* **31**, 4639–4656 (2010).

124. Nam, S., Stowers, R., Lou, J., Xia, Y. & Chaudhuri, O. Varying PEG density to control stress relaxation in alginate-PEG hydrogels for 3D cell culture studies. *Biomaterials* **200**, 15–24 (2019).

125. Xu, W. *et al.* A double-network poly(Nε-acryloyl l-lysine)/hyaluronic acid hydrogel as a mimic of the breast tumor microenvironment. *Acta Biomater.* **33**, 131–141 (2016).

126. Liu, C., Lewin Mejia, D., Chiang, B., Luker, K. E. & Luker, G. D. Hybrid collagen alginate hydrogel as a platform for 3D tumor spheroid invasion. *Acta Biomater.* **75**, 213–225 (2018).

127. Campbell, J. J., Husmann, A., Hume, R. D., Watson, C. J. & Cameron, R. E. Development of three-dimensional collagen scaffolds with controlled architecture for cell migration studies using breast cancer cell lines. *Biomaterials* **114**, 34–43 (2017).

128. Liang, Y. *et al.* A cell-instructive hydrogel to regulate malignancy of 3D tumor spheroids with matrix rigidity. *Biomaterials* **32**, 9308–9315 (2011).

129. Shen, M. *et al.* Tinagl1 Suppresses Triple-Negative Breast Cancer Progression and Metastasis by Simultaneously Inhibiting Integrin/FAK and EGFR Signaling. *Cancer Cell* **35**, 64-80.e7 (2019).

130. Xiao, Y. *et al.* Integrin α5 down-regulation by miR-205 suppresses triple negative breast cancer stemness and metastasis by inhibiting the Src/Vav2/Rac1 pathway. *Cancer Lett.* **433**, 199–209 (2018).

131. Li, Y. *et al.* In vivo β-catenin attenuation by the integrin α5-targeting nano-delivery strategy suppresses triple negative breast cancer stemness and metastasis. *Biomaterials* **188**, 160–172

(2019).

132. Li, X. Q., Lu, J. T., Tan, C. C., Wang, Q. S. & Feng, Y. M. RUNX2 promotes breast cancer bone metastasis by increasing integrin α5-mediated colonization. *Cancer Lett.* **380**, 78–86 (2016).

133. Ryu, M. H., Park, H. M., Chung, J., Lee, C. H. & Park, H. R. Hypoxia-inducible factor-1α mediates oral squamous cell carcinoma invasion via upregulation of α5 integrin and fibronectin. *Biochem. Biophys. Res. Commun.* **393**, 11–15 (2010).

134. Haber, T. *et al.* Bone Metastasis in Renal Cell Carcinoma is Preprogrammed in the Primary Tumor and Caused by AKT and Integrin α5 Signaling. *J. Urol.* **194**, 539–546 (2015).

135. Lin, C.-H. *et al. FNDC3B* promotes cell migration and tumor metastasis in hepatocellular carcinoma. *Oncotarget* **7**, 2328–2338 (2016).

136. Barbazán, J. *et al.* Liver metastasis is facilitated by the adherence of circulating tumor cells to vascular fibronectin deposits. *Cancer Res.* **77**, 3431–3441 (2017).

137. Erdogan, B. *et al.* Cancer-associated fibroblasts promote directional cancer cell migration by aligning fibronectin. *J. Cell Biol.* **216**, 3799–3816 (2017).

138. Gopal, S. *et al.* Fibronectin-guided migration of carcinoma collectives. *Nat. Commun.* **8**, 14105 (2017).

139. Pankov, R. Fibronectin at a glance. *J. Cell Sci.* **115**, 3861–3863 (2002).

140. Borghi, N., Lowndes, M., Maruthamuthu, V., Gardel, M. L. & Nelson, W. J. Regulation of cell motile behavior by crosstalk between cadherin- and integrin-mediated adhesions. *Proc. Natl. Acad. Sci. U. S. A.* **107**, 13324–13329 (2010).

141. Feldkoren, B., Hutchinson, R., Rapaport, Y., Mahajan, A. & Margulis, V. Integrin signaling potentiates transforming growth factor-beta 1 (TGF-β1) dependent down-regulation of E-Cadherin expression – Important implications for epithelial to mesenchymal transition (EMT) in renal cell carcinoma. *Exp. Cell Res.* **355**, 57–66 (2017).

142. Azimian-Zavareh, V., Hossein, G., Ebrahimi, M. & Dehghani-Ghobadi, Z. Wnt11 alters integrin and cadherin expression by ovarian cancer spheroids and inhibits tumorigenesis and metastasis. *Exp. Cell Res.* **369**, 90–104 (2018).

143. Monier-Gavelle, F. & Duband, J.-L. Cross Talk between Adhesion Molecules: Control of N-cadherin Activity by Intracellular Signals Elicited by β1 and β3 Integrins in Migrating Neural Crest Cells. *J. Cell Biol.* **137**, 1663–1681 (1997).

144. Lathia, J. D. *et al.* Integrin Alpha 6 regulates glioblastoma stem cells. *Cell Stem Cell* **6**, 421–432 (2010).

145. White, D. E. *et al.* Targeted disruption of β1-integrin in a transgenic mouse model of human breast cancer reveals an essential role in mammary tumor induction. *Cancer Cell* **6**, 159–170 (2004).

146. Ota, D. *et al.* Tumor-α9β1 integrin-mediated signaling induces breast cancer growth and lymphatic metastasis via the recruitment of cancer-associated fibroblasts. *J. Mol. Med.* **92**, 1271–1281 (2014).

147. Chen, M. B., Lamar, J. M., Li, R., Hynes, R. O. & Kamm, R. D. Elucidation of the roles of tumor integrin β1 in the extravasation stage of the metastasis cascade. *Cancer Res.* **76**, 2513–2524 (2016).

148. Weber, M. R. *et al.* Activated tumor cell integrin αvβ3 cooperates with platelets to promote extravasation and metastasis from the blood stream. *Thromb. Res.* **140**, S27–S36 (2016).

149. Jahangiri, A. *et al.* Cross-activating c-Met/β1 integrin complex drives metastasis and invasive resistance in cancer. *Proc. Natl. Acad. Sci. U. S. A.* **114**, E8685–E8694 (2017).